

Growth and advanced characterization of solution-derived nanoscale $\text{La}_{0.7}\text{Sr}_{0.3}\text{MnO}_3$ heteroepitaxial systems

Jone Zabaleta Llorens

Departament de Materials Superconductors i Nanoestructuració a Gran Escala, ICMAB-CSIC
Supervisors: Prof. T. Puig Molina and Dr. N. Mestres Andreu
Tutor: Prof. A. Sánchez Moreno

Departament de Física
Programa de Ciència de Materials
Universitat Autònoma de Barcelona



Bellaterra, December 2011

Chapter 5

Advanced local characterization of LSMO nanoislands: PEEM and KPFM

The present chapter is devoted to the investigation of self-assembled ferromagnetic $\text{La}_{0.7}\text{Sr}_{0.3}\text{MnO}_3$ (LSMO) nanoislands by means of two cutting-edge nanoscale characterization techniques. Photoemission electron microscopy (PEEM) combines the high spatial resolution provided by electron imaging with the chemical, electronic and magnetic information attainable from X-ray-matter interaction. Meanwhile, Kelvin Probe Microscopy (KPFM) is based on the contact potential measurement between materials brought into electrical contact, as originally first achieved by Lord Kelvin back in 1898 [261]. Developed 30 years ago, KPFM is a powerful scanning probe technique, capable now of lateral atomic resolution in the mapping of local contact potential differences [262, 263]. These two distinct techniques have in common their rapid and continuous development, caused by the need to characterize increasingly small objects as well as new and complex materials systems. In this regard, both PEEM and KPFM characterization of solution-derived LSMO self-assembled nanoislands constitute a notable challenge, principally due to the insulating character of the substrates where the nanoislands lie. This makes KPFM measurement and its interpretation non-straightforward. On the other hand, feasible PEEM experiments require the a priori metal capping of the insulating samples, greatly reducing the intensity of the signal coming from the sub-200 nm size LSMO nanoisland. Under this experimental conditions, we will see, we are close to the resolution limit of the technique. To the best of our knowledge there are no attempts in the literature concerning the study by PEEM and KPFM of systems of these particular characteristics. This chapter presents the efforts in pushing the potential of these techniques towards the characterization of self-assembled nanoscale magnetic systems.

5.1 Photoemission Electron Microscopy measurements of self-assembled LSMO nanoislands

PEEM offers simultaneous imaging and spectroscopic characterization of material surfaces with high spatial resolution. Being able to probe the local chemical composition of the sample, it allows one to independently study the surface of the nanoislands in the case of self-assembled nanostructured templates, or even to chemically map individual nanoscale objects. In addition to elemental selectivity, PEEM also enables the study of the magnetic domain structure of surfaces of films and nanostructures. The recent technological interest and advances in the fabrication of novel and miniaturized magnetic devices, and the corresponding necessity for their fundamental understanding, makes PEEM a very valuable nanoscale magnetic characterization technique.

5.1.1 Basics on PEEM

In photoemission electron microscopy an intense light such as X-ray radiation, is directed into a sample triggering the excitation of core-level electrons into unoccupied states. The holes in the core levels are subsequently filled by electrons from higher energy states, either radiatively i.e. with the emission of fluorescence rays, or by Auger electrons that can suffer multiple scattering and yield a cascade of secondary electrons. The core-level photoemitted electrons (photoelectrons) and the cascade of elastically and inelastically scattered secondary electrons escaping the sample surface, are then accelerated under high voltages (typically 20 kV). Then, these electrons are carried along an electron-optical system which generates, transfers, and magnifies the image, finally formed onto a phosphor screen. The electron image is converted there into a visible image by means of a CCD camera (see Fig. 5.1 below). The energy spectra of the PEEM-transmitted electrons is considerably broad, ranging from directly emitted photoelectrons to low-energy secondary electrons. This is one of the main factors that limit the resolution (known as chromatic aberration). Other lens aberrations include astigmatism or spherical aberration, in which rays at different angles are focused at different distance from the focal plane. Increasing the acceleration voltage or decreasing the contrast apertures are some of the strategies used to enhance the lateral resolution, presently at around ~ 30 nm, and further improving [264].

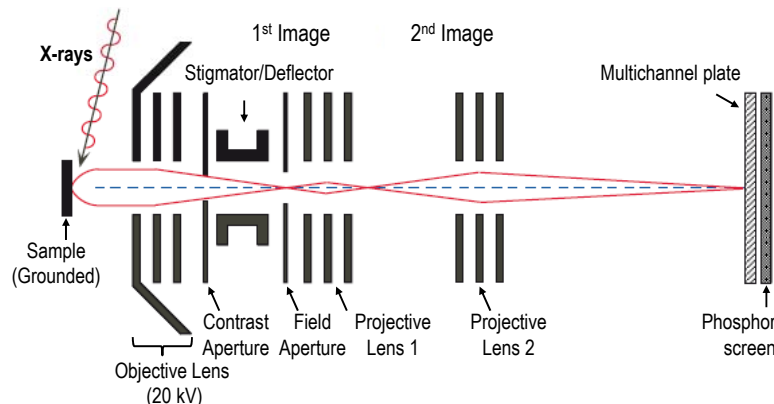


Fig. 5.1: Electron-optics layout within the PEEM chamber. Adapted from [265].

X-ray PEEM (X-PEEM) experiments are performed in synchrotron-radiation facilities, which provide intense, naturally polarized light, with wavelengths ranging from micrometers (infrared) up to Angstroms (hard X-rays). X-PEEM is typically operated in the soft X-ray regime, i.e. with radiation energies in the 100-2000 eV range, where many of the most important magnetic transition metals like Fe, Co, Mn, and Ni have their L -absorption edges (the $2p \rightarrow 3d$ transition). The K -edge of light elements (O, C, Si...) and the M -edge of rare-earth metals also fall in this energy range. Fig. 5.2 shows a schematic drawing of the fundamental instrumental parts constituting a X-PEEM experiment. X-rays, generated by the deflection of relativistic electrons within the synchrotron storage ring, are directed into the specific PEEM beamline, after choosing their polarization (either linear, circular or elliptical). The monochromator in the line selects the energy of the beam, in minimum steps of 0.1 eV, and a mirror system brings the light onto the sample surface. After the X-ray interacts with matter, the escaping electrons enter the PEEM electron-optical system depicted in Fig. 5.1.

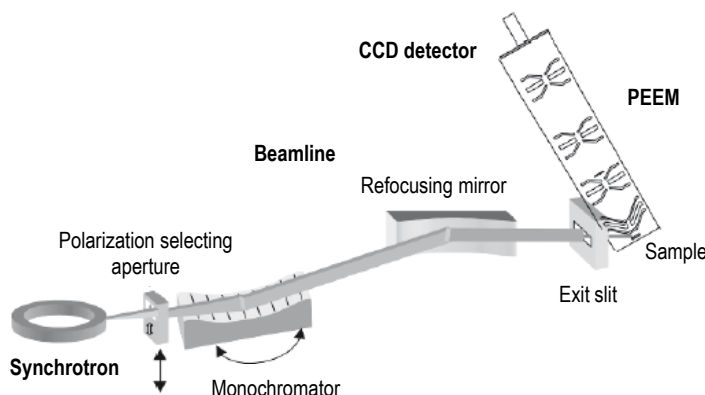


Fig. 5.2: Schematic drawing of the PEEM integration in a synchrotron facility. Reproduced from [266].

Chemical and Magnetic contrast in X-PEEM

The fundamental characteristic of X-PEEM is that it provides spatially-resolved chemical and magnetic contrast in the nm range. This is done by simultaneously recording the emitted electrons, at a certain energy, for every point of the imaged sample. By changing the energy (in steps as small as 0.1-0.5 eV), the changes in e^- emission are monitored in the form of a darker or brighter contrast. The usual working mode consists in collecting all of the electrons (directly photoemitted and secondary) that escape from the sample due to the de-excitation process initiated by the X-ray absorption. This mode is known as Total Electron Yield (TEY) mode. When the energy of the arriving photons meets that of a certain electronic transition in a particular element, the absorption is greatly enhanced and this, in turn, augments the cascade of electrons emitted from that particular spot of the sample (the spot is seen with bright contrast). It can be demonstrated that if the penetration depth of the X-rays is larger than the escaping depth of the electrons, Δ , the absorption is directly proportional to the electron yield signal [265, 267, 268]. The escaping depth is determined by the average depth from which low energy secondary electrons (the great majority) leave the sample. This distance is measured experimentally, taking values from 1.5 nm to 2.5 nm

in ferromagnetic metals (for instance, $\Delta \sim 21$ Å and $17 (\pm 2)$ Å have been measured for Fe [268, 269]). Therefore, X-PEEM is essentially a surface-sensitive technique. By recording the intensity maps (which constitute the PEEM images) at several energies, and integrating the stack of images within the area of interest, we obtain the X-ray Absorption Spectrum (XAS) of that specific sample region. By tuning the energy range and the energy resolution adequately, not only the general aspects of the XAS spectra but also their fine structure can be studied. The latter, known as X-ray Absorption Near Edge Structure (XANES) allow one to discern different valence states of the studied element, as well as to learn about the chemical environment of the analyzed atoms, since their characteristic spectra depend on it.

The other major characteristic of X-PEEM is the possibility of imaging the magnetic domains of ferromagnetic surfaces using X-ray magnetic circular dichroism (XMCD). XMCD is based on the distinct absorption of left- and right-handed circular polarized light by the electrons of a ferromagnet. The interaction with the illuminating X-rays causes the spin of photoelectrons to change polarization. This change depends on the helicity of the light and on the spin state of the excited core-electron and may be expressed in the following way [265]:

$$\vec{P}(\vec{\sigma}^+) = -\vec{P}(\vec{\sigma}^-) \quad (5.1)$$

$$\vec{P}(2p_{3/2}) = -k \cdot \vec{P}(2p_{1/2}) \quad (5.2)$$

Here \vec{P} stands for polarization and σ^+ (σ^-) for the left-handed (right-handed) circularly-polarized light. Eq. 5.1 indicates the change in polarization direction when the helicity of the incident light is opposite. As regards Eq. 5.2, it expresses the dependency of polarization with the core-electron spin. The splitting of the $2p$ level due to spin-orbit interaction gives rise to the L_3 and L_2 -edges in transition metals, which correspond to $2p_{3/2} \rightarrow 3d$ and $2p_{1/2} \rightarrow 3d$ transitions, respectively. According to Eq. 5.2, the polarization changes sign and magnitude from one $2p$ level to the other. Besides, in the case of a ferromagnetic material, the probability for an electron to be excited into an unoccupied state depends precisely on its polarization, i.e. on whether it is a minority spin with a large available unoccupied Density of States (DOS) above the Fermi level (E_F), or, conversely, a majority spin with a low DOS above E_F . As the polarization depends on the helicity of the light (Eq. 5.1) and, from what we have just said, the transition probability of electrons in a ferromagnet depends on the polarization of the photoelectrons, it follows that the intensity I of the absorption edge will be different for opposite light helicities:

$$I(\vec{\sigma}^+) \neq I(\vec{\sigma}^-) \quad (5.3)$$

Fig. 5.3 shows the XAS for the Mn L_3 and L_2 edges in a $\text{La}_{0.7}\text{Sr}_{0.3}\text{MnO}_3$ thin film at 100 K, measured with the light helicity either parallel or antiparallel to the magnetization. The XMCD spectrum below, also known as the *dichroic spectrum*, is then calculated from the difference between $I(\vec{\sigma}^+)$ and $I(\vec{\sigma}^-)$ [270]. The integration of intensities and the application of the so-called *sum rules* can be further used to calculate the magnetic orbital and spin moments of the specific elements measured [271, 272].

Regarding magnetic domain imaging, the usual procedure is to collect PEEM images at fixed photon energies where the magnetic contrast is maximum, i.e. at the L_3 or L_2 absorption edges for the case of ferromagnetic (FM) transition metals. Contrary to FM materials, for non-magnetic materials there is no absorption change with circular polarization,

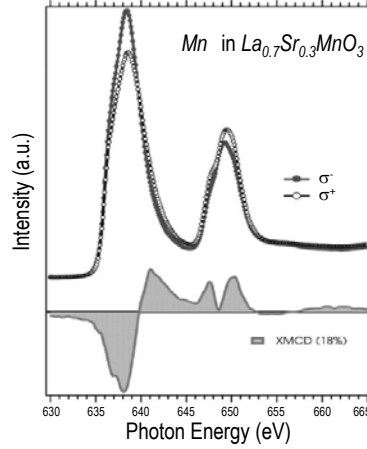


Fig. 5.3: XAS for Mn $L_{3,2}$ -edges in a $\text{La}_{0.7}\text{Sr}_{0.3}\text{MnO}_3$ thin film for light helicity aligned either parallel or antiparallel to the magnetization vector. The difference between the two spectra yields the XMCD signal below. The measurement was done at 100 K. Adapted from [270].

i.e. $I(\vec{\sigma}^+) = I(\vec{\sigma}^-)$. Consequently, the common way of enhancing the magnetic contrast in PEEM images is by getting rid of the non-magnetic contrast by subtracting two images taken at the same energy but with opposite helicities:

$$A_{\sigma}(x, y) = \frac{I_{\sigma^+}(x, y) - I_{\sigma^-}(x, y)}{I_{\sigma^+}(x, y) + I_{\sigma^-}(x, y)} \quad (5.4)$$

where $A_{\sigma}(x, y)$ is known as the *asymmetry image* [265]. Equivalently to Eq. 5.4, the XMCD image can be obtained by subtracting two images taken with the same helicity but opposite magnetization directions. A clear example of such contrast enhancement is illustrated on the left panel of Fig. 5.4 (a) and (b), in which the nickel rectangular structures (12 μm equivalent diameter) of Fig. 5.4 (b) (the asymmetry image) display purely FM contrast, after eliminating non-magnetic contributions (chemical, topographical...etc.) exhibited in Fig. 5.4 (a) [265]. The black and white contrast and the gray shades in between account for the relative orientation of the magnetization vector with respect to the light helicity. Indeed, the intensity of the contrast may be expressed as $I \sim \vec{M} \cdot \vec{\sigma} \sim I_0 \cos(\alpha)$ with \vec{M} the magnetization vector of the sample and α the angle between the helicity vector and \vec{M} . Fig. 5.4 (c) on the right shows the magnetic domain pattern of a (001)-Fe (001) surface obtained at the iron $L_{2,3}$ edge [265]. The arrows display the in-plane magnetization direction within each domain. In addition to FM samples, X-PEEM can also probe technologically important antiferromagnetic materials such as Ni and Co oxides or complex oxides like LaFeO_3 [273], taking here advantage of X-ray Linear Magnetic Dichroism.

5.1.2 Experimental procedure: on the metal capping of insulating substrates

We conducted the PEEM measurements at the UE49-PGM-1-SPEEM Beamline at the synchrotron light source BESSY II (Berlin), in the context of the scientific collaboration with Dr. S. Valencia (BESSY) and with the technical support and supervision of Dr. J. Herrero-Albillos and the Beamline scientist Dr. F. Kronast. A beam time of 3 weeks in total, separated in three periods, was devoted to our samples. We measured self-assembled ferro-

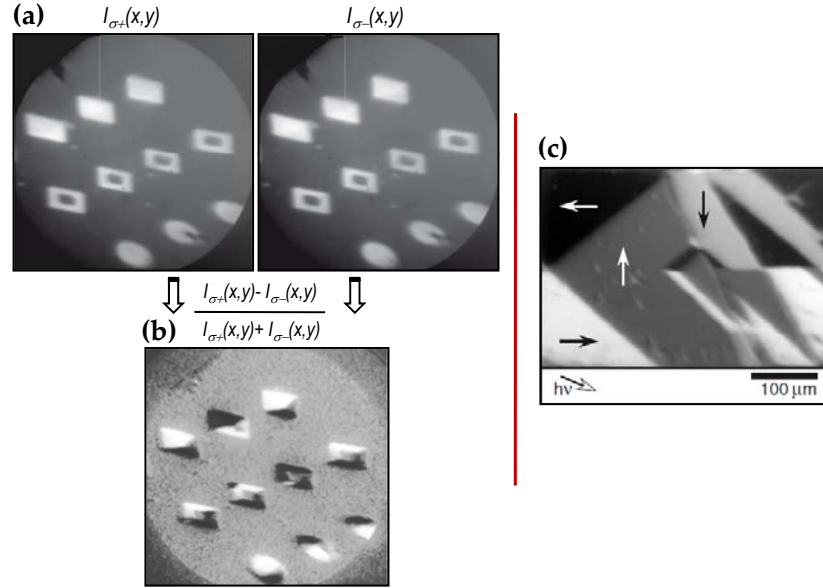


Fig. 5.4: (a)&(b) Example of the ferromagnetic contrast PEEM image obtained from the subtraction of two consecutive images taken at the same photon energy but with opposite helicities. The subsequent normalization further enhances the FM contrast. The sample consists of rectangular Ni structures, with $\sim 12 \mu\text{m}$ equivalent diameter [265]. (c) (001)-Fe thin film PEEM magnetic contrast image. The various shades of gray are caused by the relative angle between magnetization and the incident light propagation vector [265].

magnetic LSMO nanoislands on YSZ substrates, grown from 0.03 M precursor solutions, and heat-treated at 900°C for 1 h to 3 h. These nanoislands are small, near the PEEM resolution, with thickness $t \sim 10\text{--}60 \text{ nm}$ and lateral sizes $D \sim 40\text{--}200 \text{ nm}$, and a variety of aspect ratios. Among the two possible nanoisland morphologies, we selected the *regular-square* nanoislands, described in Chapter 3, mainly because they are larger and appear separated at larger distances than the *rotated-square* nanoislands. Recall that samples exhibiting the (001)_{LSMO}-oriented *regular-square* nanoislands also display a minority population of (111)_{LSMO}-oriented triangle-base nanoislands.

With PEEM we can explore both the absorption edges of individual nanoislands and averaged signals of nanoisland collections. As shown in previous chapters, these ferromagnetic islands have a $T_C \sim 350 \text{ K}$ and display various possible nanoscale magnetic configurations, revealed by MFM. As compared to MFM, PEEM offers complementary information regarding the ferromagnetic structure of nanoislands: it is sensitive to the in-plane magnetization direction rather than to the out-of-plane stray field sensed by MFM (recall the intensity dependence $I \sim \vec{M} \cdot \vec{\sigma}$). Furthermore, in PEEM we avoid the influence of the tip on the magnetic contrast of the sample, and we may thus observe the unperturbed magnetic structure. Nevertheless, the small island size makes it difficult to resolve their magnetic domains.

Influence of the capping on photoemission experiments

Before going through the chemical and magnetic investigation of the nanoislands our first objective is to overcome the most important experimental factor limiting the measure-

ments: the insulating nature of the single crystal YSZ substrates. To bring the electrons emitted from the sample into the microscope, we mentioned earlier that a high voltage (20 kV) is applied between the sample surface (the cathode) and the first part of the objective lens, called the extractor electrode (the anode). Consequently, the sample surface, in contact with the grounded sample-holder, must be conducting. To circumvent this issue we explored the coating of our LSMO/YSZ nanostructured samples using different non-ferromagnetic metals: platinum, copper, and aluminum. In the following we explain the details of this strategy and some of the difficulties it introduces.

First of all, X-rays must get across the metal capping layer into the LSMO nanoislands without a significant intensity loss. Aluminum cappings are very common in electron emission microscopies precisely because they are highly transparent to X-rays, compared to other denser metals like copper or platinum. The latter, in turn, offers a greater conductivity. Fig. 5.5 (a) shows the attenuation length of X-rays*, impinging at a 16° angle with respect to the substrate horizontal, for Al, Cu and Pt, as a function of different photon energies in the 500 eV to 700 eV range [274]. We have chosen to plot this energy range because it comprises the manganese absorption edge. Additionally, we have selected the 16° X-ray incidence angle because it is the angle ($\pm 3^\circ$) used in the experimental set-up of our PEEM measurements[†]. The larger this angle, the farther the X-rays will penetrate [see Fig.5.5 (b), plotted for the case of Pt]. From Fig. 5.5 (a) it is evident that X-rays penetrate long distances in Al, while for photons of 700 eV, Pt coatings larger than 15 nm produce a decrease in X-ray intensity above 37%.

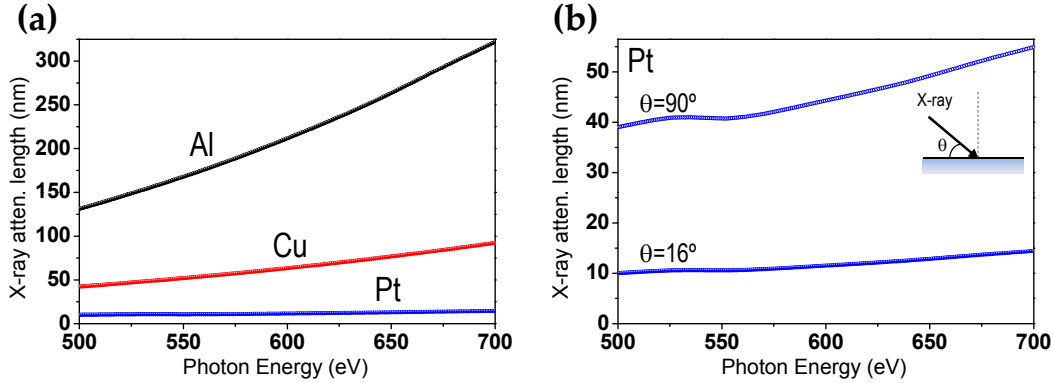


Fig. 5.5: X-ray attenuation lengths as a function of photon energy, for energies in the 500-700 eV range. (a) Comparison for Al, Cu, and Pt coatings. The X-ray incidence angle was taken 16° with respect to the surface horizontal. (b) X-ray attenuation length notably increases with higher incidence angles. The plot shows the case for Pt at $\theta = 16^\circ$ and $\theta = 90^\circ$.

In order not to decrease the photon intensity substantially, therefore, we should keep the Pt coating thickness below 15 nm, below 50 nm in the case of Cu, and around a few hundreds of nm for Al. We knew from previous PEEM experiments in thin LSMO films [140] that a resistance of the order of 10 kOhms, measured with a two-probe tester, was sufficiently low to make the PEEM measurement feasible. For electron-beam sputtered

*X-ray attenuation length is defined as the depth into the material, measured along the surface normal, at which the X-ray intensity has decayed $1/e$ ($\sim 37\%$) with respect to its value at the material surface.

[†]Selecting an X-ray incidence angle of 16° is common procedure in PEEM experiments. It gives a compromise between having a large signal for in-plane magnetization and being able to detect out-of-plane magnetization components.

Pt layers, for instance, we achieved such values with $\sim 2\text{-}5$ nm thick coatings. Hence, regarding photon penetration, the metallic coating does not hamper the measurement. The critical point, as we shall see next, relies in the great loss of collected electrons caused by the capping.

We already mentioned that PEEM is mainly a surface-sensitive technique, since only electrons ejected within a few nm from the sample surface will be able to leave the sample and reach the detector. Such electron *mean escape depth* (Δ), in turn, depends on the inelastic mean free path (λ_i) of electrons (which is a material-dependent quantity), and of the electron emission angle (α). This dependence is expressed as $\Delta = \lambda_i \cos \alpha$. The intensity due to the surface-emitted electrons, in turn, decays with the increasing capping thickness t according to the exponential law [275]

$$I_S = I_S^0 e^{-\frac{t}{\lambda_i \cos \alpha}} \quad (5.5)$$

In reality, electrons also undergo elastic-scattering events that change their trajectories. To take into account such effects one needs to replace λ_i with L , the *effective attenuation length*, which varies with sample thickness and emission angle [275]. In Fig. 5.6 we plot the decay of the electron intensity (in percents) as a function of the metal capping thickness for the three metals used (Al, Cu, Pt), and for two different electron energies i.e., 200 eV [Fig. 5.6 (a)] and 1000 eV [Fig. 5.6 (b)][‡]. These energy values are far apart from each other and therefore set the boundaries for what the decay is like at intermediate energies. The detector, as in our experiment, is considered parallel to the substrate surface. Note also that two different emission angles, $\alpha=0^\circ$ and 55° , were considered. Recall that the electron mean escape depth varies with the emission angle, and that the majority of our nanoislands are square-base pyramids faceted in the (111) planes, hence at 55° from the substrate horizontal (see the schematic diagram at the top right corner of Fig. 5.6). The intensity decay is stronger for electrons leaving the sample at inclined angles than for normal emission ($\alpha=0^\circ$). Aluminum is the metal showing the slowest decay, and Pt the most rapid, close to Cu in the case of slow electrons. Anyhow, the thickness values necessary to prevent an excessive loss of electron intensity are very low: for a Pt capping of $t=2$ nm the intensity falls to 10% in the case of 1000 eV electrons, and a capping as thin as $t\sim 1$ nm is required to achieve the same signal in the case of slower electrons. The best situation is found for Al capping, which allows the same intensity (10%) at twice the thicknesses (~ 5 nm for 1000 eV). In addition to the loss due to the capping we should keep in mind that the electron intensity will first decay within the LSMO sample before reaching the metal overlayer. Fortunately, this decay is not as strong as in Pt; for the fastest electrons, an intensity loss of 90% corresponds to values of 4 and 6 nm, for $\alpha=55^\circ$ and 0° , respectively (not shown).

Capping selection experiments

Copper and aluminum capping were performed at the BESSY Synchrotron facility, using the evaporator system and a separate chamber dedicated to sample sputtering and metal deposition available in the PEEM. The main advantage is the possibility of starting with very thin deposits, enter the sample in the PEEM, check whether it conducts, and, if not, realize further depositions and checks. The disadvantage is that, when the sample does

[‡]We have calculated these plots through simulations available from the NIST Electron Effective Attenuation Length Database [276]. These data are based on Eq. 5.5, revised as to take into account L values instead of λ_i . They calculate the electron mean escape depth Δ values for a given α , L and λ_i .

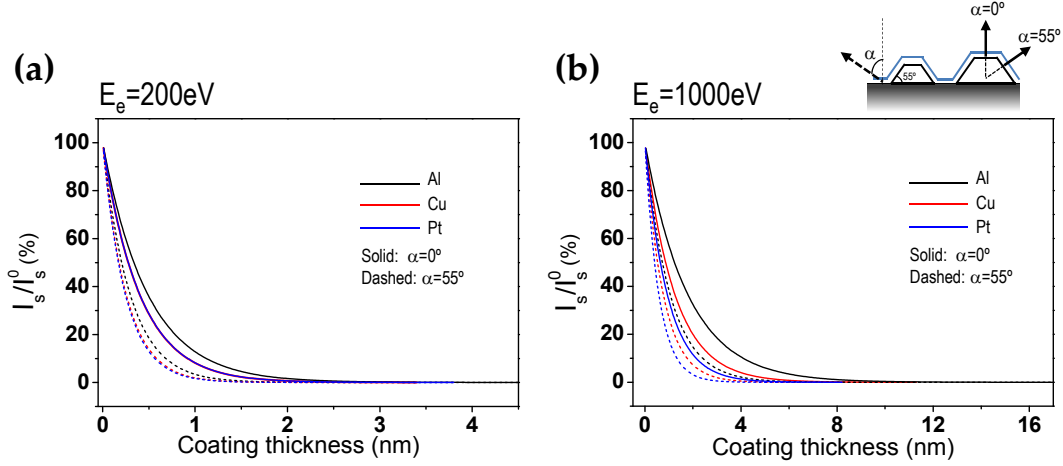


Fig. 5.6: Relative decay of the emitted electron intensity as a function of the coating thickness for 200 eV (a) and 1000 eV (b) electron energies. Al, Cu and Pt capping and two possible emission angles $\alpha=0^\circ$ (solid lines) and $\alpha=55^\circ$ (dashed lines) are considered. The sketched diagram at the top right corner illustrates the geometry of such emission processes.

not conduct, we cannot know whether the thickness is insufficient, or whether the problem stems from the lack of electrical contact between the sample-holder cap and the sample surface. To verify this, we need to remove the sample from the chamber (thus first undo the vacuum), check the contact, reposition the cap in the case cap and sample do not make electrical contact, and re-insert the sample in the PEEM. These checks require successive venting and pumping down of the load-lock chamber, and ensuring the ultra-high vacuum (UHV) chamber does not lose its vacuum. On the other hand, Pt-coated samples were electron-beam evaporated *ex-situ* (at the Scientific Services of the UAB, Barcelona). Thus, the sample was known to make electrical contact before introducing it into the PEEM. In turn, we could not a priori ascertain whether the capping was too thick to be able to detect any signal until the PEEM measurement was performed.

Among the series of experiments we made to optimize the capping experiments for enhanced PEEM signal, *ex situ* evaporated *platinum* yielded the best results. The next sections will in fact be based on Pt-coated samples. *Copper* capping, starting from $t=1$ nm up to 5 nm layers did not work: the initial thin layers (1-1.5 nm) produced sparks in the PEEM, indicative of sample charging, i.e., of insufficiently conducting capping. Moreover, these sparks did not disappear with increasing coating thickness. This suggests that such sparks removed part of the Cu layer producing a rough surface with possible bare substrate spots that did not improve in quality upon further Cu deposition. Regarding *aluminum*, this was a priori the best option, according to the X-ray attenuation length and the electron intensity decay studies described above (Figs. 5.5 and 5.6). However, the strong tendency of Al towards oxidation (its oxidation potential is the highest of all elemental metals except K, Ca, Na and Mg) can trigger depletion of oxygen from the LSMO upper layers, with the consequent loss of ferromagnetism [277].

To prevent the Al-triggered LSMO de-oxygenation, we deposited 1.5 nm of Cu prior to the 5 nm Al capping. Fig. 5.7 (a) shows a PEEM 5 μm field of view (meaning 5 μm diameter) image of a LSMO/YSZ nanostructured sample, taken at $E=639.2$ eV. The image is normalized first by subtracting the detector background image, and second, with the

subtraction of an image taken at the pre-edge of the Mn L -edge. The latter is often used to enhance the signal from a particular element [266] and will be invariably applied in all of the PEEM images shown hereafter. A bright contrast emerges from the island structures as opposed to the dark YSZ substrate, indicating the presence of Mn within the islands. Fig. 5.7 (b) displays the TEY XAS for the Mn L edge, obtained by integrating the intensities within a certain area, selected from the image of Fig. 5.7 (a), for a stack of images running from the Mn L pre-edge (635 eV) up to 660 eV in the present case. The XAS in the top row of Fig. 5.7 (b), very noisy, corresponds to a single island, with area around $(166 \times 120) \text{ nm}^2$, comprising ~ 126 pixels. If we sum the contribution of a large number of spectra, which is done by selecting simultaneously a large number of islands, the signal to noise ratio of the resulting *averaged* spectrum increases substantially, revealing more detailed absorption features. Note that the highest peak corresponds to $E=639.2 \text{ eV}$, precisely the energy at which the island contrast is brightest.

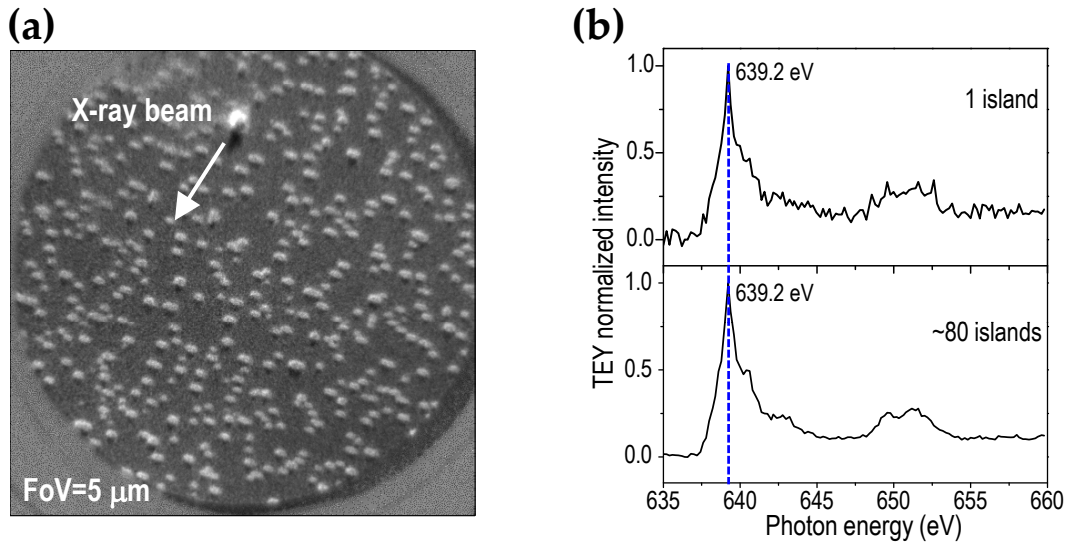


Fig. 5.7: (a) PEEM image at $E=639.2 \text{ eV}$ of a LSMO on YSZ nanostructured template coated with 1.5 nm Cu (in contact with the sample surface) and 5 nm Al . Field of view $\text{FoV}=5 \mu\text{m}$. (b) XAS of the Mn $L_{2,3}$ -edges obtained for a single nanoisland (top panel) and for a large number of them (lower panel). The integration of many nanoislands largely increases the signal to noise ratio.

The difference between the XAS of Fig. 5.7 and that corresponding to stoichiometric $\text{La}_{0.7}\text{Sr}_{0.3}\text{MnO}_3$ (LSMO), in Fig. 5.3, is remarkable. Although we can recognize some features from the ferromagnetic LSMO spectrum in Fig. 5.7 (b), such as the presence of the double-step background, the general shape of the two spectra differ notably. Moreover, in measurements on LSMO ferromagnetic thin films done the same day under identical experimental conditions, the Mn L_3 edge was found at $\sim 641 \text{ eV}$, well above the energy shown by the highest peak in Fig. 5.7 (b) (639.2 eV)[§]. Our results hence indicate a departure from the $\text{Mn}^{3+}/\text{Mn}^{4+}$ valence composition expected for LSMO. A peak in the XAS at lower energies than the main L_3 peak has been identified in the literature as the fingerprint of Mn^{2+} in the case of de-oxygenated LSMO and LCMO surfaces [278–281]. In these works, the presence of Mn^{2+} appears superimposed to the original $\text{Mn}^{3+}/\text{Mn}^{4+}$ composition (i.e. coexisting with the ferromagnetic manganite). Also, the Mn^{2+} is predominantly related to

[§]The energy resolution was kept at $0.1\text{--}0.3 \text{ eV}$ for the majority of the spectra.

the film surface and grain boundaries, i.e. the places more likely to suffer the effect of atmosphere exposure, defects...etc. The Mn^{2+} fingerprint of our spectra is even more evident, suggesting that the de-oxidation of LSMO in our case is more pronounced; this, in turn, would reduce the fraction of Mn^{3+}/Mn^{4+} consequently destroying the ferromagnetism of the compound. Effectively, no XMCD signal could be measured for this sample. In Fig. 5.8 we compare our data (bottom graph) with the XAS for the Mn L edge in two cases having purely Mn^{2+} . Our results agree much better with this latter spectra than with the spectrum for LSMO in Fig. 5.3. We can therefore conclude that the copper coating does not prevent the LSMO de-oxidation caused by the Al capping.

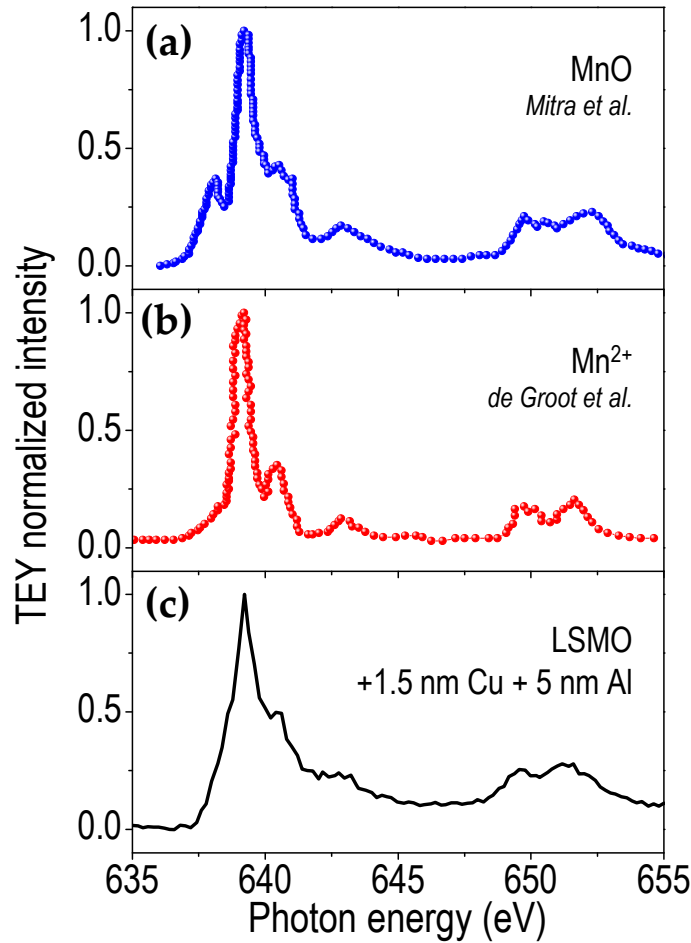


Fig. 5.8: Mn L -edge XAS for (a) MnO compound [282], (b) Mn^{2+} in a cubic crystal field, with field splitting of 0.6 eV [283], (c) LSMO on YSZ nanostructured sample with 1.5 nm Cu + 5 nm Al capping.

Based on the above study we discarded the copper and aluminum cappings for further measurements. Therefore, the following analyses are focused on platinum-coated samples, with estimated thickness between 2 and 4 nm.

5.1.3 Chemical analysis: probing the nanoscale chemical features

Surface and bulk composition of LSMO nanoislands

The images in Fig. 5.9 were taken at the Mn L_3 -edge ($E=641.3$ eV). The $5\text{ }\mu\text{m}$ field of view PEEM image shown in Fig. 5.9 (a) reveals a dispersion of black spots on a gray background. The digital zoom (below) shows that these dark dots have elongated shape in the direction of the illuminating X-rays. Moreover, one can also notice that the black dot is accompanied by a slightly brighter contrast. This image is the result of merging 10 images taken at the same energy, and the only normalization done is against the detector. By further subtracting the background image acquired at the Mn L pre-edge, we significantly enhance the contrast, as evidenced by Fig. 5.9 (b). The dark spots are still there, but now the bright contrast can also be clearly perceived.

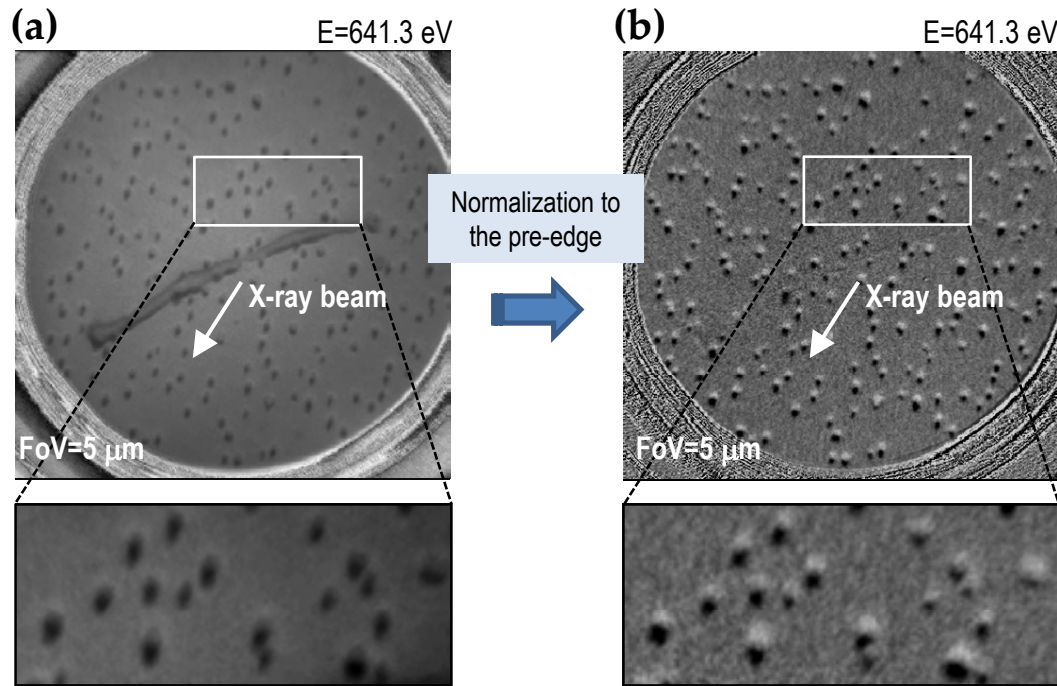


Fig. 5.9: PEEM images ($5\text{ }\mu\text{m}$ field of view) of a Pt-coated LSMO nanostructured sample taken at the Mn L -edge. They are the result of merging 10 images. (a) After subtracting the detector image. (b) After further subtracting the Mn L -pre-edge image.

By illuminating our sample with X-rays at the Mn L -edge energy, we expect the Mn-rich regions to give a bright contrast, indicative of the $2p \rightarrow 3d$ transition and of the subsequent secondary electron emission (see section 5.1.1). In Fig. 5.9 we do, in fact, observe bright spots, but these appear linked to a black *shadow*, which is even easier to see [Fig. 5.9 (a)]. The spatial distribution of the structures and their lateral sizes are in agreement with what one expects from the topology of the self-assembled LSMO nanoislands, which we checked with AFM beforehand. The presence of the island *shadow*, in turn, is the consequence of the X-rays 16° grazing angle with respect to the sample surface. PEEM investigations of nanoislands, although still very scarce and mostly involving semiconductor nanocrystals, have already identified the shadow effect, which is caused by low X-ray

incident angles on *nm* size objects [284–286]. Beyond considering the impact of such geometrical effects on the intensity of XAS spectra [284], however, no further importance was ascribed to the presence of the island shadow. Fig. 5.10 (a) shows the same PEEM data as Fig. 5.9 (b), using a different color scale to better distinguish the *island* and *island-shadow* features. Blue corresponds to the highest TEY values (island) and red to the lowest (shadow), with white in between. In Fig. 5.10 (c) we plot the laterally resolved spectra obtained from integrating the selected areas in (b) for a number of images running from the Mn *L* pre-edge up to the post-edge. While the top graph in Fig. 5.10 (c) shows the expected absorption spectrum, the bottom graph displays the reversed Mn *L*_{3,2} edges characteristic of a transmission experiment. The origin of these two information sources, simultaneously obtained in our case, relies on the experiment geometry, as we will discuss next.

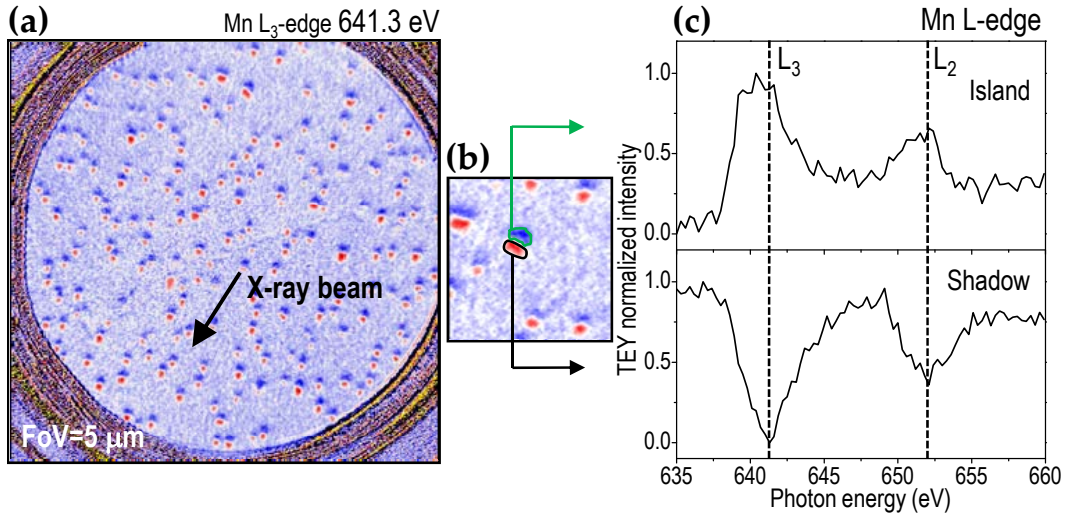


Fig. 5.10: (a) PEEM image from Fig. 5.9 (b), displayed now with a blue-red color scale. Blue corresponds to bright contrast (enhanced TEY signal) and vice versa. (b) Island and island-shadow regions for a single nanostructure. (c) Laterally-resolved spectra corresponding to the island and island-shadow regions marked in (b).

We plot the schematic diagram of our experimental configuration in Fig. 5.11 (a). The light impinges on the island at a 16° angle, goes through the Pt coating (not drawn to scale) and part of it passes through the whole nanoisland reaching the opposite side. The LSMO nanostructure in the sketch exhibits the 55° inclined (111) facets, as in the real case, and its proportion (lateral size $D=3.5$ times the island thickness) is also within the measured nanoisland aspect ratio statistics. When the energy of the X-rays matches the Mn *L*-edge, absorption processes occur throughout the entire island, triggering the cascade of electrons that produce the TEY signal. Because of the small mean escape depth of electrons, especially in Pt, many of them won't be able to leave the island; only very few, the most superficial of the LSMO island, will escape and be collected to form the image. Meanwhile, the X-rays will have traversed the entire island since the attenuation length of X-rays is much larger than the electron escape depth. In the process, however, the Mn atoms located deep within the bulk of the island will undergo the same absorption processes we just mentioned. The result of such a large number of photons being absorbed is that the light that reaches the other end of the structure is less intense. And it is more or less intense depending on the degree of absorption suffered in the bulk, i.e. depending on the energy value.

This is precisely what happens in a transmission experiment. Therefore, due to the grazing incidence, we have the negative image of what happens in the island bulk. The secondary electrons that do not come from the Mn-rich places form the grayish background, with much smaller intensities. At the shadow places, however, the electrons that reach the detector are less than those coming from the background, simply because the X-ray intensity reaching that places is less.

In brief, thanks to the grazing angle of light, which permits some rays to reach the substrate surface at the opposite end of nanoislands, we have access to the chemical information of the *bulk* of the nanostructure. The Pt capping, although greatly reducing the incoming signal, further restricts the information depth of the TEY signal to the very *surface* of the island. The latter, instead of a limitation, appears in the present case as an advantage, because it gives us access to the information of the island surface, which is complementary to the bulk characterization obtained by the transmission results. In Fig. 5.11 (b) we plot the result of integrating both island and island-shadow areas, as we did in Fig. 5.10 (c), but now for a total of ~ 85 nanostructures in order to enhance the signal to noise ratio [we have also reversed the transmission spectrum (bottom panel) to better compare its features with the spectrum from the nanoisland surface (top panel)]. Let us once more underline that we identify the *island* (bright and blue contrasts in Figs. 5.9 and 5.10, respectively) with the *surface* information, and the *shadow* (dark and red contrasts in Figs. 5.9 and 5.10, respectively) with the *bulk* information. The *bulk* spectrum in Fig. 5.11 (b) displays the shape of the expected Mn $L_{2,3}$ edges XAS for Mn^{3+}/Mn^{4+} composition according to the 0.7:0.3 La-Sr ratio in $La_{0.7}Sr_{0.3}MnO_3$. It is remarkable its good agreement with the XAS for $La_{0.7}Sr_{0.3}MnO_3$ reported by de Jong et al. [278]. In contrast, the *surface* spectrum displays larger differences. In addition to being noisier (the intensity counts were $\sim 43\%$ of the intensity of the bulk spectrum) it also shows a new peak at around 639.5 eV, which does not appear in the bulk spectrum.

In the previous section we discussed the peak at low energy of the Mn L -edge spectrum (~ 639.2 eV) in terms of Mn^{2+} formation due to the aluminum capping. At variance with that sample, where the Mn^{2+} signal was dominant, the results here show that the low energy (~ 639.5 eV) peak is a secondary feature superimposed to the characteristic bulk LSMO spectrum. Meanwhile, the nanoisland bulk shows no traces of such low-energy peak, as confirmed by the transmission spectra. Hence it appears that, in agreement with previous experiments [279, 280], if that peak is related to the Mn^{2+} ion, its presence is limited to the surface, where it coexists with the Mn^{3+}/Mn^{4+} mixed valence composition. Moreover, Mn^{2+} formation, which occurs at expenses of destroying the Mn^{3+}/Mn^{4+} stoichiometric ratio in $La_{0.7}Sr_{0.3}MnO_3$, is expected to decrease the ferromagnetic signal of the compound. Therefore, its presence can be related to the ferromagnetic dead layer concept already introduced in Chapters 3 and 4. In other words, the loss of ferromagnetic signal observed in manganite nanoislands on YSZ (with respect to bulk LSMO), which we argued in terms of the generally accepted concept of a surface/interface dead magnetic layer, could be rooted in the presence of Mn^{2+} . It should be noted, nevertheless, that the subtraction of the bulk spectrum from that associated to the surface did not yield as clear a Mn^{2+} fingerprint as the ones reported in the literature [279, 280] (not shown). It turns out that the signal from the surface is too weak and noisy with respect to the bulk signal to be able to discern a clean signal.

The origin of Mn^{2+} ion was claimed to be related to oxygen vacancies found at the surface [280]. In turn, the surface de-oxygenation was explained as a consequence of

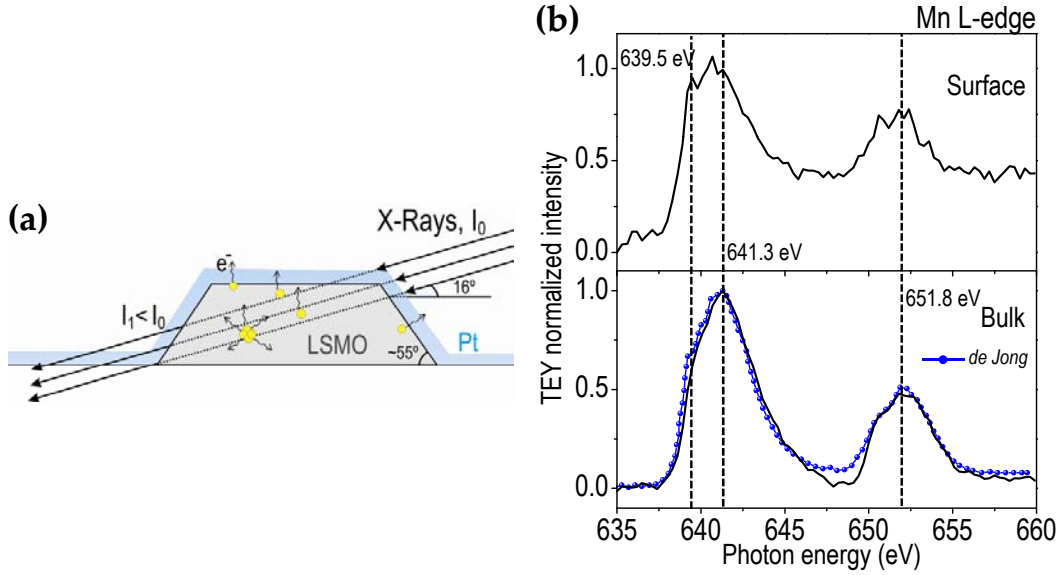


Fig. 5.11: (a) Schematic diagram of the X-rays impinging at 16° on a LSMO nanoisland. The yellow circles illustrate absorption events from which electron cascades are generated. The X-rays that manage to cross the entire island are less than those at the beginning. (b) The particular experiment geometry enables discerning island surface and island bulk XAS for the Mn, averaged among ~ 85 islands in these particular graphs. The reported XAS corresponding to the Mn^{3+}/Mn^{4+} ratio in $La_{0.7}Sr_{0.3}MnO_3$ [278] has been plotted for comparison.

vacuum annealing [278, 280], or of reduction processes during ambient exposure to CO [281]. Other origins of spectral variations in the Mn *L*-edge were ascribed to changes in the Mn^{3+}/Mn^{4+} ratio and in the crystal field strength [283]. Our results suggest that a certain amount of Mn^{2+} is present at the surface of nanoislands, but a number of tests, left for future work would be needed to ascertain such hypothesis. One could i) check whether upon annealing under different oxygen partial pressures the low-energy peak changes, ii) perform the PEEM experiment on different days and check for variations in the ambient-sensitive Mn^{2+} peak (the present measurements were performed two months after the sample synthesis), iii) check the low energy peak of the oxygen *K*-edge (~ 530 eV), which is related to the hybridization of O *2p* orbital with the Mn *3d* orbitals. A hypothetical decrease in the intensity of such peak could be related to a higher *3d* level occupancy due to the presence of Mn^{2+} . In fact, we did attempt this latter study but our oxygen spectra did not yield any useful information, mainly due to the small intensities we were dealing with. Also, note that mirrors (and other objects along the beam trajectory towards the sample), have oxygen contamination: the oxygen spectral features of our sample were thus not clearly discernible from those caused by absorption processes before reaching the sample.

Comparison of $(001)_{\text{LSMO}}$ and $(111)_{\text{LSMO}}$ nanoislands

One of the strengths of PEEM regarding nanostructured samples is that, because of its space resolution, it allows one to identify, select, and study distinct features. We exploited this potential for the individual study of the spectral shapes corresponding either to $(001)_{\text{LSMO}}$ -oriented and $(111)_{\text{LSMO}}$ -oriented nanoislands. The former constitute the majority of the population, with square-base truncated pyramidal shape and $(111)_{\text{LSMO}}$ inclined facets [we

referred to them in the description of the shadow origin in Fig. 5.11 (a)]. The $(111)_{\text{LSMO}}$ nanoislands, by contrast, are the triangular-base nanoislands, which we have already introduced in the previous chapters. As they are different both in morphology and crystal structure, we aim now at verifying whether there is a sizable difference in their chemistry. Fig. 5.12 (a) shows a PEEM image taken at the Mn L_3 -edge with circularly polarized light. We show this image because it facilitates the identification of nanoislands in terms of square or triangular. The XAS data displayed in Fig. 5.12 (c), however, are calculated from measurements with linear polarized light, the same kind of measurements done to calculate the XAS data shown in Figs. 5.10 and 5.11. Islands that could be distinguished unambiguously are marked in red (square nanoislands) and blue circles (triangular nanoislands) in Fig. 5.12 (a), and are the ones used for building the laterally-resolved spectra on the right. The small differences between squares and triangles we can observe in the spectra of Fig. 5.12 (c) spectra are of the same order as the differences that arise from one individual island spectrum to another, regardless of its geometry. Thus, no measurable differences emerge from the Mn spectra of these two types of nanostructures. Note that, although a little noisier, the Mn island surface and bulk L -edges here presented show the same trends as depicted in the previous XAS analysis.

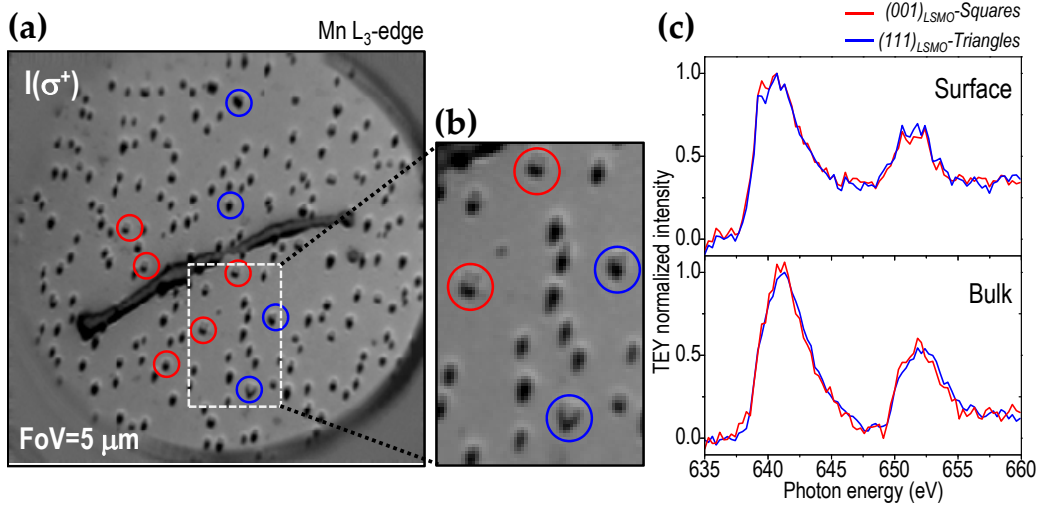


Fig. 5.12: PEEM analysis of $(001)_{\text{LSMO}}$ and $(111)_{\text{LSMO}}$ -oriented LSMO nanoislands reveals no differences in their chemistry. (a) $5\ \mu\text{m}$ field of view image taken at the Mn L_3 edge with circularly polarized light. A few recognizable square and triangular islands appear within red and blue circles, respectively. (b) Enlarged image of the area marked with dashed lines in (a). (c) Mn L -edge XAS corresponding to the square and triangular islands, further separated in terms of their surface and bulk contributions.

La M -edge

Contrary to the Mn L -edge, the XAS features of the lanthanum M -edge, which involves $3d_{5/2}, 3d_{3/2} \rightarrow 4f$ transitions, reveal little of the specific chemical composition of LSMO. This is mainly because of the great valence stability of the lanthanum ion, which exhibits a single oxidation state, La^{3+} . Fig. 5.13 (a) shows the PEEM image, after normalization, taken at the La M_5 -edge. As for Mn, this image is also the result of 10 merged images. The

XAS at the right side show the surface (top panel) and bulk (bottom panel) contributions obtained by selecting either *island* or *shadow* regions, respectively. We have also plotted the TEY spectrum from the literature corresponding to lanthanum in LaAlO_3 , where La displays the same 12-fold coordination as in LSMO [287]. One can notice that there is a considerable difference between the intensities of the M_5 and M_4 peaks. Otherwise, the main information we extract from the lanthanum XAS is the presence of La on the substrate surface. This is consistent with the observation that the substrate exhibits residual material in the form of small dots [see the AFM topography image in Fig. 5.13 (c)]. As we saw in Chapter 3, such material diffuses towards the islands upon longer annealing times and higher temperatures.

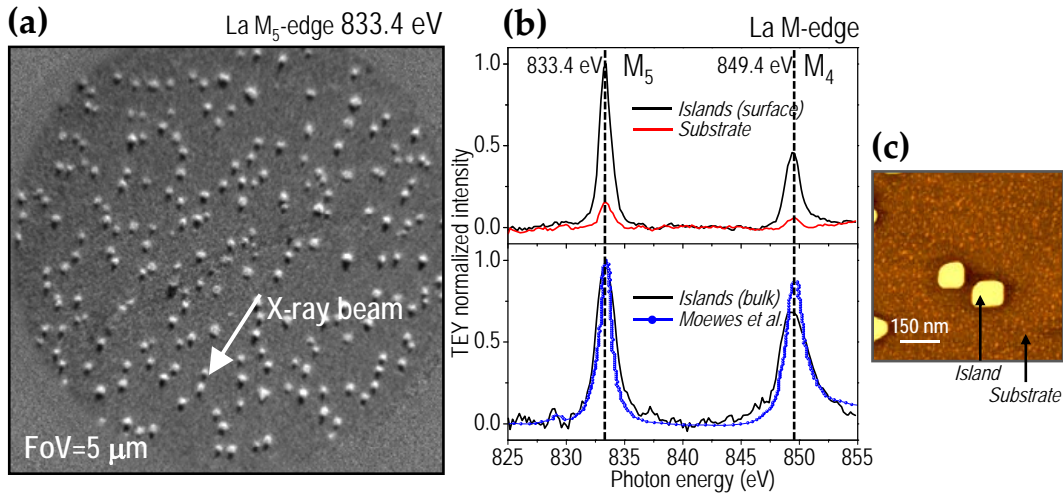


Fig. 5.13: (a) PEEM 5 μm field of view image taken at the La M_5 -edge showing the bright and dark contrasts characteristic of our experiments. (b) La M -edge XAS of the island surface (top panel) and bulk (bottom panel). The absorption spectra show no significant differences. A La M -edge for LaAlO_3 is also plotted for comparison [287]. Analysis of sites without islands reveal the presence of lanthanum on the substrate surface. This is in agreement with the AFM study of the sample (c), which reveals residual material on the substrate surface.

In summary, throughout this section we have investigated the manganese L -edge XAS of LSMO self-assembled nanoislands on YSZ. The small nanoisland sizes (t below ~ 40 nm and D below ~ 200 nm), along with the X-ray 16° incidence angle, have made the nanoisland surface and its bulk contribution separately accessible. Thanks to this fact we can confirm that the majority of the island, corresponding to the bulk contribution, displays the manganese XAS expected for bulk LSMO. Hence this result supports our assumption, in the previous chapters, that the ferromagnetic signal obtained from SQUID and MFM measurements effectively stems from the actual $\text{La}_{0.7}\text{Sr}_{0.3}\text{MnO}_3$ compound. Meanwhile, a certain de-oxygenation has been detected on the surface of the nanoislands, evidenced by means of a slight peak at low energy values, which suggests Mn^{2+} formation. This could be related to the loss of magnetic moment obtained from macroscopic SQUID magnetometry, i.e. to the dead layer concept we introduced in previous chapters. The individual chemical analysis of $(001)_{\text{LSMO}}$ and $(111)_{\text{LSMO}}$ -oriented nanoislands, has shown that no detectable differences exist between the two populations. Finally, lanthanum M -edge XAS has shown no remarkable features but for the detectable presence of La on the YSZ substrate. The latter is in agreement with the presence of small particles between the LSMO

nanoislands shown by AFM measurements.

5.1.4 Magnetic analysis: the limits of XMCD in nanoscale metal-coated LSMO nanoislands

Now that we have investigated the absorption spectra for individual and LSMO nanoisland ensembles, we move on to study their magnetism. As we explained in section 5.1.1, we collect PEEM images at the Mn L -edge with circular-polarized light of opposite helicities. The result of subtracting two images taken with opposite helicities, the so-called *asymmetry image* (Eq. 5.4), will reveal the ferromagnetic contrast present in our sample. One should keep in mind that the intensity of such contrast goes like $I \sim I_0 \cos \alpha$, with α the angle between the sample magnetization vector and the light helicity vector. Hence, if the magnetic moments, despite being in-plane, they are oriented 90° with respect to the X-rays, the contrast will be null. In order to enhance the contrast as much as possible, we saturate the samples in-plane, prior to inserting them in the PEEM chamber, using a 1 T permanent magnet. Then, in remanence after retiring the magnet, we place the sample in the magnetic sample-holder, making sure that the saturation direction is parallel to the in-plane projection of the 16° impinging light. Fig. 5.14 shows a schematic diagram of how the sample is located with respect to the X-rays and to the coils of the magnetic sample-holder.

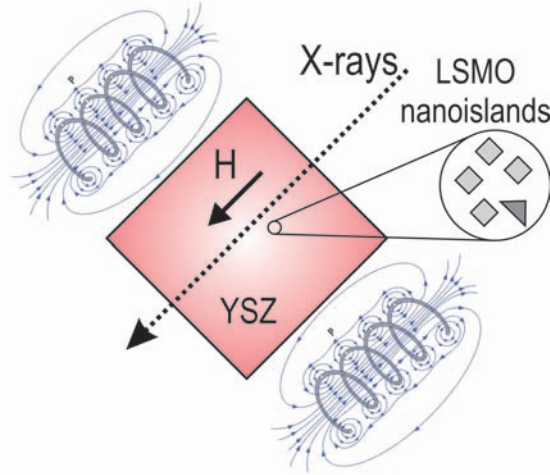


Fig. 5.14: Illustration of the sample placed with respect to the incident X-rays and to the magnetic field H generated by the sample-holder coils.

XMCD at room temperature

Our LSMO/YSZ self-assembled nanoislands are ferromagnetic, as we have seen by SQUID magnetometry and MFM. Fig. 5.15 shows the hysteresis loop, at 300 K, of the 0.03 M 900°C heat-treated LSMO/YSZ nanostructured sample that we will study with PEEM. We place it on the sample-holder with no applied field. Considering the magnetic volume derived from the estimated thickness ($t_{eq} \sim 3.5$ nm), the magnetization takes a value of ~ 308 kA/m

at saturation ($\sim 2.7 \times 10^{-5}$ emu, see Chapter 3). At zero applied field, in contrast, the magnetic moment value falls a $\sim 80\%$ from its saturation value, i.e. down to ~ 57 kA/m. A maximum field of ± 178 Gauss was applied for room temperature measurements. For these field values, according to the macroscopic magnetization loops, the magnetic moment exhibits a value of $1.9 (\pm 0.1) \times 10^{-5}$ emu (~ 217 kA/m); the ± 0.1 error stems from whether we are on the upper or lower branch of the loop. Hence, the drop from saturation is now of $\sim 30\%$. Although notably improving with respect to the remanence regime, we do not achieve complete saturation of the sample with these fields.

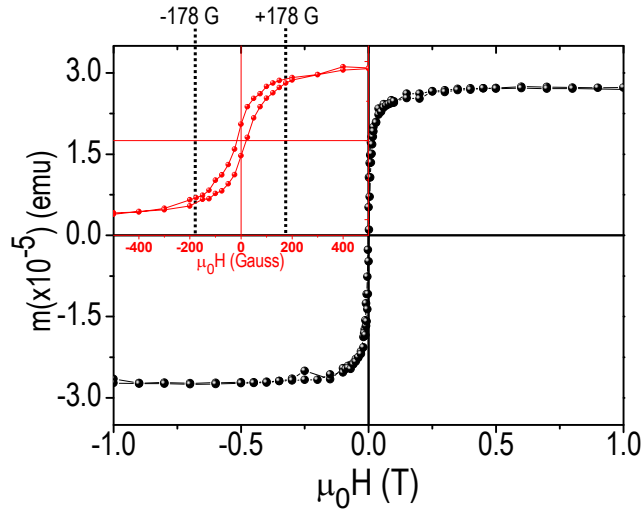


Fig. 5.15: Magnetic moment vs. magnetic field hysteresis loop at 300 K for the LSMO/YSZ nanostructured sample measured by PEEM (0.03 M, 900°C heat-treated). The field was applied in-plane. The augmented view of the center region is displayed on the inset, in red. The signal decrease from saturation is of $\sim 80\%$ for remanence, and of $\sim 30\%$ for the maximum 178 G applied field within the PEEM.

The result of XMCD measurements in **remanence** are shown in Fig. 5.16. For each XMCD image (1 stack), we recorded 60 images with one helicity and other 60 images with the opposite helicity, with an exposure of $\Delta t = 3$ s per image. Fig. 5.16 (a) displays the PEEM image at the Mn L_3 -edge taken with left-handed circular polarized light, after merging 7 different stacks collected in the above mentioned way. Thus, Fig. 5.16 (a) is the result of averaging 420 images. To this image we subtract the opposite helicity image, identically obtained, which yields the XMCD image of Fig. 5.16 (b). In the red-blue color scale, red indicates magnetic moments \vec{m} oriented antiparallel to the X-rays (negative contrast), and blue means that \vec{m} is parallel to the incident light direction (positive contrast). White indicates no magnetic contrast.

Some of the nanoislands evidenced by small squares in Fig. 5.16 (a) appear in the corresponding XMCD image as dark-blue spots, which is the evidence of the ferromagnetic nature of islands. A careful inspection of the images allowed us to determine that the blue contrast in Fig. 5.16 (b) stems from the shadows of Fig. 5.16 (a). Recall that the intensity of the transmitted signal (the shadow) is twice as large as the intensity coming from the island surface. Hence, it is reasonable to think that the signal we observe is in fact the difference between the two more intense signals, i.e. those coming from the transmission. Note that, since the transmission signal is identical but opposite in sign to the absorption

signal, the XMCD will also be opposite in sign. In other words, if blue contrast means magnetic moments parallel to the incident light, the islands we observe in Fig. 5.16 (b) are magnetized antiparallel to the X-rays. The line scan across an individual nanoisland, Fig. 5.16 (c), shows that the amplitude of the signal is only ~ 3.3 times the noise peak-to-peak amplitude, despite the large number of scans we have averaged. Regarding the XAS measurements, the intensity signal we measured was barely a 5% of the total available intensity, due to the Pt coating. The magnetic signal is now a $\sim 20\%$ of that 5%, i.e., a $\sim 1\%$ of the total signal. We are therefore very close to the detection limit.

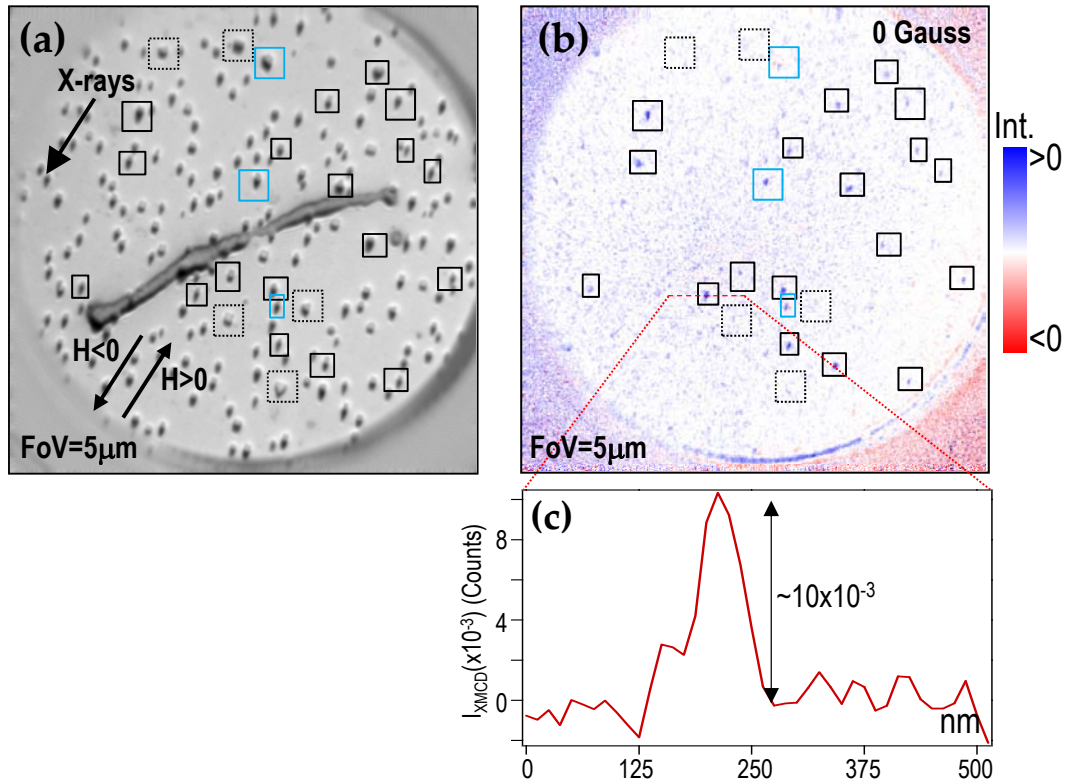


Fig. 5.16: (a) $5\ \mu\text{m}$ field of view PEEM image taken with left-handed circular polarized light. (b) Remanence XMCD image of the region in (a), after ex-situ saturation of the sample. The islands giving ferromagnetic contrast are marked inside black squares. Some examples of large islands giving no XMCD signal are indicated with dashed-line squares. Within light-blue squares we have marked a few islands showing simultaneous blue and red contrast (see text). (c) Line profile showing the intensity of the signal at one of the blue-contrast islands (red dashed line in (b)).

We know from SQUID magnetometry that the magnetic signal in remanence is very low, $\sim 57\ \text{kA/m}$. By XMCD too, it appears that few of the islands (in blue) are contributing to the magnetic signal parallel to the initial saturation field. We cannot properly tell the inner distribution of the magnetic domains in such islands, e.g. whether they are single domain or multidomain, because of the limited resolution. This limit can be estimated by the smallest lateral size of the observed contrasts, which is around $\sim 150\ \text{nm}$ [see Fig. 5.16 (c)]. Considering the exceedingly small signal, and the loss of precision in the island shapes caused by the Pt capping, even achieving such a resolution is quite remarkable. Other islands give no contrast, presumably because their magnetic moments are oriented

90° with respect to the incident light. Finally, a few islands displaying both blue and red contrast have been marked inside light-blue squares in Fig. 5.16 (b). Note that this *double contrast* is related to individual islands, i.e. from the correspondence between Fig. 5.16 (a) and Fig. 5.16 (b) we can rule out the possibility that it might originate from two different adjacent nanostructures with opposite magnetic moments. In fact, there are no isolated red islands: in remanence, none of the islands have reversed magnetization. The red contrast we observe appears next to the blue contrast of the same island. Such a contrast fits well with an in-plane swirling magnetic configuration, i.e. with a vortex flux-closure state. We shall come back to this point later on.

By applying **in-plane magnetic field** we expect to change the magnetic configuration of the LSMO nanoislands. From the averaged SQUID data (Fig. 5.15) we expect a significant increase in the magnetization signal with applied magnetic field; such increase should be somehow reflected in the XMCD contrast. Fig. 5.17 (a) shows the XMCD image, at the Mn L_3 -edge, that results under an in-plane applied field of 178 Gauss. Since the contrast we observe is positive we know from $I \sim I_0 \cos(\alpha)$ that magnetic moments and incident X-rays are parallel. As these magnetic signal comes from the *island shadow*, however, what we have in reality is the magnetic field applied anti-parallel to the X-ray beam. Note that, compared to Fig. 5.16, a greater number of dots appear with the blue contrast here: the magnetic field enhances the alignment of the magnetic moments. However, the contrast is quite weak and noisy. This is because the images in Fig. 5.17 are averages of two stacks of images, instead of the seven stacks used for Fig. 5.16. When we switch the applied field direction, Fig. 5.17 (b), we observe a reverse in the contrast: nanoislands are now seen as red spots. This provides further evidence on the ferromagnetic origin of the contrast. The line scans below each PEEM image display this reversal in terms of a change from positive to negative signal, implying that the relative orientation of magnetic moments with respect to the light has reversed.

It is also noteworthy that Fig. 5.17 (b) appears noisier than Fig. 5.17 (a) (the red spots are harder to detect from the background). This loss of contrast is further evidenced in the decrease of intensity (from 14×10^{-3} to 10×10^{-3}) observed in the line scan. A possible reason for this loss could be that the field we are applying is not really -178 Gauss but somewhat less, caused by some remanent magnetic field at zero applied current. Another source of contrast loss could be some kind of *sample damage* due to the prolonged exposure of the region to continuous radiation. This particular region was exposed to no less than 1.5 h of X-ray irradiation, since the first image of Fig. 5.17 (a) until the last of Fig. 5.17 (b). We shall discuss this point in the following.

Influence of X-ray irradiation time on the XMCD signal

A potential loss of magnetic signal with increasing X-ray sample irradiation is not a minor issue. We cannot expect to address physical changes in the magnetic signal of our LSMO nanoislands with varying magnetic field, if such variations are, in part, due to the signal degradation caused by X-rays.

Fig. 5.18 displays the lower left-corners of the images that comprise the XMCD image of Fig. 5.16 (b) (recall that the latter is the result of merging 7 XMCD images collected in sequence). Each of the 7 images of Fig. 5.18 have a line scan corresponding to one individual island. We observe that there are fluctuations in the intensity of the magnetic signal of the island investigated, but these are random fluctuations, i.e. there is no monotonic decay

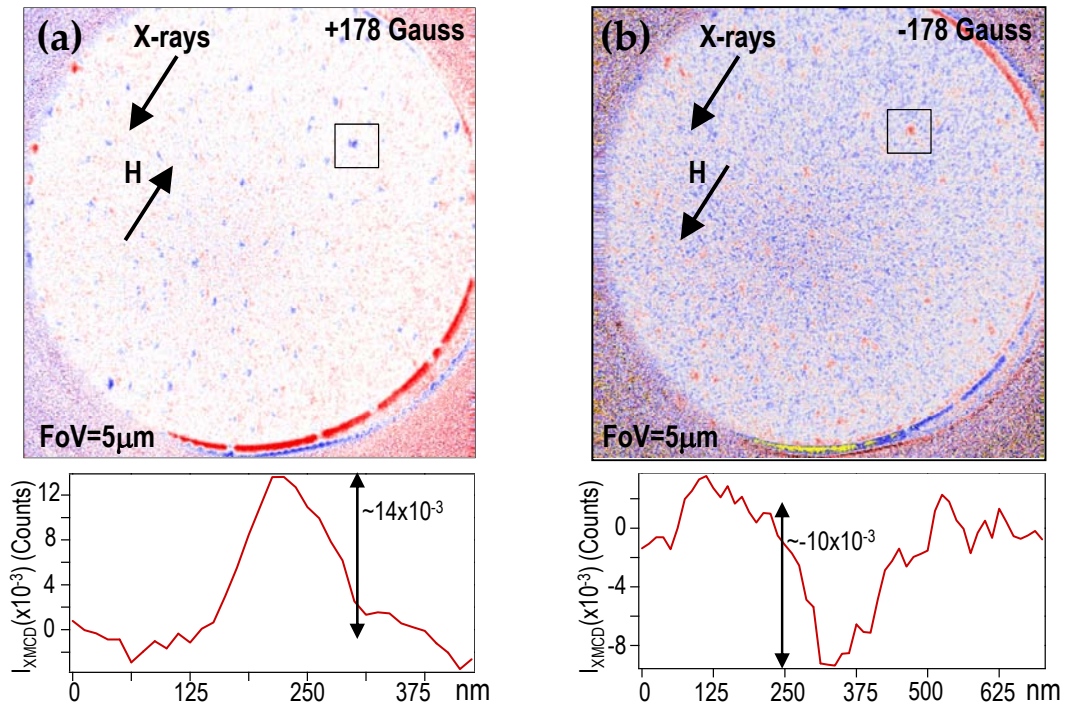


Fig. 5.17: (a)&(b) 5 μm field of view XMCD images taken with opposite applied fields of ± 178 Gauss. The change of field direction is accompanied by a change in the magnetization direction of nanoislands. This is evidenced by a blue to red contrast change and the associated sign reversal in the line scan.

of the intensity that could suggest a gradual loss of the signal. We can thus conclude that, throughout the ~ 45 min of continuous irradiation from image 1 to image 7, the X-rays do not affect the magnetism of the islands.

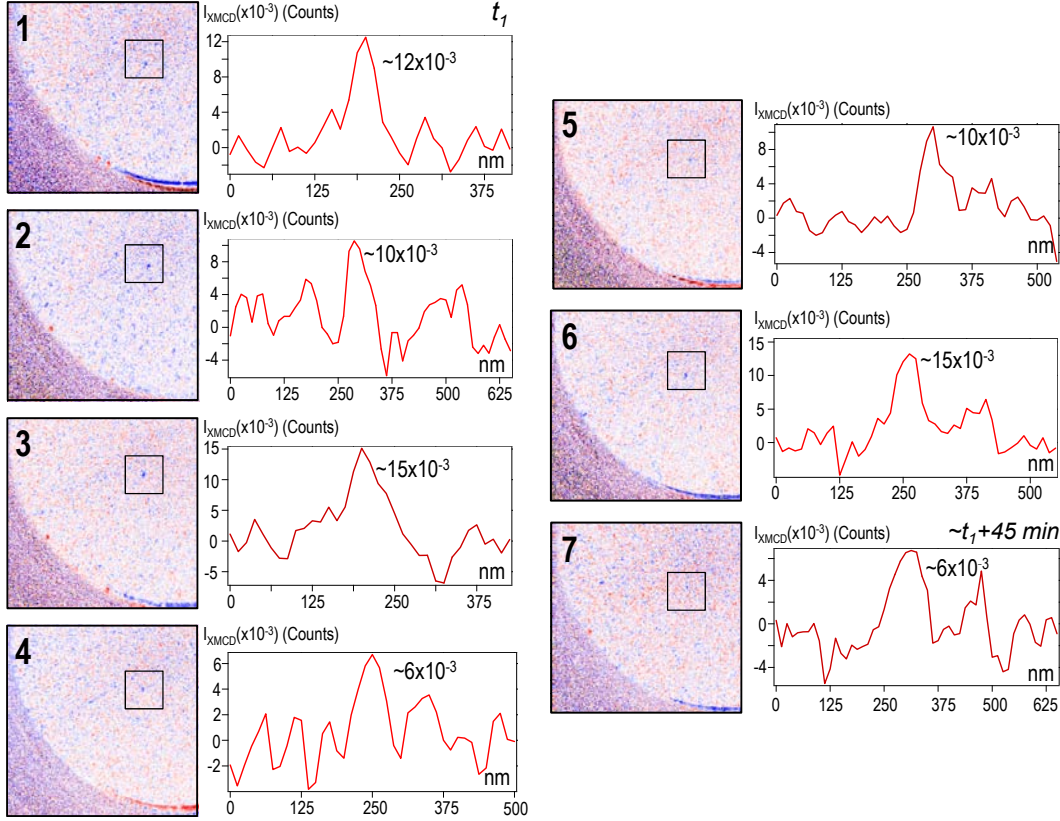


Fig. 5.18: Left-bottom corner of each of the 7 images that conform Fig. 5.16 (b), numbered in chronological order. The set of accompanying line-scans express the intensity evolution of the XMCD contrast with time, corresponding to a single island (marked within black squares).

If we now study what happens after longer exposure times, however, we find conclusive evidence that the XMCD signal can completely fade away. On the left hand side of Fig. 5.19 we have the same XMCD image as shown in Fig. 5.16 (b), displaying the nanoisland contrast at zero applied field. On the right, the same sample spot is imaged, at 178 Gauss, after a large number of experiments were done in between. We have estimated that the area was exposed to X-ray irradiation for a total of ~ 15 h, with 2 breaks of a few hours in between due to the synchrotron beam injection. The sample was therefore steadily illuminated for about 7 h. The result of such exposure is the total loss of XMCD signal in the area, even at an applied field of 178 Gauss. Besides, by moving the illuminated spot to other sample regions, we regained the XMCD signal. Hence, the apparent *sample damage* after such long exposure times is due to X-ray irradiation.

Next, we want to check whether upon X-ray irradiation there are sizable changes in the chemical spectra of manganese. If we compare the Mn *L*-edge XAS features of a group of nanoislands at a certain time and ~ 45 min after continuously irradiating the same spot, we observe no relevant differences [see Fig. 5.20 (a)]. This is in agreement with the fact that no magnetic signal loss was observed after ~ 45 min of steady irradiation. Fig. 5.20

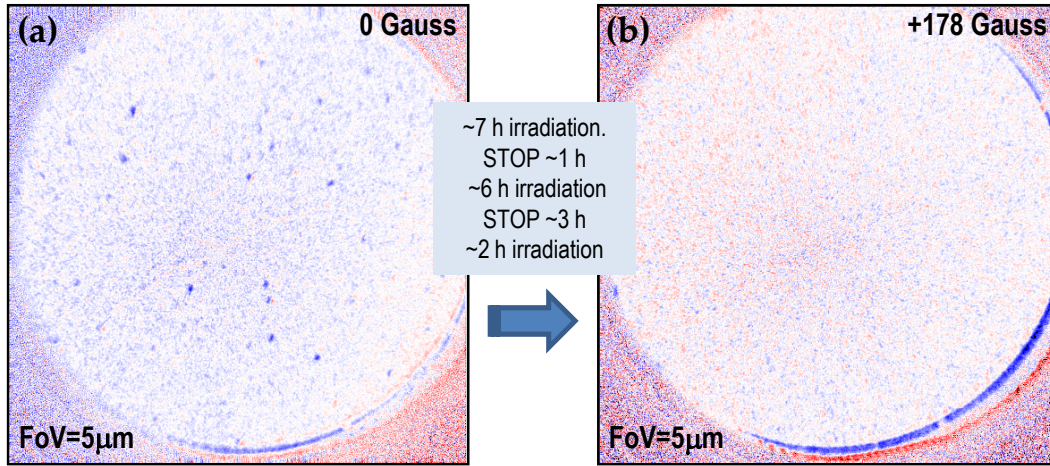


Fig. 5.19: (a)&(b) 5 μm field of view XMCD images of the same sample spot showing the loss of magnetic signal upon 7 h of continuous X-ray irradiation.

(b), in turn, compares the Mn L_3 -edge XAS for a nanoisland ensemble at a moment when XMCD signal was measurable, with a XAS of the same group of nanoislands at an instant when the signal was no longer detectable (after 7 h of irradiation). Although for fine-structure considerations a better signal to noise ratio is required, it appears evident that the Mn L_3 -edge is still present after having lost the magnetic signal. Furthermore, we do not find a decrease in the signal intensity nor the low-energy peak, at ~ 639.2 eV, characteristic of Mn^{2+} formation. Hence, apparently, the lack of magnetism is not caused by having chemically altered the manganite.

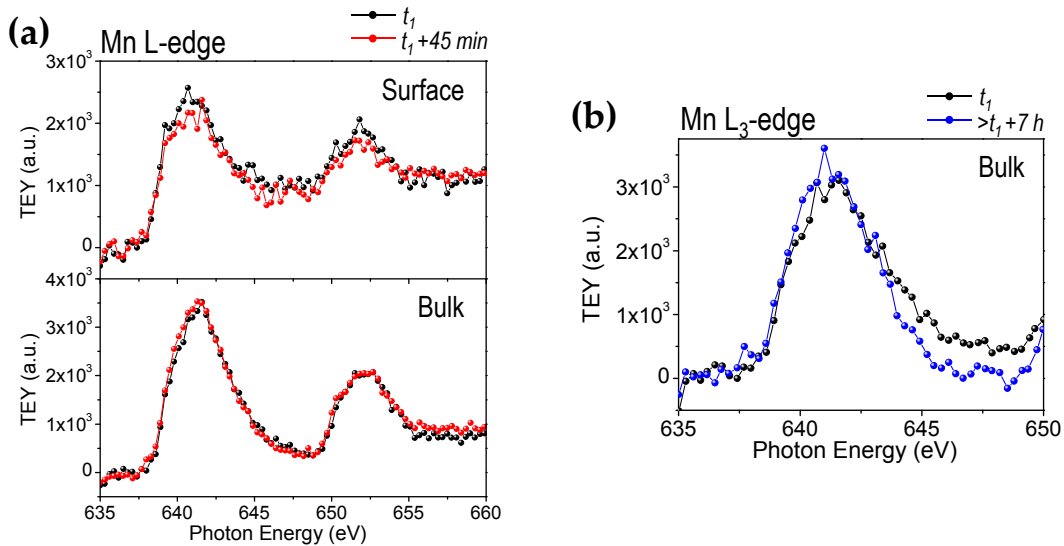


Fig. 5.20: (a) Mn L -edge XAS of a LSMO nanoisland ensemble after X-ray irradiation during ~ 15 min (t_1 , black) and ~ 60 min ($t_1 + 45$, red). The spectra exhibit no appreciable variations. (b) Mn L_3 -edge XAS of a LSMO nanoisland ensemble after X-ray irradiation during ~ 15 min (black) and for more than 7 h (blue).

After the previous results, we can now think of a different mechanism that could lead

to the fading of the magnetic signal. Pt is a good thermal conductor, with thermal conductivity values of around $\kappa_{Pt}(300\text{ K}) \sim 71.6\text{ W/m}\times\text{K}$ [288], and it is hence expected to easily lead the X-ray power, in the form of heat, into the LSMO nanoislands, which have a poor thermal conductivity of $\kappa_{LSMO}(300\text{ K}) \sim 2.4\text{ W/m}\times\text{K}$ [289]. The heat within the small LSMO nanoisland cannot easily dissipate since islands stand on top of an extremely good thermal insulator, YSZ[¶] [$\kappa_{YSZ}(300\text{ K}) \sim 2.2\text{--}2.6\text{ W/m}\times\text{K}$ [290]], and thus the nanoisland is expected to rise its temperature a lot, which would not happen if it were epitaxially grown onto a metallic substrate. Therefore, LSMO nanoislands under prolonged X-ray irradiation could undergo the ferromagnetic to paramagnetic transition, by being heated above their Curie temperature $T_C \sim 350\text{ K}$.

XMCD at 110 K

The interest of measuring our LSMO nanoisland system at low temperatures is two-fold: on one hand, the magnetic signal is stronger below 300 K, so we expect to enhance the faint magnetic contrast we obtain at room temperature (RT). On the other hand, this study will clarify whether the magnetic signal loss observed at RT is effectively caused by heating the LSMO above its Curie temperature. Our experimental set-up allows us to reach a minimum temperature of 110 K. The magnetic hysteresis loop of the LSMO nanoisland ensemble (0.03 M) at 110 K, as measured with SQUID magnetometry before the PEEM experiments, is plotted in Fig. 5.21. The saturation magnetic moment is $\sim 4.6 \times 10^{-5}\text{ emu}$ ($\sim 526\text{ kA/m}$) while, in remanence, the magnetization value drops a $\sim 50\%$ from the saturation value.

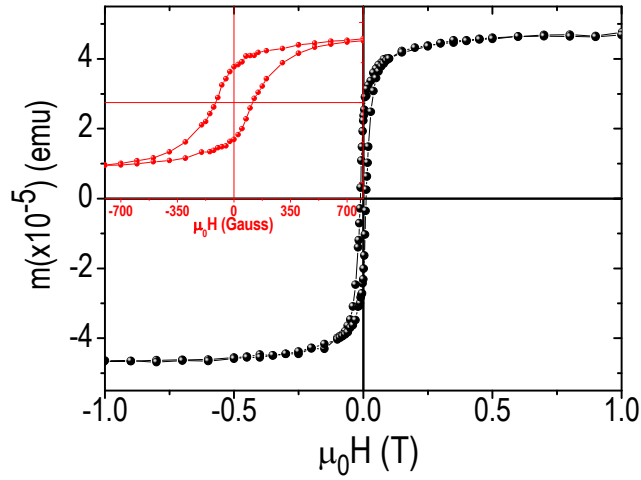


Fig. 5.21: Magnetic moment vs. magnetic field hysteresis loop at 110 K for the LSMO/YSZ nanostructured sample measured by PEEM (0.03 M, 900°C heat-treated). The field was applied in-plane. The augmented view of the center region is displayed on the inset, in red. The signal decrease from saturation is of $\sim 50\%$.

Fig. 5.22 (a) displays a $5\text{ }\mu\text{m}$ field of view PEEM image taken at the Mn L_3 -edge. The interesting thing about this image is that the Pt capping has worn out a little, in the form of horizontal scratches; this results in a greatly increased brightness for nanoislands next to

[¶]The low thermal conductivity of YSZ makes it the material of choice for thermal barrier coating applications, where the ceramic is required to protect metallic parts of engines subject to very high operational temperatures of around 1200°C.

these scratches. One can notice, in the areas where the capping layer is intact, that the island and shadow contrast is identical to that shown earlier in the chapter (a representative island with its associated shadow is indicated in the figure). Conversely, near the thinned Pt, the island surface signal is remarkably improved, confirming the critical role of the capping in the collected electron intensity. Note also that the shadow can still be detected next to the bright islands, as expected, since its origin is exclusively due to the grazing X-ray angle and the nanoisland geometry. The direction of the incident light, as well as the two possible application directions of the magnetic field, are depicted in Fig. 5.22 (a).

Fig. 5.22 (b) shows a 3 μm zoomed XMCD image, taken in remanence, of the region marked within dashed white lines in Fig. 5.22 (a). We have numbered some of the large islands in both images, to better see the image correspondence. With respect to our RT measurements, the present low T XMCD image shows a considerable contrast enhancement. Note that the most intense contrasts, those of the large triangular islands, coincide with the scratched-capping sites. For the islands located below the numbered islands, the contrast is notably weaker. Nevertheless, even at these sites we can easily discern many double spots, aligned with the light direction, and with opposite colors. These double spots correspond to a single island, in particular, to the island and the island-shadow. This confirms our previous hypothesis that the contrast arising from island and island-shadow should be opposite, with the difference (with respect to RT measurements) that we are now able to see them both, thanks to the enhanced intensity conditions. Note that not all of the nanostructures exhibit the same island and island-shadow sizes; this depends on the specific nanoisland geometry and orientation. In fact, for the islands at the very thin Pt capping sites (the scratches) the shadow loses relevance with respect to the bright island signal, and we mostly observe a single large spot coming from the island [some of these single spots have been marked with stars in Fig. 5.22 (b)]. In the following, we will refer exclusively to the contrast arising from the island, not from the island-shadow.

Along with the double-spots we have just described, we find single islands giving adjacent blue and red double spots, for instance the triangular nanostructure numbered 3. Instead of one on top of the other, these spots are located one next to the other, perpendicular to the X-ray incidence direction. Such contrast arrangement is in agreement with two antiparallel magnetization vectors, next to each other, characteristic of a magnetic vortex. The perpendicular magnetic moments necessary to achieve the flux-closure configuration, being 90° oriented with respect to the X-rays, give no contrast. We have therefore the evidence of magnetic vortices in some of these nanoislands, which we already suggested in the RT results. Furthermore, we have the first confirmation that the magnetic configuration of triangles may also be that of a vortex. Remember that, by means of Magnetic Force Microscopy, we could not resolve their magnetic structure due to the influence of the tip, which wiped the magnetic domains within the triangles back and forth upon scanning (Chapter 4). Some of the vortices (V) are indicated with red squares in Fig. 5.22 (b). The rest of the nanoislands exhibit either a blue or a red contrast, characteristic of a single domain (SD) state (some of them are also marked with squares). It is highly possible that these apparently uniform contrasts might comprise a mixture of differently oriented domains (i.e. a multidomain structure), considering the large size of some of those islands. However, detecting these variations is beyond our experimental resolution.

In addition to an enhanced magnetic contrast, no critical magnetic contrast loss was detected upon continuous X-ray irradiation of the same spot at low temperatures. We can thus confirm our hypothesis that the X-rays are not intrinsically damaging the LSMO but

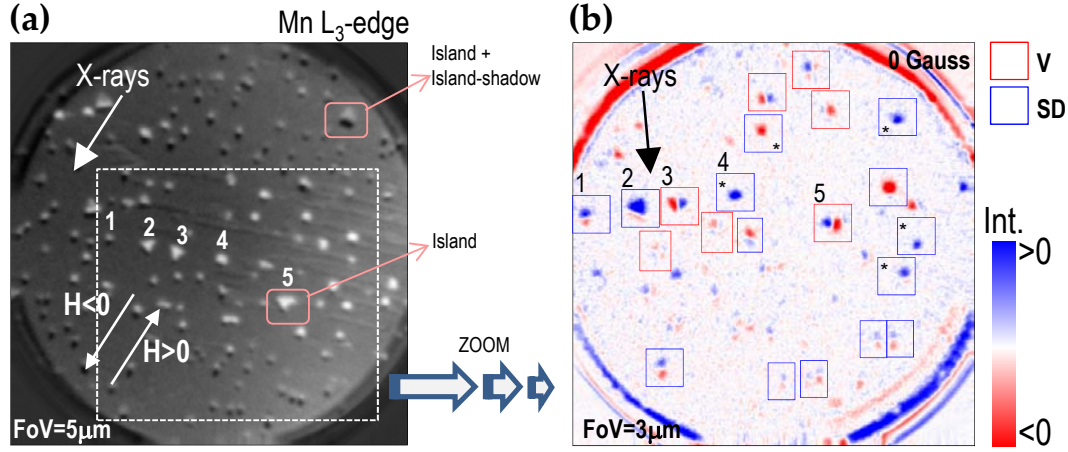


Fig. 5.22: (a) 5 μm field of view PEEM image at the Mn L_3 -edge showing a large increase in the intensity signal at the central part, i.e. where a thinning of the Pt capping occurred. (b) Remanence XMCD image of the zoomed-in region, approximately indicated with dashed lines in (a). Numbered nanostructures serve as reference with respect to (a). Vortex configurations (V) and single domain configurations (SD) can be distinguished. Some representative examples are marked within red and blue squares, respectively.

producing a temperature gradient that makes the system non-ferromagnetic when measured at RT. Therefore, we may now safely study the changes in the magnetic configuration of individual nanostructures under applied field. This time, magnetic fields up to ± 700 Gauss could be applied within the PEEM chamber. The maximum field applied in the course of imaging was, nevertheless, ± 350 Gauss.

Fig. 5.23 exhibits a number of XMCD images of the same spot taken at different stages throughout the magnetic history of the sample. The XMCD image in the top row, taken in remanence, corresponds to the same region shown in Fig. 5.22 (b). Some representative vortex and single domain configurations are marked with red and blue squares, respectively. The sample was previously saturated with a negative field ($H < 0$). This can be deduced from the fact that the majority of the single domain islands we observe in remanence show a blue (positive) contrast, which indicates magnetic moments aligned parallel to the incident X-rays [i.e. $H < 0$, see Fig. 5.22 (a)]. The three XMCD images of the bottom row were taken at the same magnetic field, ~ 260 Gauss, but at different times, i.e. following different magnetic states. The sequence that was carried out is illustrated by A, B... letters on different points of the 110 K macroscopic hysteresis loop of the sample, indicating the magnitude of the field and the order in which it was applied.

By increasing the magnetic field from 0 to +260 Gauss, opposite to the incident light, some of the nanoislands magnetic configurations undergo detectable variations. The same islands within squares in the remanence **A** image, are also marked with squares in **B**. Those showing detectable changes with respect to the previous image are marked with black solid lines, while the rest are enclosed in gray dashed squares. Notice, for instance, how the two islands named 1 and 2 in image **B** lose the blue contrast shown in **A**, under the influence of a +260 Gauss field opposite to their magnetization^{||}. This lack of contrast, even more evident in image **D**, could indicate that a coherent rotation demagnetization process is taking place, with the magnetic moments aligning close to perpendicular to the X-rays

^{||} Recall that we refer only to the island (not island-shadow) contrast.

at that particular stage. Even clearer is the vanishing contrast in island 3 of image **B** with respect to its blue contrast in **A**. Applying a considerably larger field, i.e. ~ 450 Gauss (point **C** in the hysteresis cycle), we achieve the total reversal of that island, which, going back to 260 Gauss (image **D**), does not regain the faint contrast of image **B**.

Regarding islands 4, 5, and 6 in image **B**, these were all vortices in the remanence image **A**. In the case of 5 and 6 they were already non-centered vortices, with non-compensated parallel and antiparallel domains. The domain parallel to the applied field (red) spreads to the whole nanoisland in **B**, until reaching a single-domain state. The vortex evolution is more clearly seen in nanoisland 4, where the applied field makes the red domain grow at expenses of the blue, but the vortex is not yet annihilated. In fact, this suggests that the vortex core movement (the middle part between blue and red), moves perpendicular to the applied field, as generally expected. The evolution of nanoisland 4 towards a single domain configuration is further evidenced in **D**. Other significant transformations one can observe include the total reversal, in image **D**, of the large triangular island 7: in the increase from 260 Gauss up to 450 Gauss and back to 260 gauss the nanostructure undergoes a 180° change in magnetization. Identical behavior, although only after reaching higher fields (~ 700 Gauss), is exhibited by island 11 in image **F**.

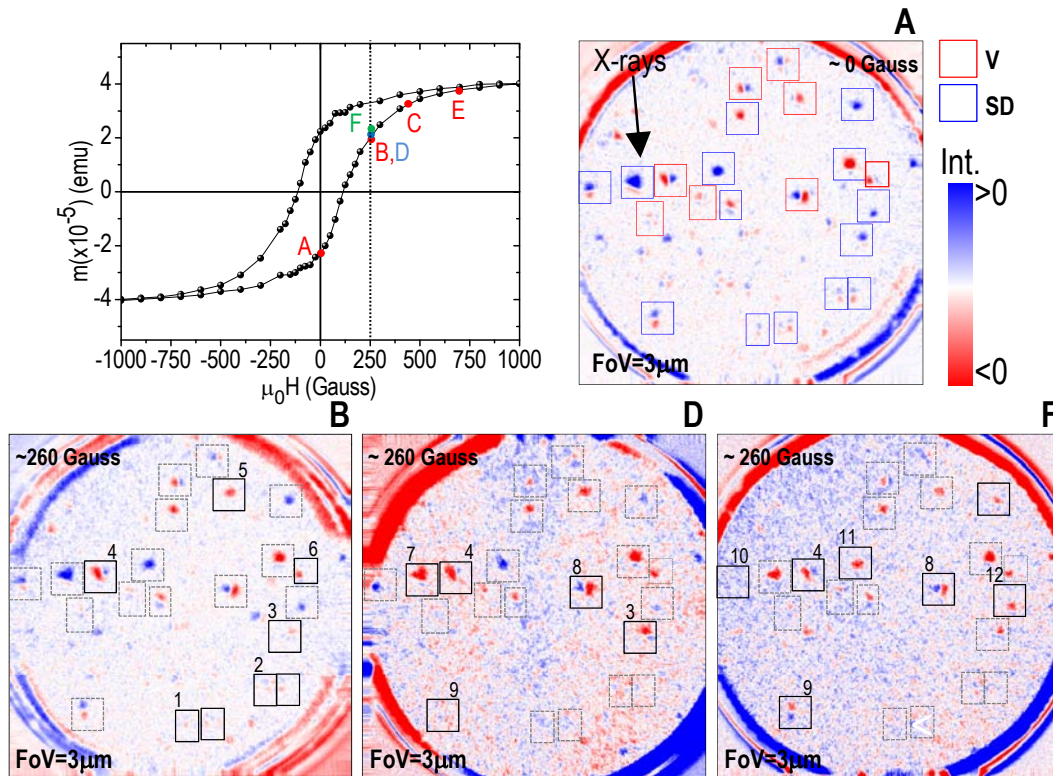


Fig. 5.23: XMCD study of the magnetic configuration evolution of LSMO nanoislands with applied magnetic field. Images are labeled A, B...etc. in chronological order and in correspondence with the applied fields pointed in the 110 K hysteresis loop. Black solid squares mark nanoislands that have undergone a transformation in their magnetic configuration with respect to the previous image, and gray-dashed squares mark those which remain the same.

Fig. 5.24 displays another set of XMCD images at various magnetic fields, as illustrated by the different points marked on the hysteresis cycle. The $5 \mu\text{m}$ field of view XMCD im-

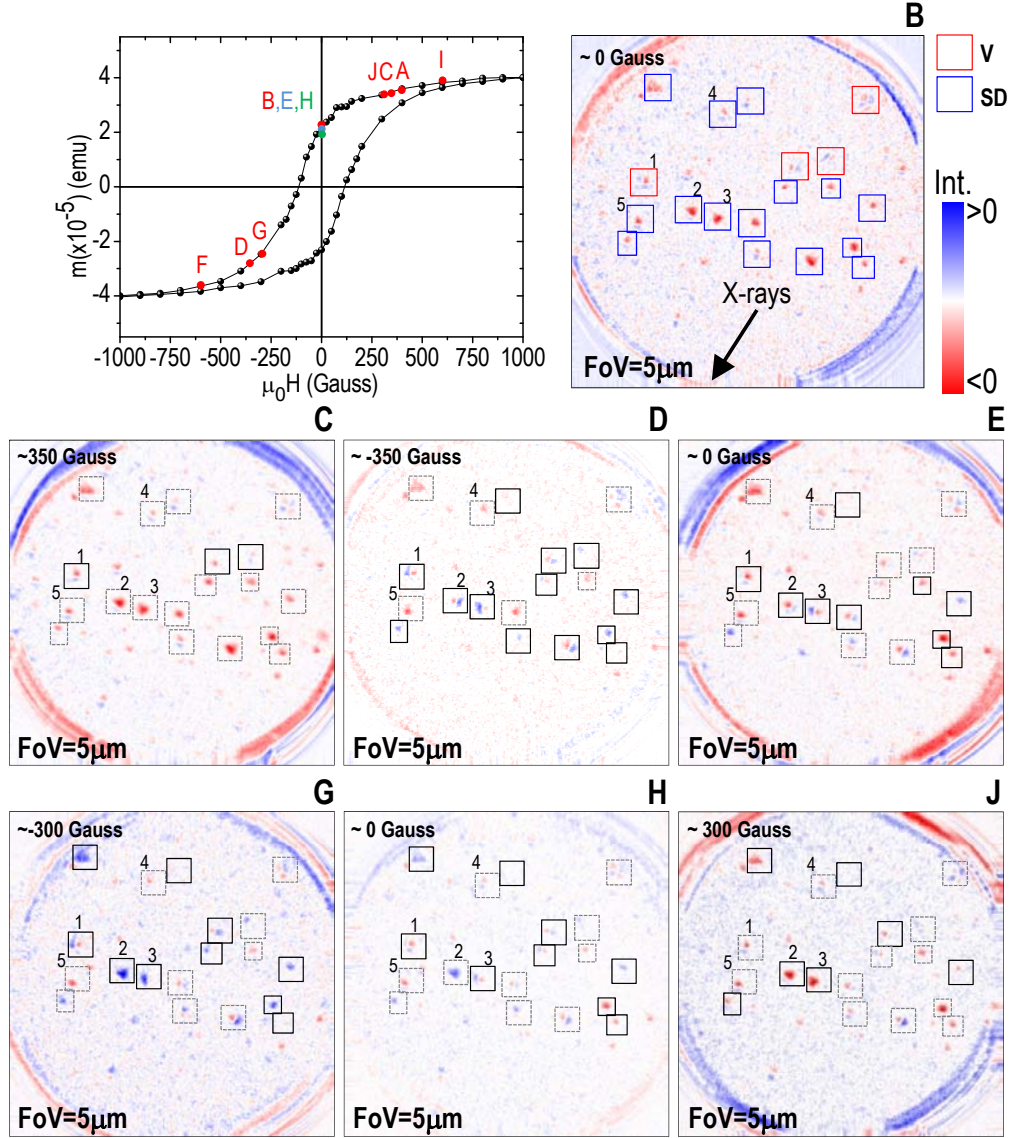


Fig. 5.24: Similar XMCD study as the one presented in Fig. 5.23, although now the fields do not surpass 350 Gauss and hence their corresponding XMCD image is measurable. Islands labeled 1, 2, and 3 are large triangles which exhibit easily detectable changes in their magnetic configuration. By contrast, islands 4 and 5 exemplify other smaller islands which show no appreciable change in their magnetic structure within the range of applied magnetic fields.

ages show the same PEEM image of Fig. 5.22 (a). Again, the islands that have changed their magnetic configuration with respect to the previous image are marked with solid black squares, and gray dashed-line squares denote those that remain unaltered. From the study of this set of XMCD images one can see that large triangular nanoislands, in the middle of the image, easily change their magnetic configuration upon application of a magnetic field. Take, for instance, nanoislands 1, 2, and 3. Nearly at every registered magnetic field variation we see a change in their magnetic configuration: from single domain to vortex, vortex evolution, reversed single domain etc. This behavior suggests a magnetically soft nanostructure, whose magnetic configuration is easily perturbed. During MFM imaging of triangles in Chapter 4, in fact, we also observed such “softness”, manifested in the influence of the magnetic tip on the nanoisland original magnetic configuration. At the other extreme we find examples like those of islands 4 and 5: they exhibit an initial red single-domain contrast, which, upon multiple changes in magnetic field direction and magnitude, does not suffer any detectable alteration.

In conclusion, the XMCD studies presented here highlight once more the rich variety of nanoscale magnetic behaviors exhibited by the solution-derived self-assembled LSMO nanoislands. This landscape can only be revealed from a nanoscale spatially-resolved technique that allows one to individually characterize each nanostructure, and identify details that appear hidden in the averaged macroscopic magnetometry measurements. This scenario was already extensively described in the previous chapter, devoted to the investigation of the nanoisland magnetic structure by Magnetic Force Microscopy. We there could correlate the nanoisland size and aspect-ratio to its preferential magnetic ground state. The present PEEM investigation, in turn, has allowed us to answer some of the questions that raised during the MFM study: for example, we have seen that triangular nanoislands can display a magnetic vortex configuration, and, additionally, the evolution of the contrast under an applied magnetic field is consistent with the expected behavior of a vortex core, i.e. is perpendicular to the field. Regarding the vortices in the square-shape nanoislands, which we saw in Chapter 4 to move parallel to the external field, we could not determine their behavior by PEEM. On one hand, it is not straightforward to characterize square islands displaying a vortex state (they tend to be smaller islands). On the other hand, a motion parallel to the field implies subtle contrast changes difficult to resolve. Once more, one should rely on micromagnetic simulations that take into account the real shape of the nanoislands. These, as already commented in Chapter 4, are currently in progress.

5.1.5 Conclusions

Along the previous pages we have explained and discussed the PEEM experiments and their results on the system of ferromagnetic self-assembled LSMO nanoislands on YSZ. Special emphasis was given to the metallic capping required to accomplish the measurements, since samples must be electrically conducting (YSZ is a good insulator) and because, as we showed here, a successful capping is crucial and not straightforward. After demonstrating the suitability of platinum against copper and aluminum, we have moved on to the XAS study of the manganite nanoislands. We have taken advantage of the geometrical shadow-effect caused by the 16° X-ray incidence angle impinging on the small nanoislands ($D \lesssim 200$ nm and $t \lesssim 40$ nm), to simultaneously and separately analyze their surface and bulk composition. We have thus seen that the Mn XAS within the nanoisland (the bulk part) exhibits the spectral features expected for stoichiometric $\text{La}_{0.7}\text{Sr}_{0.3}\text{MnO}_3$. In

contrast, there is evidence of a certain Mn^{2+} formation at the island surface, which supports the hypothesis of a superficial ferromagnetic dead layer on the LSMO nanoislands, discussed in previous chapters. It was also proved that, within experimental accuracy, the chemistry of the nanoislands does not depend on its crystallographic orientation. Magnetic measurements by means of XMCD have shown that the islands are indeed ferromagnetic. Nevertheless, we have seen that the Pt capping in such small nanostructures substantially reduces the intensity signal in the XMCD experiments, especially at high temperatures, where the magnetization value of manganite is small. The exposure to X-rays, for as long as seven hours and at room T , has been proved to heat the irradiated spot above the manganite T_C , with the corresponding loss of magnetic signal. In order to avoid the heating and to enhance the signal to noise ratio, we have performed experiments also at 110 K. The greater intensities, especially at places where the capping appears to have slightly worn out, has evidenced the presence of magnetic vortices in the $(111)_{\text{LSMO}}$ -oriented triangular-shaped nanoislands, which magnetic state was not accessible in the MFM experiments of Chapter 4 (recall that the tip stray field modified its magnetic configuration). Moreover, these vortices move, as theoretically predicted, perpendicular to the applied field. We have finally studied the magnetization processes of individual islands subject to different external magnetic field values. Our observations reveal that the variety of island shapes and sizes comprising the system of self-assembled LSMO nanoislands implies a correspondingly varied landscape of magnetization processes. It is also worth remarking that in the evolution of nanoislands with applied field there is no evidence that the magnetic state of an island should influence that of its neighbour islands. This agrees well with our hypothesis of Chapter 4 that the magnetic interaction between nanoislands is negligible. A more detailed study considering XMCD imaging at many different field values, given an island large enough to resolve its structure can, in a future work, provide full hysteresis cycles of individual LSMO nanoislands.

5.2 Kelvin Probe Force Microscopy study of self-assembled LSMO nanoislands

KPFM is the scanning force microscopy tool used for measuring the work functions of different metals with nanometer spatial resolution [291, 292]. The work function values of a metal are known to sensibly vary with contaminants, adsorbed layers, different reconstructions and defect structures on the surface, and such variations can be locally addressed with KPFM [293]. Increasingly during the past decade, the use of KPFM has been extended to other materials, being applied in the characterization of semiconductor nanostructures and devices [294–296] as well as to measure charge-related phenomena on insulating surfaces [297–300]. The precise mechanisms acting between the tip and the sample are often complex and difficult to understand, and hence the interpretation of KPFM results is not trivial and straightforward [301, 302]. In this section we focus on the KPFM study of self-assembled LSMO nanoislands on insulating YSZ substrates, detailing the experimental procedure and, from a critical perspective, analyzing the obtained results.

5.2.1 Basics on KPFM

KPFM measures the contact potential difference (CPD) between the sample and a sharp metallic tip placed a few *nm* above its surface. CPD (or V_{CPD}) is defined as the electric potential difference between two points in vacuum, each of them close to the surface of a different metal, while these metals are uncharged and electrically contacted. KPFM is a Scanning Probe Microscopy technique which relies on the Kelvin method [261]: when two metals, arranged in a parallel plate capacitor geometry as illustrated in Fig. 5.25, are contacted, electrons will flow from the material with lowest to the material with highest work-function, until the Fermi level of the two equilibrate [Fig. 5.25 (b)]. At that point, an electrostatic field develops between the two conductors. We can nullify this field by applying a certain voltage, V_{CPD} , which equals the work-function difference between the two materials, i.e. $eV_{CPD} = \Delta\phi = \phi_{tip} - \phi_{sample}$ [Fig. 5.25 (c)], with e the electron charge. Strictly speaking, this expression only holds for the case of metals [261, 291, 303]. For insulating samples, the V_{CPD} does not equal the difference in work functions between the tip and the sample, since the electrically contacted conductors in that case are the tip and the sample-holder, not the sample. Moreover, the voltage applied to nullify the electric field will counteract, in addition to the V_{CPD} , any potential difference that may build-up as a consequence of the bulk insulator in-between the tip and the sample-holder [297].

As a type of Scanning Probe Microscopy (SPM), KPFM senses the interaction, in particular the electrostatic interaction, of the *nm* lateral-size tip with the sample underneath [293]. As we also commented for magnetic force microscopy (MFM) in Chapter 4, the critical point in SPM is to be able to separate the specific interaction we want to measure, in this case electrostatic, from the number of short and long-range forces that are present between the tip and the sample. These interactions include short-range repulsive forces due to the overlapping electron wave functions, Van der Waals attractive forces, adhesion and friction forces...etc. In order to separately measure the electrostatic force with the Kelvin method, the vibrating capacitor method is used [304], first implemented into a Force Microscopy by Nonnenmacher and co-workers [291]: either the tip or the sample are biased by applying an alternating voltage V_{ac} at a frequency ω , along with a continuous voltage V_{dc} . The energy in a parallel plate capacitor is given by $U = \frac{1}{2}C(\Delta V)^2$, where C is the local capacitance between the tip and the sample and ΔV is the potential difference between them. Because of the existence of the CPD, the potential difference is given by: $\Delta V = (V_{dc} - V_{CPD}) + V_{ac}\sin\omega t$. The electrostatic force is the gradient of the energy:

$$F_{el} = -\frac{1}{2}\frac{\partial C}{\partial z}(\Delta V)^2 \quad (5.6)$$

where the z -axis is the direction perpendicular to the sample surface. Substituting the explicit expression of ΔV in Eq. 5.6, developing it, and rearranging the result in terms of the dependency with ω , three different terms arise: $F_{el} = F_{dc} + F_{\omega} + F_{2\omega}$, where

$$F_{dc} = -\frac{1}{2}\frac{\partial C}{\partial z}\left[(V_{dc} - V_{CPD})^2 + \frac{V_{ac}^2}{2}\right] \quad (5.7)$$

$$F_{\omega} = -\frac{\partial C}{\partial z}V_{ac}(V_{dc} - V_{CPD})\sin\omega t \quad (5.8)$$

$$F_{2\omega} = \frac{V_{ac}^2}{4}\frac{\partial C}{\partial z}\cos 2\omega t \quad (5.9)$$

The first term, F_{dc} , contributes to the topography signal by the static deflection of the tip, and the time-dependent F_{ω} and $F_{2\omega}$, can be separately measured by lock-in techniques.

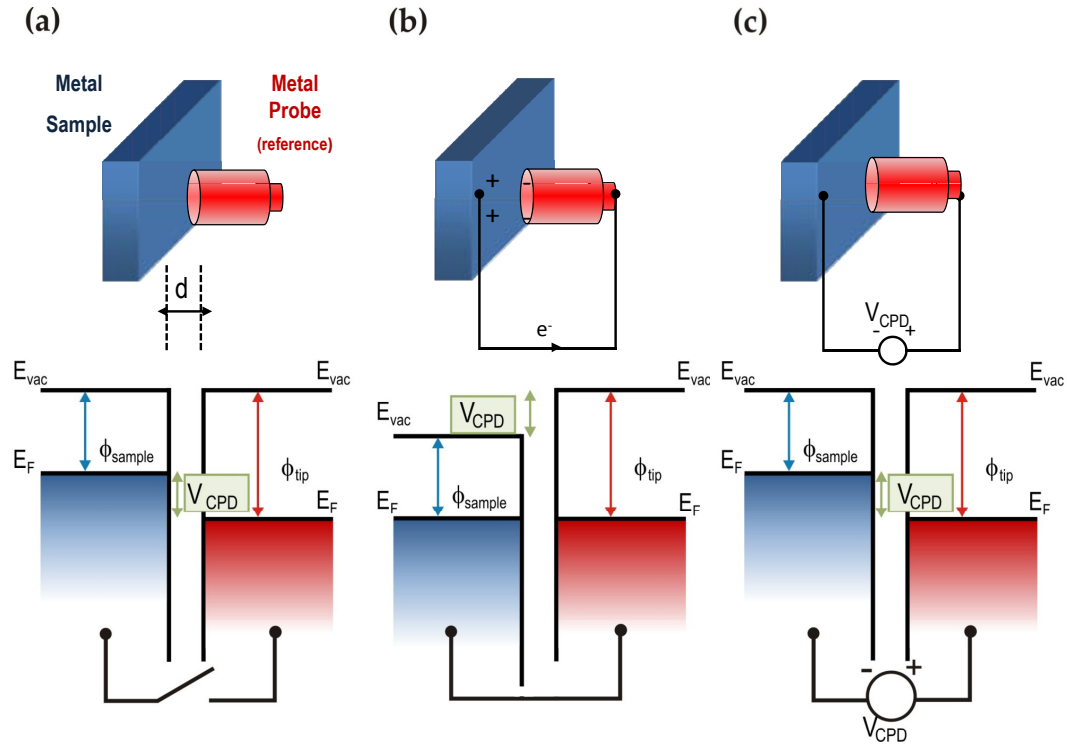


Fig. 5.25: Schematic illustration of the Kelvin method for CPD measurement. (a) Two conductors, sample and probe, are arranged as a parallel plate capacitor separated a distance d . (b) Upon electrical contact, electrons flow from the material with lowest work-function to the material with the highest work-function until the Fermi levels of the two equilibrate, leaving both conductors charged which yields an electrostatic field to develop between them. (c) Such electrostatic force can be nullified by application of the Contact Potential Difference, which equals the difference between the work-function of the two metals.

The term $\frac{\partial C}{\partial z}$ depends on the probe-sample geometry and on the dielectric characteristics of the sample, so it will change with varying sample topography, tip-sample distance, and with the dielectric properties. The term $F_{2\omega}$, which exclusively depends on this derivative (V_{ac} is an externally set constant), can be used for capacitance microscopy [305, 306]. F_{ω} causes the cantilever to vibrate and is the signal used in KPFM measurements: the voltage value V_{dc} we need to apply to make $F_{\omega}=0$ is, precisely, the CPD value between the tip and the sample, $V_{dc}=V_{CPD}$. Therefore, by monitoring the voltages that make $F_{\omega}=0$ at each (x,y) point of the sample, we obtain a CPD map of the scanned area.

Simultaneously to the CPD image, during KPFM operation we obtain the topography image of the studied surface. In fact, one of the uses of KPFM is the imaging of *real* topographical features, free from electrostatic artifacts that may cause errors in the estimation of the lateral and vertical dimensions. To be able to measure topography and KPFM simultaneously we need to disentangle the influence due to Van-der-Waals attractive forces (responsible for topography) and the long-range electrostatic interactions. Generally, the cantilever first resonance frequency (f_0) is used for topography imaging while the alternating voltage V_{ac} is set at a frequency $f_{ac}=\omega/2\pi$ well separated from f_0 : some experiments use small frequencies in the 1-10 kHz range [307–309] while others enhance the resolution of the measurement by tuning ω to the second cantilever resonance frequency ($f_2\sim 6f_0$) [310–312]. In either case we have two feedback loops, one for the height control which gives us the topography signal, the other for detecting and subsequently enforcing $F_{\omega}=0$.

The same concepts related to the *Dynamic mode* operation explained in section 4.1 of Chapter 4 are applied in KPFM measurements. In brief, the interactions between the tip and the sample are measured by detecting the variations in the characteristic parameters of the oscillating cantilever: its amplitude, its phase, and its frequency. The shift in frequency, for instance, is given by: $\Delta f \approx -\frac{f}{2k} \frac{\partial F}{\partial z}$, with k the cantilever spring constant. The Scanning Probe Microscope then works by utilizing these parameters as feedback parameters so that any deviation from the set-point value is followed by a response to restore such set-point. Such response is recorded at every (x,y) point during the scanning of the sample, and hence, we obtain the spatially-resolved image of the desired physical property.

5.2.2 Experimental procedure

The KPFM measurements described here were done in the context of a short three month stay at Prof. M. Salmeron's group at the Materials Science Division of Lawrence Berkeley National Laboratory (LBNL), under the supervision of Dr. A. J. Katan. A UHV AFM instrument (model 350AFM/STM) equipped with a SPM100 control electronics (RHK Technology) was used, operated at room temperature and with a base pressure of around $p\sim 10^{-8}$ Torr. We worked in the Dynamic Non-Contact mode using the resonance frequency of the cantilever as the feedback parameter for topography measurements (Frequency modulated-AFM). An independent demodulator was employed for such purpose (EasyPLL from Nanosurf). For Kelvin operation we used a Lock-in Amplifier (Perkin Elmer) and a PID feedback controller (SIM960, Stanford Research Systems). Fig. 5.26 displays the main parts of the experimental set-up we employed. The sample, a 0.5 mm thick YSZ insulating substrate, was pasted with Ag paint to the grounded sample-holder, and the voltages were applied to the conducting tip.

Frequency modulated operation mode is the usual working mode for topography feedback in UHV, after the pioneering work by Albrecht et al. [313]. In the general Dy -

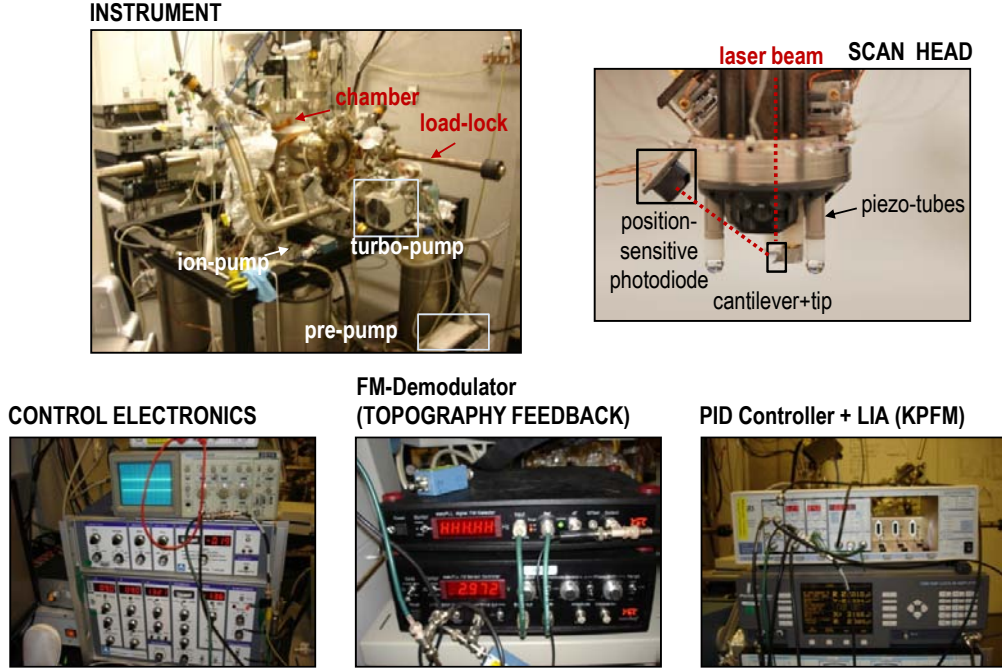


Fig. 5.26: Experimental set-up for simultaneous Frequency modulated-AFM and KPFM measurements using the UHV AFM/STM (RHK Technology) from Prof. Salmeron's group at LBNL.

namic AFM, a cantilever far from the sample surface, which oscillates at its free resonance frequency f_0 , is set to oscillate slightly off-resonance (at its set-point value f). The tip will then approach the sample until it reaches that precise oscillation frequency (set-point). Topography variations of the sample surface will cause the oscillation amplitude to change and the frequency value to deviate from the set-point value f . In the Frequency modulated-AFM mode the feedback loop will then adjust the tip to sample distance in order to restore the set-point frequency f . In other words, the feedback reacts to keep the frequency shift $\Delta f = f - f_0$ value constant and thus topography images are constant frequency-shift images. One could also work in Amplitude-Modulated AFM or 'slope detection' mode, in which the feedback parameter is the amplitude of the oscillation. However, the time necessary for the amplitude to reach, after its change, a steady state (necessary for feedback purpose) is $\tau = 2Q/\omega_0$, where Q is the cantilever quality factor and ω_0 its resonance frequency [222]. Such value results unsuitably large in UHV systems, where Q is $\sim 10^4$ - 10^5 . In Frequency modulated-AFM, by contrast, this problem is avoided because the immediate change in frequencies is detected.

All of the images reproduced in the following were done using Si tips from Budget Sensors with an electrically conducting chromium/platinum coating (5 nm Cr + 25 nm Pt, with Pt the outward layer) [314]. Their resonance frequency is found in the $f_0 \sim 68$ -75 kHz range and the spring constant k is around 2.5-3 N/m. The nominal radius is $R \leq 25$ nm. Typical peak-to-peak oscillation amplitudes, measured through the register of the cantilever thermal spectrum and the oscillation amplitude in the oscilloscope, were in the range of $A_{p-p} \sim 2$ -10 nm.

Fig. 5.28 displays the main channels, significant for the Kelvin Probe signal analysis, that we recorded on a LSMO/YSZ self-assembled nanoisland system. As explained

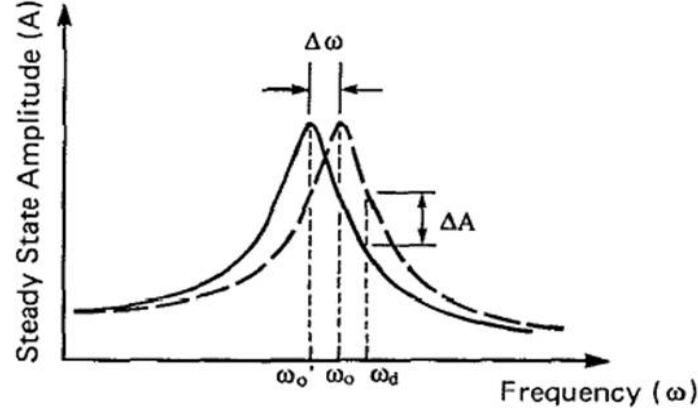


Fig. 5.27: The resonance curve for a cantilever shifts its resonance frequency value from ω_0 to ω'_0 due to the tip-sample interaction ($\Delta\omega \propto \frac{\partial F}{\partial z}$). Such variation causes a variation in the amplitude, ΔA , as measured in the set-point value ω_d . Reproduced from [313].

above, the topography signal registers the piezo changes in order to keep the frequency-shift constant. The frequency shift map to its right, hence, records the error due to the feedback, which is always more evident at the edges of abrupt structures. The CPD channel corresponds to the DC voltage (applied to the tip in our case) necessary to make the F_ω component equal to zero, i.e. this is the CPD or Kelvin signal. We measured the Kelvin signal in the Amplitude Modulated-KPFM mode, which means that we measured and nullified the *amplitude* of the F_ω component. In analogy to the aforementioned Amplitude modulated-AFM and Frequency modulated-AFM, Amplitude modulated-KPFM and Frequency modulated-KPFM use the *amplitude* of F_ω component and its *gradient* for feedback in Kelvin operation, respectively (see for instance reference [293]). To the right of the CPD image we show the Kelvin Error image, which registers the feedback error in nullifying F_ω , and hence will be accentuated where large CPD changes are present. When the Kelvin feedback is OFF, this channels gives the measure of the electrostatic force between the tip and the sample. For every image we recorded both forward and reverse scans to be able to separate true contrasts from scanning artifacts (only the forward scan is shown in Fig. 5.28.) The resolution of the images was typically 256×256 pixels.

Before performing the Kelvin measurement, an important step is the **tuning of the feedback parameters** (Proportional, Integral, and Derivative gains of the PID controller) to make sure that the feedback is working fast enough with respect to the scanning speed. For this reason also the scanning speed was generally kept notably low, at values ~ 0.15 - 0.2 Hz (~ 5 - 6.5 s/line). Fig. 5.29 shows the time-dependent oscilloscope behaviors of the CPD, Kelvin Error, and Topography signals, at the moment of turning the Kelvin feedback on, and off again. The abrupt change of the CPD and of its error signal indicates that the PID parameters are working fast enough (otherwise the change with time would be progressive). The values of the Kelvin error axis, both absolute and relative, depend on the sensitivity of the lock-in at the time of scanning, as well as on its output voltage (2.5 V), and hence are not meaningful. In contrast, although the absolute values in the CPD

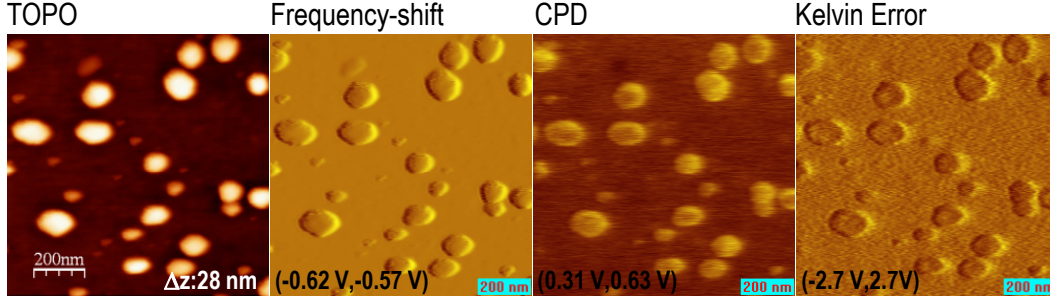


Fig. 5.28: Principal channels to be recorded throughout KPFM measurements. In addition to the simultaneous topography and CPD images, their corresponding error signals are also displayed. The images are $1\ \mu\text{m} \times 1\ \mu\text{m}$.

signal varied notably in both magnitude and sign (sometimes during the course of the same image), the relative island to substrate CPD variations remained roughly constant. These variations in the absolute value of the voltage to be nullified, however, made it necessary to constantly check and re-tune the feedback operation, which at times was difficult. We believe that these variations could arise from trapped charges on our insulating substrate, which may be inhomogeneously distributed at defect sites or kinks of the YSZ surface. The electric field generated by such charges in the tip ‘image’ charges varies with the tip-sample distance, and so does the voltage required to nullify such field [300]**.

The optimal set-points for our measurements of LSMO nanoislands on YSZ substrates ranged from $\Delta f \sim 35\ \text{Hz}$ to $\Delta f \sim 60\ \text{Hz}$, corresponding to typical tip to sample distances ranging from less than 5 nm to slightly above 8 nm, as measured from Force-Distance curves. We routinely adjusted the set-point, so we expect different tip to sample distances for different measurements. Note that none of these PID tuning difficulties arose when we performed preliminary KPFM measurements on LSMO thin conducting films (not shown in this work). The stability of these samples during the KPFM was ideal, the CPD absolute voltages were identical, before and after tip-withdrawal, experiment after experiment etc. This observation supports our ascribing the former voltage variations to trapped charges on the insulating YSZ sample. Regarding the topography signal, it is worth commenting on the $\sim 1\ \text{nm}$ height change produced by the ON-OFF turning of the Kelvin feedback. This is precisely the evidence of an electrostatic force, in this case repulsive, between the tip and the sample, which is present when there is no Kelvin feedback. At the moment the electrostatic force is made zero, with the turning ON of the feedback, the tip increases its distance from the sample (by $\sim 1\ \text{nm}$) so that the Δf is kept constant (otherwise Δf would fall to lower values due to the absence of repulsion).

5.2.3 Origin and evidence of the KPFM contrast in LSMO on YSZ nanostructured samples

The following sections are devoted to the results concerning the KPFM measurements on self-assembled LSMO nanoislands on insulating YSZ substrates, with particular emphasis on the experimental concerns related to their physical interpretation. A small $240\ \text{nm} \times 240\ \text{nm}$

**In their KPFM study of alkali halide surfaces Barth and Henry ascribe the observed potential contrasts, which are typically observed at kink sites of steps of the sample surface, to negative net charges, caused by impurities within the crystal [300].

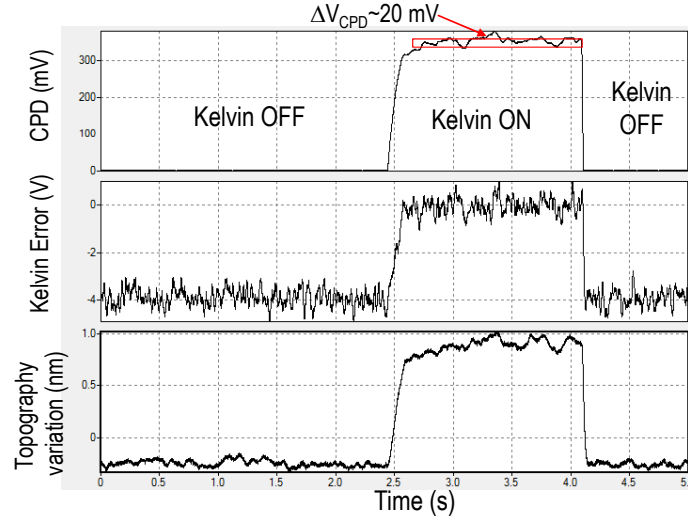


Fig. 5.29: Kelvin feedback testing through the time response signal analysis. Tip and sample are at the set-point distance, and the topography feedback is kept ON, i.e. $\Delta f = \text{constant}$, the whole time. The abrupt changes in time evidence that the PID controller is doing well. The change registered in topography reveals the presence of the electrostatic force.

nm area, containing a single LSMO nanoisland, is imaged in Fig. 5.30. The top row shows the topography-related information of a well-defined LSMO nanoisland with a thickness $t \sim 22$ nm and a lateral size $D \sim 100$ nm. Note that the island displays a rotated-square morphology, one among the two main morphologies observed in LSMO/YSZ nanostructured samples (see Chapter 3). The simultaneous Kelvin measurement of the island is shown at the bottom row of Fig. 5.30. A clear bright contrast, as compared to the dark YSZ substrate, emerges from the island in the potential image V_{dc} . Meanwhile, the Kelvin error signal exhibits very low contrast, featuring the expected changes where abrupt contrast variations occur, i.e. at the edges of the island in this case. A line scan across the V_{dc} image shows that the potential difference between substrate and island is ~ 120 mV. Statistical analysis of a large number of pixels at substrate and island spots give also a very similar potential jump of $\Delta V = 110 \pm 10$ mV. Note that we have named the Kelvin image V_{dc} , instead of CPD , as we did in Fig. 5.28, despite being exactly the same channels, identically measured. V_{dc} is the bare continuous potential applied to the tip in order to make $F_w = 0$. On the other hand, CPD entails a physical meaning, the Contact Potential Difference between the tip and the sample electrode. According to Eqs. 5.7 to 5.9, routinely used to explain the bases of KPFM, V_{dc} equals the CPD . This, however, is not strictly true for our case, as we will explain shortly. In the following, we will refer to V_{dc} images as *potential images*.

We plot a schematic diagram of the system under study in Fig. 5.31. Tip and sample, separated a distance z , are there the capacitor plates. At variance with the canonical KPFM operation example where the sample surface is metallic, in our system the capacitor architecture is formed by the tip and the sample-holder, which is grounded. On top of the sample-holder lays a massive 0.5 mm thick insulator, the YSZ substrate, which supports a dispersion of comparatively tiny LSMO nanoislands on its surface. Hence in the expression for the electrostatic force between the capacitor plates (Eq. 5.6) the capacitance C and the potential V will include the combined effect of the two dielectric media in between: vacuum (or air) and the YSZ substrate. In other words, the voltage we apply in order to

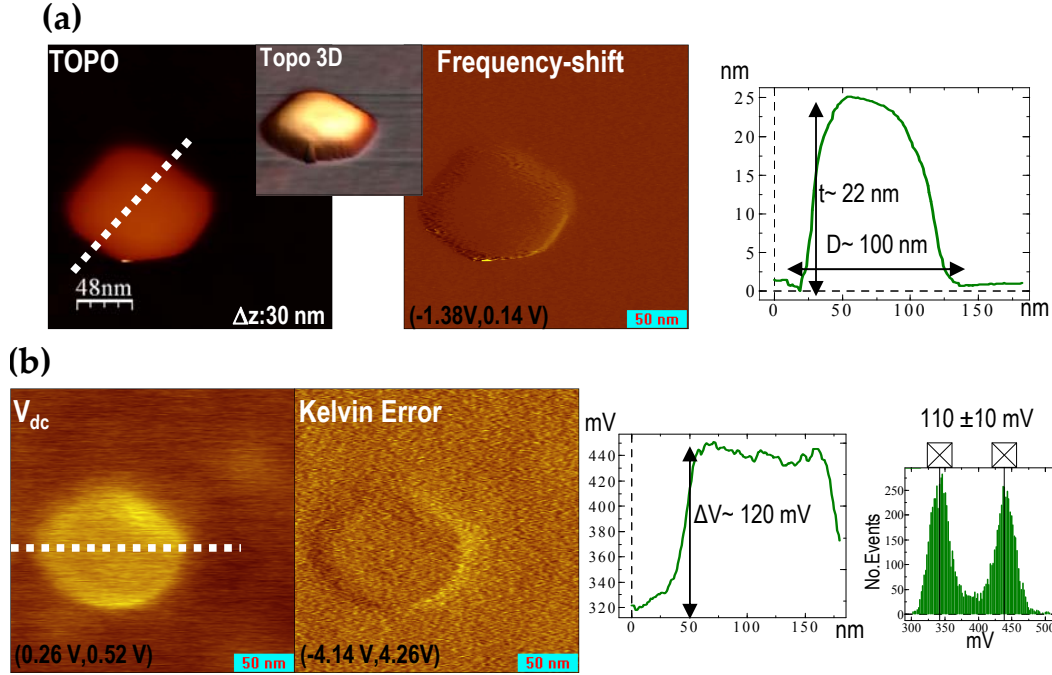


Fig. 5.30: Simultaneous topography (top row, (a)) and KPFM measurements (bottom row, (b)) of an individual LSMO nanoisland on YSZ. The surface potential variation between island and substrate is ~ 110 mV.

make $F_\omega=0$ depends not only on the CPD due to the tip and the sample-holder surfaces but also on the dipoles or charges, that may develop at the LSMO/dielectric, vacuum/YSZ interfaces [297].

If we consider the simplified picture of the parallel plate capacitor and disregard border effects, we may write the potential drop along the two dielectrics in between, vacuum and YSZ, in the following way:

$$\Delta V_{dielect.} = E_1 z + E_2 l \quad (5.10)$$

where E_1 and E_2 are the electric fields in the vacuum (between the tip and the YSZ surface) and within the YSZ, respectively, both of them perpendicular to the vacuum-YSZ interface. z and l are the corresponding dielectric thicknesses (see Fig. 5.31). As there is no free electric charge on the insulator surface, the boundary conditions for the displacement vector at the vacuum-YSZ interface require that $\epsilon_0 \epsilon_r E_2 - \epsilon_0 E_1 = 0$, where ϵ_r is the relative permittivity of YSZ (which takes values around ~ 25 [315] and ~ 29 [316]). If we now insert a conductor of thickness t in between the two plates at a distance $(z-t)$ from the tip, the voltage difference will vary accordingly:

$$\Delta V_{dielect.'} = E'_1 (z-t) + E'_2 l \quad (5.11)$$

where now E'_1 and E'_2 are defined by the condition of no electric field within the conductor, i.e. $E'_1 = \frac{-\sigma}{\epsilon_0}$ and $E'_2 = \frac{\sigma'}{\epsilon_0 \epsilon_r}$ for the fields in vacuum and within the YSZ, respectively. σ and σ' refer to the free surface charge density on the top and bottom plates of the conductor, respectively. Adding the potential drops in Eq. 5.10 and 5.11 to the expression $\Delta V = (V_{dc} - V_{CPD}) + V_{ac} \sin \omega t$, and substituting the new potential difference in the expression for the electrostatic force (Eq. 5.6), we may derive the expressions for the ω component of the

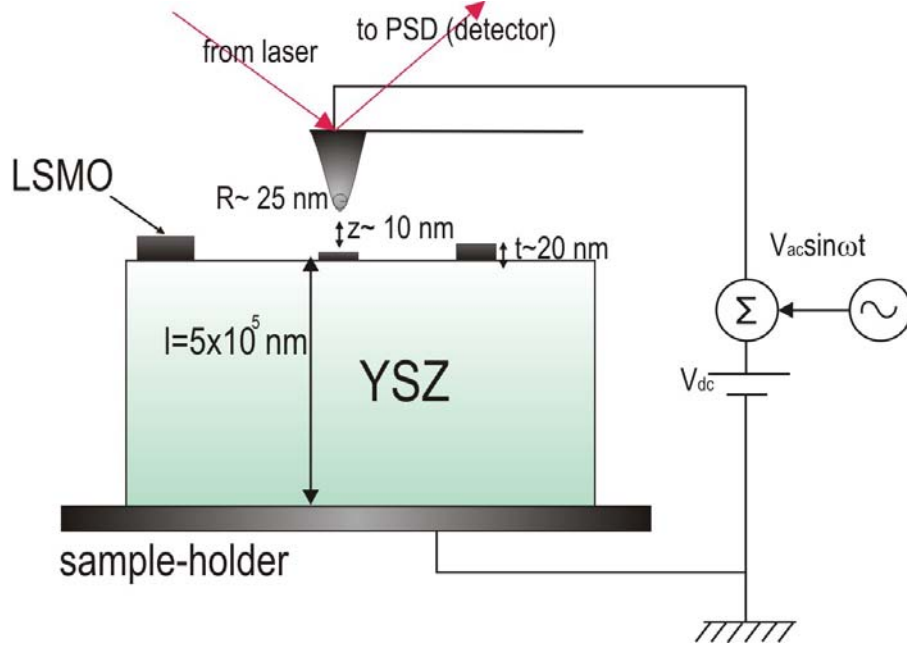


Fig. 5.31: Schematic diagram of the experimental set-up for the KPFM measurement of LSMO on YSZ nanostructured system.

force, F_ω , both for the tip positioned on top of the bare YSZ substrate and on top of the LSMO nanoisland:

$$F_\omega^{YSZ} = -\frac{\partial C}{\partial z} V_{ac} \left[V_{dc} - V_{CPD} - E_1 z - \frac{E_1 l}{\epsilon_r} \right] \sin \omega t \quad (5.12)$$

$$F_\omega^{LSMO} = -\frac{\partial C'}{\partial z} V_{ac} \left[V_{dc} - V_{CPD} + \frac{\sigma(z-t)}{\epsilon_0} - \frac{\sigma' l}{\epsilon_0 \epsilon_r} \right] \sin \omega t \quad (5.13)$$

where C and C' correspond to the capacitances of each of the two architectures (dielectric and dielectric+ conductor). The voltages required to make that component equal to zero over the YSZ substrate or the LSMO island will hence be:

$$V_{dc}^{YSZ} = V_{CPD} + E_1 \left(z + \frac{l}{\epsilon_r} \right) \quad (5.14)$$

$$V_{dc}^{LSMO} = V_{CPD} - \sigma \frac{z-t}{\epsilon_0} + \frac{\sigma' l}{\epsilon_0 \epsilon_r} \quad (5.15)$$

And the difference between the two leads to

$$\Delta V_{dc}^{LSMO-YSZ} = -\sigma \frac{z-t}{\epsilon_0} + \frac{\sigma' l}{\epsilon_0 \epsilon_r} - E_1 \left(z + \frac{l}{\epsilon_r} \right) \quad (5.16)$$

Note that the V_{CPD} voltage term due to difference in work function between the tip and the sample-holder is canceled, i.e. we do not have a dependence with respect to the sample-holder. In contrast, we obtain an expression which is dependent upon the distinct charge distributions at the LSMO surfaces. Note that this picture is a rude oversimplification of the real experimental set-up, as we have considered that the LSMO conductor in-between the two dielectrics consists of two infinite parallel plates. In reality, the LSMO nanoislands are finite solids, with well-defined crystal planes that connect the upper and lower parallel surfaces. Instead of charge distributions, in a faceted finite size metal in equilibrium

such as these nanoislands it is generally talked of the *surface dipole* of a specific surface, which is the origin of its work function and thus it is directly related to the geometric and, in consequence, the electronic structure of that specific surface [317, 318]. This issue will be discussed later in the chapter. The above oversimplified view, however, is useful to illustrate the role of the bulk insulator, while it highlights that the relative potential differences between the substrate and the LSMO islands do not depend on the sample-holder electrode.

In addition to a remarkable contrast difference between the LSMO nanoislands and the YSZ surface of Fig. 5.30, careful measurements of some islands, which generally imply very low scanning speeds ($\sim 5\text{--}6.5$ s/line), enable the observation of contrast variations within one island. The potential images of Fig. 5.32, for instance, evidence a brighter contrast at the lower half of the island. This potential variation is quantitatively shown in the line-scans of Fig. 5.32 (c): we have plotted the nanoisland topography (top row) and potential (bottom row) profiles, corresponding to the white dashed lines in the images. A potential jump of around ~ 80 mV is measured within the island, in agreement with the statistical V_{dc} distribution study of the regions marked in blue squares and numbered 1, 2, and 3. After verifying that the Kelvin feedback is working correctly, a number of tests are available to assess whether this is a physical effect or an artifact: we can repeatedly scan the island, combining different directions, e.g. back and forth downwards [Fig. 5.32 (b), top row] or upwards, changing the angle of the tip with respect to the sample [from 0° in Fig. 5.32 (b) top to 90° in Fig. 5.32 (b) bottom row. . .etc. Other tests include slight variations of the tip to sample distance, or playing with the scanning speed. After taking such precautions we can thus conclude that there is a real difference in the potential between those two island halves. According to what we saw earlier this could be linked to a difference in the charge distribution within the upper facet. In turn, such charge inhomogeneities could have multiple origins: different surface reconstructions of the facet yielding distinct charge distributions or the presence of defects on the surface promoting the adsorption of contaminants, are only some of the possible scenarios.

Fig. 5.33 shows the KPFM measurement of three different LSMO nanoislands from the same sample as above. The top panel displays the topographical information of the nanostructures, i.e. the topography and its corresponding error image, plus a line scan along the dotted white line drawn in the topography image. The line profile displays a $t \sim 20$ nm thick island next to a small $t \sim 10$ nm island. The simultaneous potential and its error measurements are shown in the lower panel [Fig. 5.33 (b)]. The two largest islands are now characterized by a bright halo at their edges, surrounding a darker contrast in the middle; the latter is still ~ 60 mV above the substrate contrast [see the line profile in Fig. 5.33 (b')]. The potential we measure at the edges is around ~ 60 mV above the value at the center of the island (i.e. 120 mV above the substrate surface). If we perform a statistical analysis of the potential difference between the substrate and the whole island (including both edges and center), we obtain the distribution plotted in Fig. 5.33 (b''), where two clear peaks are separated ~ 100 mV; this is roughly the value expected from averaging the potential values of the island edge and center. All these observations point at possible differences in the electrical nature of the lateral and top facets of some of the islands. The fact that the bright halo at the island edges does not appear always (we do not see it, for instance, in the island of Fig. 5.32, although it has a similar thickness) suggests that it is not a measurement artifact. Indeed, the small nanoisland of Fig. 5.33 does not exhibit the *edge feature*. Instead, it shows a homogeneous ~ 60 mV potential difference with respect to

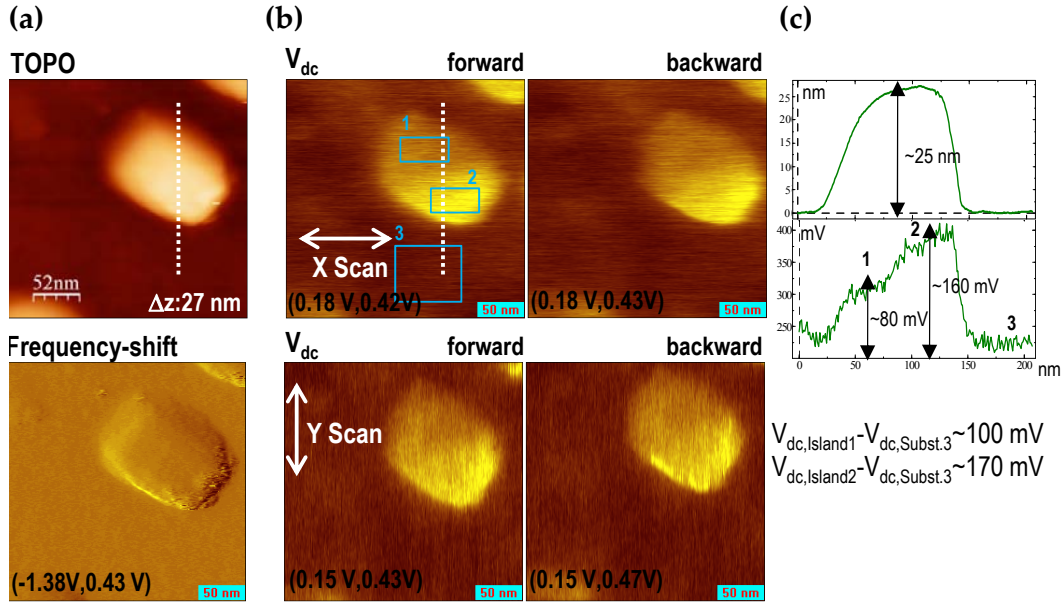


Fig. 5.32: 260nm×260nm images of a LSMO nanoisland on YSZ. (a) Topography and frequency-shift images. (b) Potential images acquired with the tip scanning in the X (0°, usual way) and Y (90°) directions. (c) Line profiles of the topography and V_{dc} images, corresponding to the white dotted lines across the island. The values below are the potential differences of the two distinct halves of the island with respect to the substrate, calculated from statistic evaluation of the squares numbered 1, 2, and 3 in the V_{dc} image.

the YSZ substrate. In the V_{dc} image it appears that the tip, with a radius of around $R \sim 25 \text{ nm}$ rapidly widening away from the apex, cannot fully resolve the small lateral separation between the large and the small island. A hypothetical effect of the lateral edges is thus not discernible. The small height of the island, however, implies very small lateral facets which suggest that the contrast we observe is mainly caused by the planar top facet. Note that this island, half the thickness of the previous discussed, exhibits the same $\sim 60 \text{ mV}$ potential difference, which can be taken as a further indication that the signal we measure does not come from the topography.

As a matter of fact, the ‘leakage’ of topographical information into the potential channel is a major issue of concern, since it can lead to physical interpretation of measurement artifacts. It is especially challenging to disentangle the topography influence from purely electrostatic signals in cases like the present one, where the abrupt changes in the topography are accompanied by a change of material. The problem of the tip-sample convolution, common to all scanning force microscopies and already mentioned for MFM in Chapter 4, is indeed also present in KPFM. For the case of the electrostatic interaction, not only the tip apex contributes to the contrast observed at a certain (x, y) position, but other parts of the tip, further separated from the sample surface, will also contribute, since the electrostatic force is long ranged and the whole tip is conducting. Consequently, the contrast exhibited by a particular (x, y) spot will display a certain proportion of contrast belonging to other spots in the sample, which is one of the reasons why achieving lateral resolution in KPFM is harder than in topography measures, and why long tips with small opening angles are ideally required. In addition to lowering the resolution of the potential image, it was demonstrated that the convolution due to the tip-sample geometry may result in a

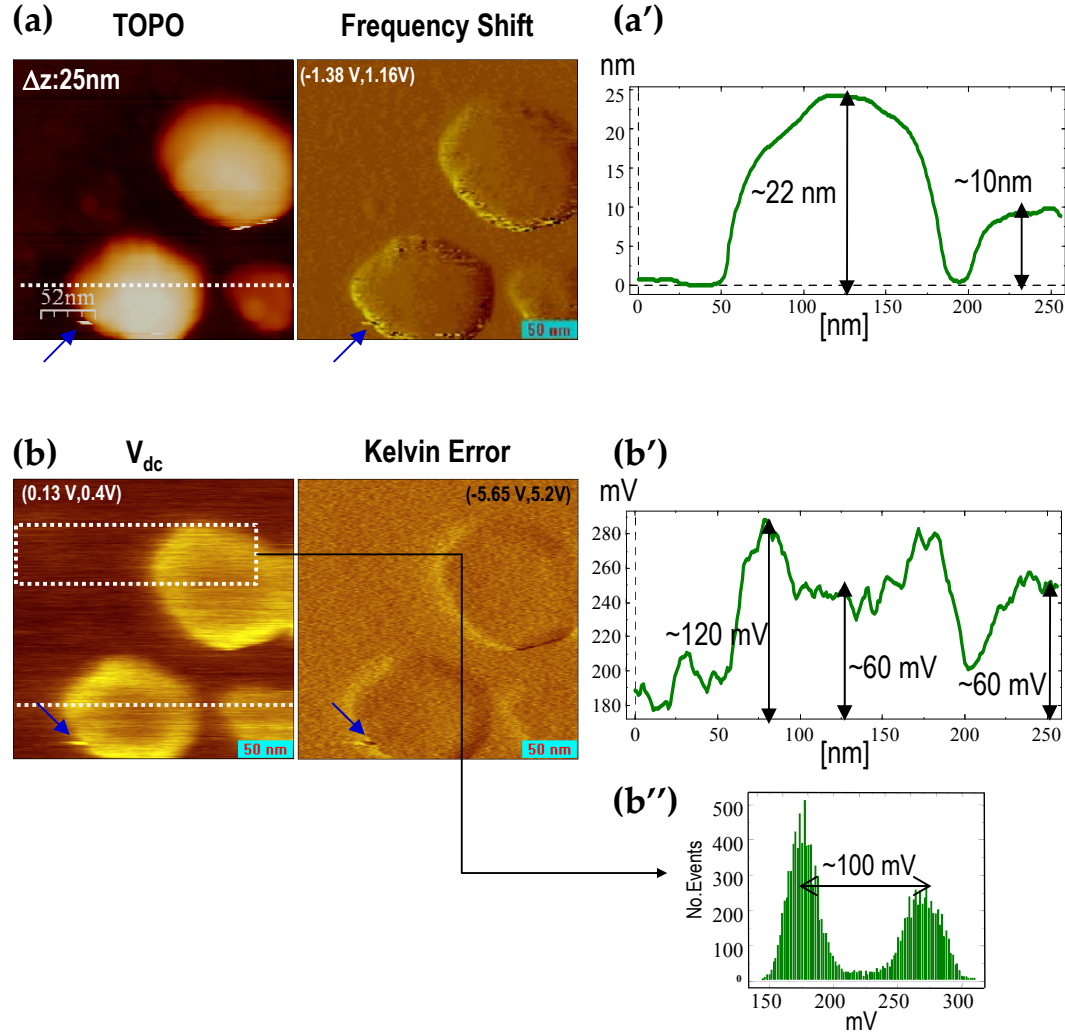


Fig. 5.33: $260 \text{ nm} \times 260 \text{ nm}$ images of LSMO nanoislands on YSZ. (a) Topography and frequency-shift images. (a') Line scan corresponding to the dotted white line in the topography image (a). (b) Potential and Kelvin error images. (b') Potential profile along the line marked in the V_{dc} image in (b), revealing a higher potential at the island edges with respect to the center. No such feature is observed in the contrast belonging to the lowest ($t \sim 10 \text{ nm}$) island, which exhibits a potential difference of $\sim 60 \text{ mV}$, analogously to the large island center. (b'') Potential distributions of the island and substrate regions within the dotted square area marked in (b). The mean difference between substrate and island (edges and center) is around $\sim 100 \text{ mV}$.

certain cross-talk of the potential signal with the topography signal; this was named the ‘topography artifact’ by Morita and co-workers [319]. Such effects are mainly observed in the case of granular films with grain sizes of the order of or smaller than the radius of the tip [320]. In the case of our nanoislands ($D \sim 100\text{--}250\text{ nm}$), although we cannot fully rule out a partial contribution from the topography, it will emerge clearly from the analysis throughout this chapter that this is a secondary effect compared to the main signal. In line with this issue, Fig. 5.34 shows the topography and potential images of a LSMO nanoisland on top of a CeO_2 buffer layer. The topography image shows an ill-defined amount of material protruding from the darker substrate. By comparison with other islands in this sample (not shown) we are able to distinguish the squared shape of an island as the brightest contrast in topography, at the far edge of the protruding material (precisely on the position that says c). The material to the left of the island, in the spot b, is probably dirt attached to the island. The important fact here is that, although such unidentified material protrudes from the sample at least 30 nm, the potential contrast it shows is darker than that of both the real island contrast (the brighter spot, c) and of the substrate background. In brief, a protruding object does not necessarily lead to a bright contrast, which confirms that in the potential image we are not measuring topography but electrostatic interaction.

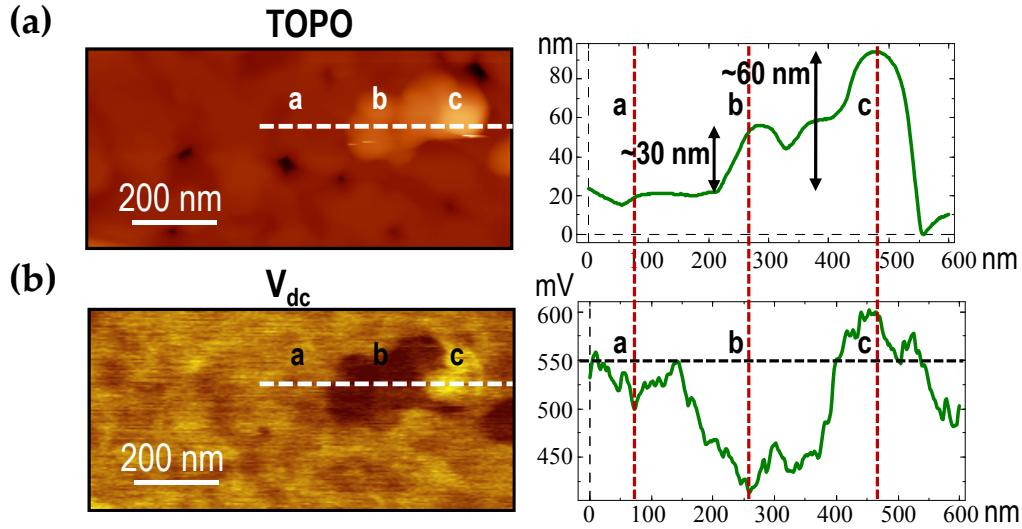


Fig. 5.34: Topography (a) and potential (b) analysis of a LSMO nanoisland on a CeO_2 buffer layer. The line profiles at the right hand side correspond to the dashed white lines drawn in the images. a, b and c along the profile indicate positions on the buffer layer and on the protruding material.

It is also pertinent at this point to mention the presence of topography-related artifacts in the potential images which result from feedback failures. The failure of the topography feedback will give erroneous normal force (F_N) values, which are the values that feed both the topography and the Kelvin feedback. This will thus be reflected in the ω component of the force F_ω , responsible for the Kelvin feedback. Such feedback failures are of course more likely to occur at sudden height changes, as those taking place at the island-substrate boundaries. An example is evidenced with blue arrows in the images of Fig. 5.33. That kind of feature indicates a feedback failure, and one can find its fingerprint not only in the topography channels, but also in the potential images. Moreover, we may also note that it produces a bright yellow contrast in the V_{dc} channel, which actually enhances the bright appearance of the island edges. Still, we may look at other places of the same island

edges where the substrate to island transition (most easily observed in the frequency-shift channel) is smooth, and is still accompanied by bright contrast in the V_{dc} image. Consequently, although present, the feedback failures do not account for the great majority of the measured potential variations.

5.2.4 Analysis of the facet contrast in large LSMO nanoislands

The contrast variations between the insulating YSZ substrate and the LSMO nanoislands illustrated in the previous examples appear notably enhanced when looking at substantially larger LSMO islands, with thickness t that go up to 80 nm and lateral sizes D of around 200 nm. Fig. 5.35 exhibits the topography and potential images of three LSMO nanoislands of this type. The potential image in Fig. 5.35 (b) features a clear bright-dark double contrast within each island. We can also note that the dark contrast of the substrate surface is not uniform, but exhibits a certain ‘color roughness’, as if it were mixed with some kind of bright contribution. In fact, topography images of the substrate surface as the one shown in gray shades in the inset of Fig. 5.35 (a), give evidence of small islands on the YSZ substrate surface. These are very likely related to the presence of La and Mn on the YSZ surface, as we already pointed out in our discussion of the PEEM results (section 5.1.3). Consequently, comparison with samples characterized by a clean YSZ surface (e.g. the case discussed in the previous section) must be done with some caution.

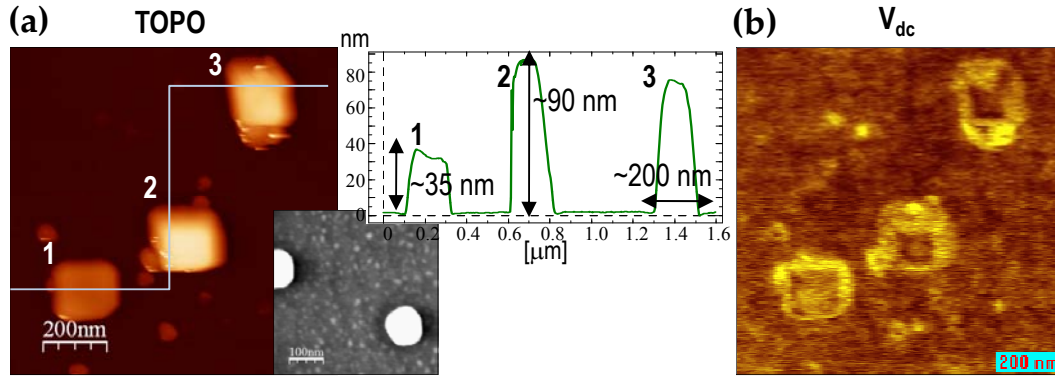


Fig. 5.35: $1\mu\text{m}\times 1\mu\text{m}$ topography (a) and potential (b) images of ‘large’ LSMO nanoislands on YSZ. The topography profile of the three islands, along the light-blue line in (a), shows the typical island sizes. The inset in gray shades, with saturated intensities, evidences the presence of material on the substrate surface in the form of little islands.

A closer look at the nanostructures of Fig. 5.35 reveals the details of the contrast variation within them. Fig. 5.36 shows the topography and potential images of the island numbered 2 in Fig. 5.35 (a). This is a *regular-square* type of LSMO nanoisland (see Chapter 3) that exhibits $(001)_{\text{LSMO}}$ top and lateral $(111)_{\text{LSMO}}$ facets. The potential image in Fig. 5.36 (b) shows that these two inequivalent planes yield different potential values with respect to the bottom reference line: ~ 50 mV for $(111)_{\text{LSMO}}$ and ~ 10 mV for the $(001)_{\text{LSMO}}$. Statistical analyses of a large number of pixels within substrate, the top $(001)_{\text{LSMO}}$ facets, and the lateral $(111)_{\text{LSMO}}$ facets, give $V_{dc}^{\text{subst.}} \sim -9 \pm 10$ mV, $V_{dc}^{\text{top}} \sim -11 \pm 10$ mV, and $V_{dc}^{\text{lat.}} \sim -35 \pm 10$ mV, respectively. The voltage distributions for each are plotted in 5.36 (b’). From these values we can deduce that the substrate and the island top facets yield similar potential values

(within the error bars), while the potential necessary to nullify the F_{el} on the $(111)_{\text{LSMO}}$ facets is $\sim 45\text{-}50$ mV larger.

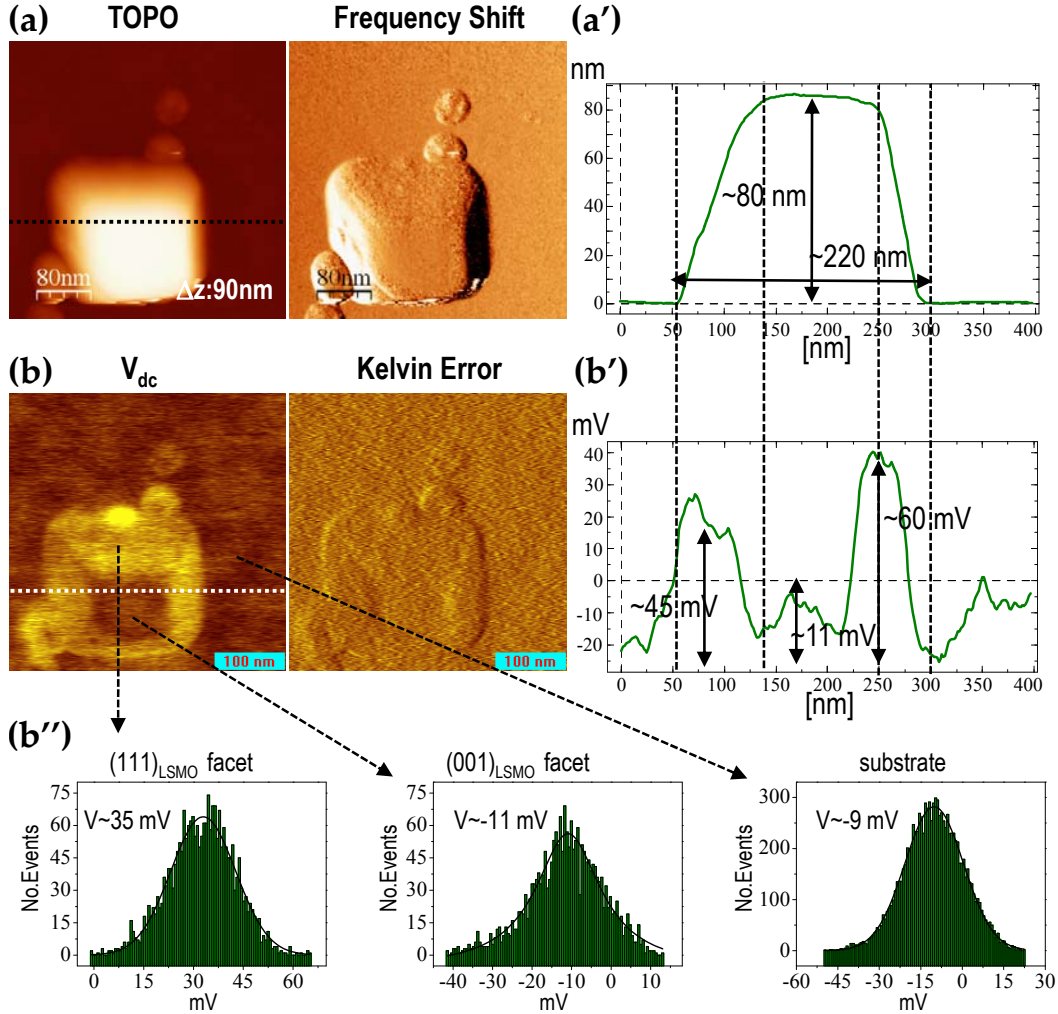


Fig. 5.36: $400\text{nm} \times 400\text{nm}$ topography (a) and potential (b) images corresponding to the ‘large’ nanoisland named 2 in Fig. 5.35. The dark to bright contrast variation, in the order of ~ 40 mV, appears linked to the nature of the LSMO facet. The line scans in (a') and (b') are simultaneous topography and potential profiles, i.e. they correspond to the same spatial region, marked in dotted lines on the topography and V_{dc} images (a) and (b). The graphs in (b'') belong to the statistical potential distributions on the $(111)_{\text{LSMO}}$ facet, the $(001)_{\text{LSMO}}$ facet, and on the substrate.

Fig. 5.37 shows the measurements of the island numbered 1 in Fig. 5.35. It is one of the *low* islands found in the present sample, with thickness $t \sim 35$ nm and a lateral size $D \sim 225$ nm. As in the island from Fig. 5.36, the top $(001)_{\text{LSMO}}$ and the lateral $(111)_{\text{LSMO}}$ facets yield different potential values. These contrast variations are quantitatively analyzed in the line-scan below the image, and also by comparing statistical analysis of the potential distributions within the regions with the same contrast; the resulting absolute values along with their standard deviation are shown in the potential images. Note, for instance, that the potential value of the $(111)_{\text{LSMO}}$ facet is $V_{dc}^{\text{lat.}} \sim 35 \pm 10$ mV, i.e. ~ 45 mV ($V_{dc}^{\text{subst.}} \sim -10 \pm 10$ mV) with respect to the substrate potential. This is in excellent agreement with the contrast

variation observed in the island of Fig. 5.36, even if these two structures are remarkably different: $t \sim 80$ nm vs. $t \sim 35$ nm, which means that the $(111)_{\text{LSMO}}$ facets have very different extension. These observations are in line with the assumption that the topography signal is not responsible for the observed contrast variations.

In addition to the orientation-dependent facet potential, we can also distinguish different types of contrasts within the top $(001)_{\text{LSMO}}$ facet: the upper part shows a slightly darker contrast as compared to the lower part. Such contrast variation is identically observed in the backward scan (not shown) and in the $170 \text{ nm} \times 170 \text{ nm}$ potential image shown in Fig. 5.37 (b'). The latter scan was measured ~ 1 h after the scan of Fig. 5.37 (b) and entirely reproduces the contrast variations there observed. In fact, by restricting the scan to the island center (plus a bit of the lateral facets) we avoid the abrupt transition of the tip from the substrate surface to the nanoisland. Consequently, the measurement is free of topography feedback failures, and, being identical to that of Fig. 5.37 (b), further supports our claim that the observed potential variations, exemplified in the previous images, have a real physical origin.

Although its thickness is not far from the values displayed by the islands of the previous sample [e.g. $t \sim 22$ nm in Fig. 5.33], the island of Fig. 5.37 features a notably larger lateral size. Such a difference in lateral size could explain why here the lateral facets can be clearly discerned from the top flat facet, while in the case of Fig. 5.33, the tip-nanoisland convolution precludes resolving these features. It is well likely, in fact, that a facet-dependent contact potential occurs in both samples, even if it's not well-resolved in Fig. 5.33 due to the smaller island sizes of that sample. We should note, nevertheless, that the lateral facets of the *rotated-square* morphology islands are not $(111)_{\text{LSMO}}$ planes as in the present case (see Chapter 3). Therefore, such difference in the crystal nature of the facets, along with the fact that our reference substrate is also different in both samples (recall the presence of small islands in the second sample), should be noted before attempting to compare the magnitude of both contrast variations.

The facet-dependent contrast discussed above raises the natural question of what contrast yield the triangular LSMO nanostructures, which top facet and long lateral facets belong to the $\{111\}_{\text{LSMO}}$ family of planes. Fig. 5.38 shows the simultaneous measurement of two interpenetrating square islands and a triangular LSMO nanostructure. The potential image of Fig. 5.38 (b) shows the average potential values inferred from the statistical analysis of the potential distributions within each blue square. Note that this latter measurement was performed on a different day, and that these values are at first sight very different from those of Figs. 5.36 and 5.37. However, the absolute numbers are not meaningful, as we have emphasized earlier in this KPFM section. Only the *differences* are important. We observe that, indeed, the tendency of 'dark top facet' and 'bright lateral facets' is reproduced for the square islands. In particular, the mean potential value of the top facets of the two merged square islands is $V_{dc}^{top} \sim -35 \pm 20$ mV [note that this is an average value, since there is a graduation of contrast from the upper (darker) to the bottom (brighter) part of the facets]. Taking this value as a rough estimate, the difference with respect to the brighter lateral $(111)_{\text{LSMO}}$ facets ($V_{dc}^{lat} \sim -85$ mV, see the line scan) is of ~ 50 mV, which is in good agreement with the variations between lateral $(111)_{\text{LSMO}}$ and top $(001)_{\text{LSMO}}$ facets measured in the square islands from the previous examples.

Moving now to the triangle, the contrast of the top facet appears fairly bright and uniform, and we do not see the clear change in contrast between the lateral and the top facets characteristic of square islands. Both the line scan and the statistical analysis show values

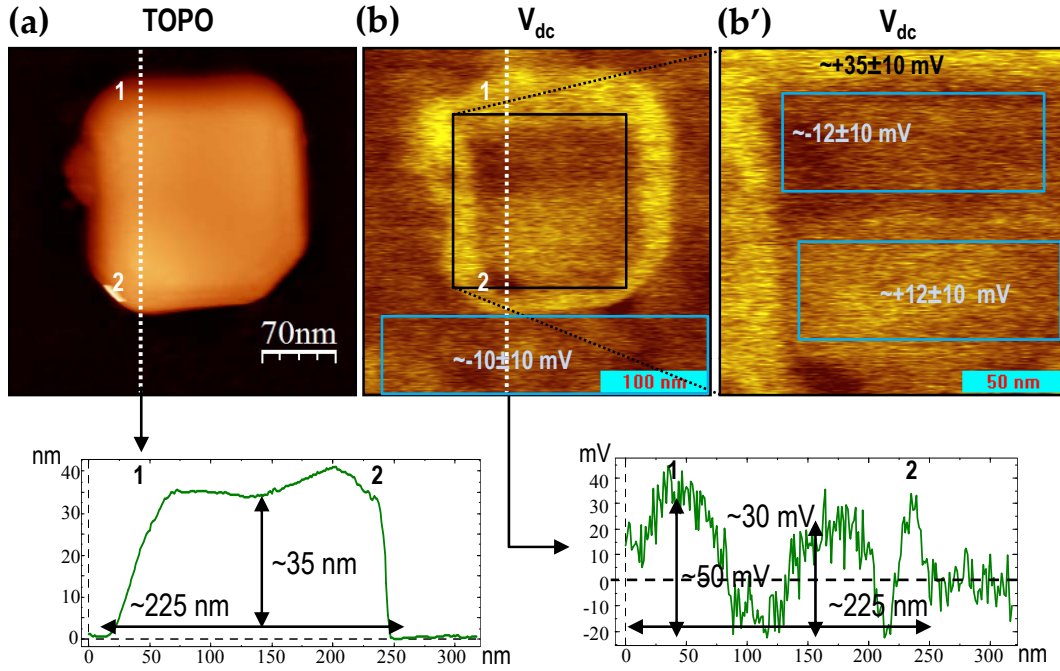


Fig. 5.37: (a)&(b) $320\text{nm} \times 320\text{nm}$ topography and potential images corresponding to the nanoisland numbered 1 in Fig. 5.35. The line scans along the vertical dotted-lines in both images are plotted below. (b') A new scan ($170\text{nm} \times 170\text{nm}$, potential image) shows the interior of the nanoisland potential distribution. The numbers given in (b) and (b') represent the potential values at each distinct region of the nanoisland.

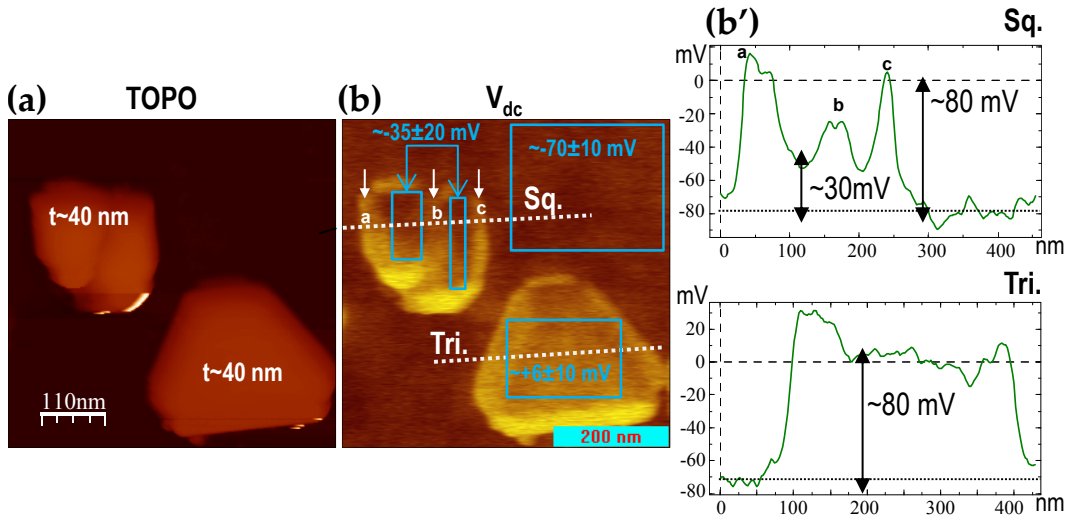


Fig. 5.38: $570\text{nm} \times 570\text{nm}$ topography (a), and potential (b) images of two merged square islands and a triangular (111) out-of-plane oriented island. The mean potential values of the distinct regions, marked in blue squares, are also indicated. (b') Potential line scans of the square and triangular islands across the dotted white lines in (b).

for the triangle $(111)_{\text{LSMO}}$ top facet that differ by ~ 80 mV with respect to the substrate surface. This value is much larger than that of the $(001)_{\text{LSMO}}$ top facet of the square islands, both in the present image and in the previous examples. Conversely, it is in remarkable agreement with the value we obtain for the $(111)_{\text{LSMO}}$ lateral facets of the square islands in Fig. 5.38, which is around ~ 85 mV. Fig. 5.39 displays the topography line scans corresponding to the triangle and square islands in Fig. 5.38 [Fig. 5.39 (a) and (b), respectively] and the profile of the square island of Fig. 5.37. Note that the angle of the facets inferred from the line scans (α_{exp}) is the result of the tip-radius/nanoisland-facet convolution: the angle of $\sim 71^\circ$ between the $\{111\}_{\text{LSMO}}$ facets of the triangle is reduced to around $\sim 56^\circ$, while the $(111)_{\text{LSMO}}$ lateral facets in the (b) and (c) square islands, at a theoretical angle of $\sim 54.7^\circ$ from the substrate horizontal, differ from one another. We have already commented that the experimentally measured angles with this kind of tips and measurements does not provide for the real values. Nevertheless, the fact that the three islands in Fig. 5.39 exhibit very similar heights, lateral sizes, and experimental angles, supports the fact that the brighter contrast obtained for the triangular top-facet is due to its crystallographic nature. In other words, would the effect be topographical, we would expect, since the geometry of the islands and the resolved experimental angle are very similar, that the triangular island exhibited a depressed potential value in its central region, as in the case of the square islands. Instead, such central value, corresponding to the $(111)_{\text{LSMO}}$ facet, remains higher, by around ~ 50 mV, with respect to the potential exhibited by the $(001)_{\text{LSMO}}$ facets.

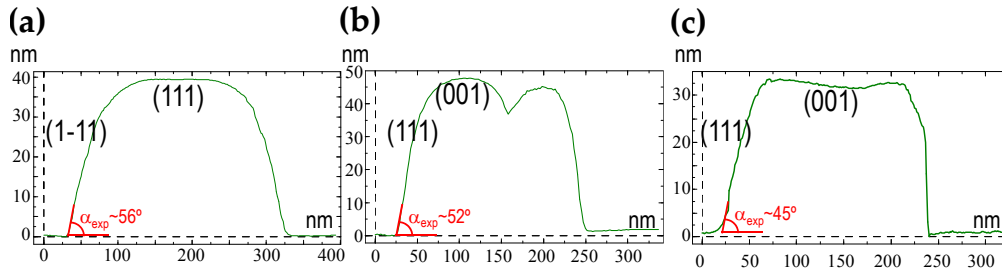


Fig. 5.39: Topography line-scans comparing the geometrical features of: (a) the triangular island in Fig. 5.38, (b) the square islands in Fig. 5.38, and (c) the square island of Fig. 5.37. The lateral and top facets are labeled, as well as the experimentally measured facet angle.

5.2.5 On the origin of the facet contrast: work function anisotropy

The results discussed until now reveal that there is a difference in potential of ~ 50 mV between the $(111)_{\text{LSMO}}$ and the $(001)_{\text{LSMO}}$ crystal planes. We will see next that such potential difference can be related to the so-called *work function anisotropy*, i.e. the dependence of the work function W of metal single crystals on the crystallographic orientation of the surface.

The work function W of a finite-size metal is defined as the energy necessary to remove an electron from its Fermi energy level E_F to a point in the vacuum just outside the solid. By the term ‘just outside’ we refer to a distance far larger than the interatomic distances but small with respect to the sample size [321]. The vacuum level *just outside* a solid $V_{\text{vac}}(s)$, depends on the chemical, atomic, and electronic structure of its surface layers through the so-called *electronic surface dipole* of the specific surface. Conversely, the vacuum level at infinity $V_{\text{vac}}(\infty)$ is invariant, and describes the energy of an electron at rest at infinite distance

from the solid [322]. This $V_{vac}(\infty)$ is not experimentally accessible [322, 323] and thus it is not relevant in real measurements, and in the following we shall therefore exclusively refer to $V_{vac}(s)$. The energy difference between these two levels is caused precisely by the presence of the surface dipole layer^{††}, which, in general, causes the vacuum level of the solid to raise from that at infinity.

The surface dipole has its origin on the spreading of the electronic charge density towards the vacuum, which occurs at the surface of a solid [324] [see Fig. 5.40 (a)]. In a nearly-free electron metal (which is not the case of LSMO), this is typically explained through the simple jellium model. Within the bulk of the crystal there is no dipole since the constant background positive charge, modeling the ion cores, is neutralized by an equal and opposite electronic charge. At the surface, however, due to their quantum-mechanical nature, electrons prefer to penetrate slightly into the vacuum region to lower their kinetic energy. A surface dipole thus forms. This ‘spilling out’ of the electron cloud causes a negative pole to stick out of the surface, inducing a potential step or dipole barrier V_e [see Fig. 5.40 (b)] [317]. In order to escape from the metal, the electron must overcome such barrier. For the electrons in the last occupied energy level, E_F , the barrier they must surmount is precisely the work function of the metal $W = V_e - E_F$. Notice that in Fig. 5.40 (b) we have written explicitly $V_{vac}(s)$ in relation to the electrostatic potential just outside the solid. According to what we said above, for distances far away from the solid such level will converge into the $V_{vac}(\infty)$ [323]. The reference energy in the diagram is $\langle V \rangle$, the average electrostatic potential within the bulk of the metal [325], i.e. $V_e = V_{vac}(s) - \langle V \rangle$.

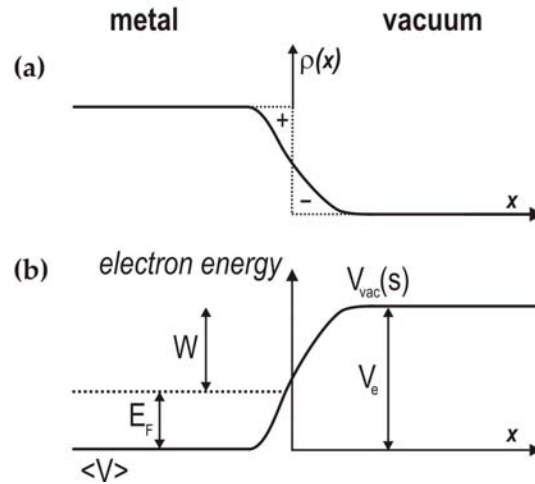


Fig. 5.40: (a) Electronic density distribution at the surface of a metal. The spreading of the electron cloud gives rise to the surface dipole. The ‘thickness’ of the dipole layer is in the order of some angstroms [324, 326]. (b) Energy levels at the metal/vacuum interface. The work function of the metal, W , is directly related to its surface dipole ($W = V_e - E_F$).

Nevertheless, this simple model is not sufficient to explain the work function anisotropy: a jellium surface is a flat and structureless plane. An elegant solution to this problem was given in 1941 by Smoluchowski [327]. The idea is quite intuitive: one just needs to consider, instead of a flat jellium surface, a *corrugated* one. The conduction electrons will slightly penetrate in the vacuum, as before, giving rise to the surface dipole. In addition to this surface

^{††} And, in insulating materials, also by extra charges on the sample surface [322].

dipole, which sticks out of the surface normal to the surface and increases W , however, electrons will also redistribute laterally (a corrugated electron cloud costs energy, i.e. better to ‘smooth it out’). This means that some negative electron charge will ‘drip inwards’, leaving the positively charged ions of the jellium surface ‘uncovered’. In other words, the so-called Smoluchowski smoothening [325] causes a *reverse dipole* which tends to lower the work function. The more corrugated the surface (i.e. less close-packed), the lower the work function, as a result of this effect. Therefore, for SC, BCC, and FCC Bravais lattices it is expected that the work functions W of (100), (110), and (111) facets, respectively, to be the largest. These predictions were theoretically [324] and experimentally [328] confirmed^{‡‡}.

In the case of KPFM on LSMO nanoislands, work function variations from one crystal facet to another should be probed, provided that the tip to sample distance z is short compared to the lateral size of the facet, but large enough that the image potential effects are negligible there. Under such conditions we can detect the corrugation of the electrostatic potential related to the work function anisotropy discussed above. We talk in this case of local work function measurements (see references [325, 326] for in-depth treatments of this issue). In contrast, when the probe is drawn far from the sample (or, analogously, the sample is very small with respect to tip-sample distance) the local potential becomes isotropic, i.e. at sufficient distance from the metal the sample has only one well-defined work function [318, 323, 326]. Fig. 5.41 shows a sketch drawn at scale of the KPFM measurement of a LSMO nanoisland. Note that our parameters meet the criteria for local work function measurements, and thus we expect our data to give reliable indications about the work function anisotropy in LSMO.

The general concepts outlined above to explain the nature of the surface dipole and of work function anisotropy are best suited for nearly-free electron metallic systems. Complex oxide metals such as LSMO are, however, very different metals. Note that LSMO surfaces have remained vastly unexplored until now, and the microscopic mechanisms leading to the formation of a surface dipole in LSMO are still unknown. For example, it is likely that the electron spill out, or even the Smoluchowski effect might not be relevant at all in this system, given the nature of the metallic state in LSMO (definitely not free-electron like). Conversely, there are other effects here that are absent in elemental metals, e.g. lattice distortions, and the possibility of having many different terminations or reconstructions for a given surface orientation. Also, the fact that we are dealing with a multicomponent compound raises concerns about the possibility of surface segregations, or yet other phenomena related to structural and/or chemical defects, added to a possible surface contamination (like water or carbon). All these effects are likely to be essential for determining the final surface dipole. Addressing this subject, therefore, would require further experimental and, very importantly, substantial theoretical efforts.

Also, concerning our specific experimental setup, we cannot be sure that the island remains at a fixed potential during the scan; indeed (see Fig. 5.41) the sample-holder is grounded, but the island lies electrically isolated, separated by the YSZ substrate. This means that one should use some care when interpreting the contact potential differences. On the other hand, the degree of repeatability of our measurements and the sharp contrast between facets suggest that the above (i.e. that the island remains at a constant potential) might be a reasonable assumption. If this is the case, our data indicate a difference in local work function of ~ 50 meV between the (111)_{LSMO} and (001)_{LSMO} facets of the LSMO

^{‡‡}Exceptions to this are found, for instance, in Al and Pb, FCC metals, in which the (100) plane exhibits the largest W [324].

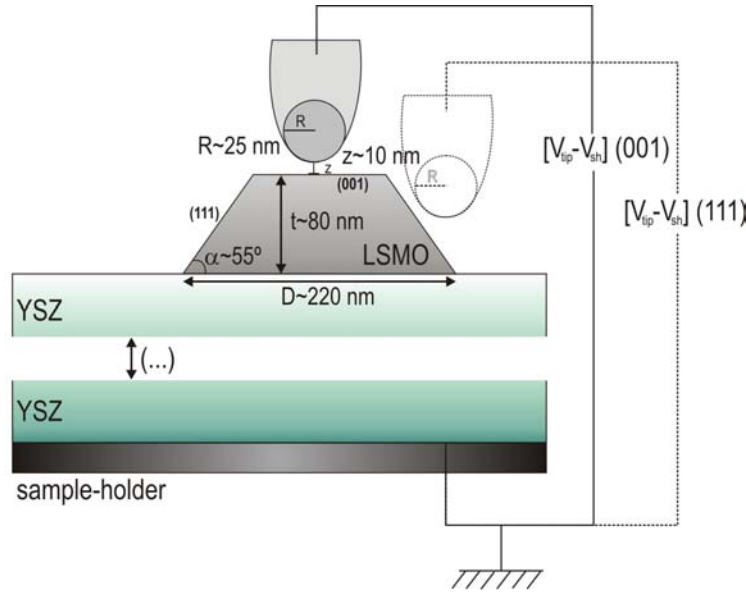


Fig. 5.41: Schematic diagram, drawn at scale, of the KPFM measurement of a LSMO square-base pyramid nanoisland. We have selected the island thickness t and lateral size D to be those of the nanoisland of Fig. 5.36, since its potential image shows a clear contrast between the $(111)_{\text{LSMO}}$ and the $(001)_{\text{LSMO}}$ facets. The tip to sample distance z and the tip radius R are also drawn at scale. Note how the extension of the LSMO facet is large enough to contain the whole probe width. On the other hand, z is small enough to probe $V_{\text{vac}}(s)$, i.e. the electrostatic potential ‘just outside’ the facet.

nanoislands. The contact potential was higher at the $(111)_{\text{LSMO}}$ facet, which implies a larger work function at the $(001)_{\text{LSMO}}$ facet (taking into account the negative sign of the electron charge).

5.2.6 Conclusions

Throughout this section we have studied the KPFM measurements on self-assembled LSMO nanoislands grown on YSZ substrates. After a general overview of the technique, we have described the experimental set-up used for sample imaging. Particular emphasis was given to the fact that the LSMO nanoislands lie on an insulating massive substrate. This makes the measurement especially challenging, both from a practical point of view (concerning the stability of the imaging process) and from a conceptual perspective. Regarding the latter, we have shown that the measured potential difference between the YSZ substrate and the LSMO nanoisland is independent from the contact potential difference between the tip and the sample holder, as deduced from considering the metallic tip and sample-holder as a parallel-plate capacitor system, with the YSZ/LSMO system sandwiched in between. Careful measurements of individual islands have revealed a contrast difference of ~ 50 mV among the $(111)_{\text{LSMO}}$ and $(001)_{\text{LSMO}}$ crystallographic planes. This contrast is especially clear in the largest nanoislands, where the tip can better resolve the potential variations due to a smaller tip-island convolution. The difference in work function between the different crystal facets of a metal is a well known issue, which has been widely investigated in simple metals but very little in complex oxides. Differences in the electric surface dipole, caused by variations in the spreading of the electronic density towards vacuum, lie at the

base of such work function anisotropy. According to our results, the $(001)_{\text{LSMO}}$ facet exhibits a higher work function than the $(111)_{\text{LSMO}}$ by around ~ 50 mV. LSMO is a multicomponent oxide and thus its facets can display different terminations [e.g. either (La,Sr)-O or Mn-O₂, or a mixture of the two in the case of the $(001)_{\text{LSMO}}$ plane]. The specific characteristics of the LSMO nanoisland facets are unknown at this stage. To ascribe the measured potential differences to a particular combination of terminations and to further assess the implications of our findings require for joint experimental and theoretical efforts.

General Conclusions

In this work we have explored nanoscale $\text{La}_{0.7}\text{Sr}_{0.3}\text{MnO}_3$ heteroepitaxial systems grown by a solution-based methodology onto different oxide single crystal substrates, including STO, LAO, YSZ, and MgO. The main results of this study are summarized in the following:

First, we have demonstrated that chemical solution deposition (CSD) is a successful approach for the fabrication of high quality epitaxial ferromagnetic LSMO ultra-thin films and 3D nanostructures. We have seen that, following identical growth procedures based on ultradiluted LSMO precursor solutions, the final system configuration relies on the choice of the substrate. In particular, ultra-thin LSMO films with thickness below ~ 10 nm are obtained on STO and LAO perovskite substrates, whereas onto YSZ fluorite and MgO rock-salt substrates, homogeneous dispersions of self-assembled nanoislands are achieved. These results are the experimental evidence of the key parameters ruling heteroepitaxial growth: elastic strain energy, and surface and interface energies. In the heteroepitaxy formed by two perovskite structure crystals, where the interface energy is expected to be low and the lattice mismatches are below 2%, LSMO grows in a thin-film configuration (onto STO and LAO). Conversely, the structural dissimilarity between LSMO and YSZ and MgO, along with the high lattice mismatches, brings the manganite to build into a 3D form.

Ultra-thin LSMO films on STO and LAO exhibit remarkably flat surface morphologies, with the tendency to reproduce the underlying substrate's step-terrace architecture. This trend is more pronounced for STO substrates, which display a very low $\epsilon \sim 0.9\%$ lattice mismatch against LSMO ($\epsilon \sim 2\%$ for LAO). As a matter of fact, the role of elastic energy is univocally manifested in that LSMO grows fully strained onto STO, while the larger mismatch with respect to LAO triggers LSMO to partially relax through misfit dislocations. The latter result contrasts with fully strained LSMO on LAO thin films, grown by vapor deposition techniques, reported in the literature. Furthermore, it highlights how the crystallization pathways and, consequently, the film microstructure, deeply depend on the processing route. Solution-derived LSMO ultra-thin films are found to be highly crystalline and epitaxial, and show no secondary phases. The versatility of CSD, in turn, is evidenced in the ability to tune the system of self-assembled nanoislands (i.e. the island size and density) by acting upon the solution concentration, the annealing times, and temperatures. Optimal precursor solution concentrations in the 0.015 M to 0.03 M (in Mn) range, and typical heat treatments at 900°C for 1 h to 3 h, yield highly uniform nanoisland ensembles. The amount of material in the nanostructured templates is given in terms of the equivalent thickness parameter, which varies from 1.5 to 3.5 (± 0.5) nm for the above concentrations. In general, dense nanoisland dispersions are formed on MgO, featuring islands with mean thickness $t \sim 7$ nm and lateral sizes $D \sim 50$ nm. Nanostructures on YSZ typically exhibit larger thickness values of $t \sim 20$ nm and lateral sizes D of around 100 nm. Anyhow, for these processing

conditions, nanoislands do not surpass the 200 nm of lateral size, which is already below the sizes commonly reached by lithography methods.

XRD pole-figure analyses have shown that LSMO nanoislands on YSZ exhibit a majority population of $(001)_{\text{LSMO}}$ out-of-plane oriented nanoislands, which exhibit two possible morphologies, regular-square and rotated-square, suggesting that distinct manganite crystal planes have similar surface energies. A minority triangle-shaped population was seen to display the $(111)_{\text{LSMO}}$ out-of-plane orientation. Meanwhile, LSMO on MgO shows a single population of cube-on-cube grown $(001)_{\text{LSMO}}$ nanoislands, with an in-plane rotated-square morphology displaying edges parallel to the $\langle 110 \rangle_{\text{MgO}}$ substrate step edges. TEM investigations have demonstrated that LSMO nanoislands on YSZ and MgO are highly relaxed.

Concerning the magnetic properties of the solution-derived LSMO ultra-thin films and nanoislands, we have shown evidence of Curie temperature values around ~ 350 K, i.e. close to reported bulk LSMO values, whether fully strained LSMO on STO, partially relaxed LSMO on LAO, or LSMO sub-200 nm lateral size nanoislands on YSZ. These are remarkable results considering the well documented tendency of vapor-deposited LSMO thin films to show depressed T_C values at very low film thicknesses, as well as taking into account the sub-200 nm lateral size of the nanoislands. Transport measurements in ultra-thin LSMO/STO and LSMO/LAO systems have shown that above average thicknesses of ~ 5.5 nm such films exhibit a metal-insulator transition which occurs at T_{MI} values well below their ferromagnetic-paramagnetic transition (measured at $T_C \sim 350$ K). Increased MR values have also been measured. An Anderson type of 2D localization in this very thin films, and the presence of structural or chemical disorder may be at the basis of these findings. To be able to shed more light into the physical mechanisms responsible for these results a deeper study is, however, in order.

The saturation magnetization in both ultra-thin LSMO films and LSMO nanoislands on YSZ was seen to be in the order of the reported values. For the LSMO on YSZ nanoisland system, however, we have found a trend towards lower magnetization with decreasing solution concentrations, i.e. with decreasing nanoisland size. The latter was explained in terms of a ferromagnetic dead-layer on the surface/interface of the nanoislands, which effect is enhanced for smaller islands (larger surface to volume ratios). We have also calculated the role of the different anisotropy contributions on the LSMO/YSZ nanoisland system, which features a biaxial in-plane anisotropy with the $[110]_{\text{LSMO}}$ in-plane easy axis, and a magnetocrystalline anisotropy constant value $K_1(150 \text{ K}) = -(5 \pm 1) \text{ kJ/m}^3$, measured for the first time in LSMO nanoislands. The exception to the good magnetic properties of these heteroepitaxial systems was found in the LSMO on MgO nanoislands. Their depressed magnetic behavior was discussed in terms of the strain state around dislocation cores, of the presence of a dead layer, and of the chemical interdiffusion between Mn and Mg. The latter mechanism is suggested by recent STEM-EELS evidence of Mn in the MgO substrate, and is currently under study.

The system of self-assembled ferromagnetic sub-200 nm lateral size LSMO nanoislands grown onto YSZ comprises a novel and challenging system. Moreover, it features many of the characteristics that are required from building blocks of potential devices, as discussed in the introduction of this work. These include room temperature ferromagnetism, high spin polarization, and sub-200 nm lateral size. Unveiling the functional nanoscale properties of these nanoislands was thus found of utmost interest, and has lead us to investigate them using MFM, PEEM and KPFM. These are all advanced techniques, in the sense that they are continuously evolving, they implement cutting-edge technologies, and in that

their characterization potential is at the frontier of knowledge, thus yielding both new discoveries and insight into them. We have given a general overview of these techniques, as well as emphasized the optimization of the experimental procedure. This has implied tuning the MFM operation through the choice of the appropriate magnetic tip, optimizing the necessary metal capping for PEEM experiments, and dealing with the challenge of an insulating substrate and its implications in KPFM measurements.

The MFM study of self-assembled LSMO nanoislands on YSZ has shown that different magnetic configurations arise from the interplay between nanoisland lateral size and thickness. This information is not accessible from macroscopic magnetometry measurements. In particular, we have identified single domain, multidomain, and vortex state configurations, in agreement with micromagnetic simulations. The vortex state appears in platelet-like nanoislands, when the competition between exchange energy and magnetostatic energy results in the in-plane curling of the magnetic moments, with an out-of-plane singularity at the center, known as the vortex core. The limited resolution of the MFM (around ~ 50 nm) and the small size of the nanoislands prevent from discerning their internal domain structure. However, the presence of the vortex core is well defined, as we conclude from the series of analyses done for a large number of nanoislands. We have also investigated the evolution of the ferromagnetic nanoislands under in-plane magnetic field. The vortex core appears to move parallel to the applied field, instead of perpendicular, as expected from a canonical vortex state. Further experiments and simulations are underway to give insight into these observations, which could be triggered by the specific characteristics of the nanoislands (their magnetocrystalline anisotropy, the truncated pyramid shape...etc.).

With respect to PEEM, by means of XAS studies we have concluded that LSMO on YSZ nanoislands exhibit the Mn^{3+}/Mn^{4+} ratio expected from the stoichiometric $La_{0.7}Sr_{0.3}MnO_3$ compound. We have also shown experimental evidence suggesting the presence of Mn^{2+} on the topmost surface layers, which can be related to the ferromagnetic dead layer responsible for the overall magnetization decrease measured by SQUID. XMCD experiments at room temperature and at 110 K have demonstrated that $(111)_{LSMO}$ out-of-plane oriented triangular nanoislands exhibit a vortex configuration, which we could not address by MFM because of the tip stray field. Furthermore, these vortices were seen to evolve towards a single domain state under in-plane external field, and to do so showing the expected vortex movement (core displacement perpendicular to the applied field).

Finally, KPFM measurements on LSMO nanoislands have opened the path to the local electrostatic characterization of nanoscale complex oxides, bringing interesting results and a number of questions regarding the underlying physical phenomena. In particular, we have observed that distinct crystallographic LSMO planes, namely $(001)_{LSMO}$ and $(111)_{LSMO}$, yield different electrostatic interaction with the conducting microscope probe. This is manifested in a relative potential variation of around ~ 50 mV between the two facets, suggesting that $(001)_{LSMO}$ crystallographic planes have a ~ 50 meV larger work function than $(111)_{LSMO}$ planes. The difference in work function among different crystal facets of simple metals is a well established issue, known as the work function anisotropy. This phenomenon, however, is best understood in the context of nearly-free electron metal systems. Hence, its implications in the complex multicomponent LSMO oxide are not straightforward and will require joint experimental and theoretical efforts.

In conclusion, this work has described the growth of nanoscale ferromagnetic manganese systems and their comprehensive characterization. On one hand, the scalability and cost-effectiveness of the solution-based approach, together with the nanometric dimension

and the magnetic properties of the manganite, meet the demands of the ever progressing nanotechnology field. On the other hand, the insight into the local properties of these systems opens new perspectives towards the exploration and understanding of nanoscale phenomena.

List of Abbreviations

2D	Two-dimensional
3D	Three-dimensional
AFM	Atomic force microscopy
BCC	Body centered cubic
CCD	Charge-coupled device
CMR	Colossal magnetoresistance
CPD	Contact potential difference
CSD	Chemical solution deposition
DE	Double exchange
DOS	Density of states
E_F	Fermi energy level
EELS	electron energy loss spectroscopy
FCC	Face centered cubic
FFT	Fast Fourier transform
FM	Ferromagnetic
FMR	Ferromagnetic resonance
FWHM	full width at half maximum
GMR	Giant magnetoresistance
GPA	Geometric phase analysis
HAADF	High angular annular dark field
HRTEM	High resolution transmission electron microscopy
KPFM	Kelvin force probe microscopy
LAO	LaAlO_3 Lanthanum aluminate
LSMO	$\text{La}_{0.7}\text{Sr}_{0.3}\text{MnO}_3$ Strontium-doped lanthanum manganite
LZO	$\text{La}_2\text{Zr}_2\text{O}_7$ Lanthanum zirconate
MBE	Molecular Beam epitaxy
MFM	Magnetic force microscopy
MOKE	Magneto-optical Kerr effect
MR	Magnetoresistance
(M)RAM	(Magnetic) random access memory
PEEM	Photoemission electron microscopy
PID controller	Proportional Integral Derivative controller
PLD	Pulsed laser deposition

PPMS	Physical properties measurement system
RMS	Root mean square
RT	Room temperature
SC	Simple cubic
SOFC	Solid oxide fuel cells
SP-STM	Spin-polarized Scanning tunneling microscopy
SPM	Scanning probe microscopy
SQUID	Superconducting quantum interference device
SRT	Spin reorientation transition
STEM	Scanning transmission electron microscopy
STM	Scanning tunneling microscopy
STO	SrTiO ₃ Strontium titanate
T_C	Curie temperature
T_{MI}	Metal-insulator transition temperature
TEM	Transmission electron microscopy
TEY	Total electron yield
UHV	Ultra-high vacuum
XANES	X-ray Absorption Near Edge Structure
XAS	X-ray absorption spectrum
XMCD	X-ray magnetic circular dichroism
XRD	X-ray diffraction
XRD ²	2D X-ray diffraction
YSZ	Y ₂ O ₃ :ZrO ₂ Yttria-stabilized zirconia

Appendix A

Experimental Techniques

In this section we briefly describe the main characteristics of the techniques that have been routinely used to characterize the $\text{La}_{0.7}\text{Sr}_{0.3}\text{MnO}_3$ (LSMO) nanoscale systems object of this work. These include: surface topography characterization by means of Atomic Force Microscopy (AFM), structural study using X-ray Diffraction (XRD) and Transmission Electron Microscopy (TEM), and magnetic and electrical characterization using Superconducting Quantum Interference Device (SQUID), Ferromagnetic Resonance (FMR), and transport measurements. Each of these techniques involves scientific and operating principles, as well as technical details that could lead to extensive descriptions. The aim of this appendix, however, is to provide the reader with a general idea of the working principles of these techniques and with the information of the specific measurements performed with them and of the instruments used.

A.1 Atomic Force Microscopy

Atomic Force Microscopy, AFM, was created in 1986 [329] as a further development of Binnig and Rohrer's first scanning probe microscope (SPM), i.e. the Scanning Tunneling Microscope, in 1982 [330]. As part of the SPM family, AFM measures the interactions between a sharp probe (the *tip*) and the studied sample with nanometric or even atomic lateral resolution. The *nm* range distance between the tip and the sample enables sensing very small forces in the 10^{-13} - 10^{-5} N range [221]. The specific property being measured depends on the nature of the force sensed by the tip (repulsive, attractive Van der Waals, magnetic, electrostatic...). This thesis widely treats the operation principle of SPM in its Magnetic Force Microscopy (MFM, Chapter 4) and Kelvin Probe Force Microscopy (KPFM, Chapter 5) variants, i.e. SPM techniques related to the measurement of magnetic and electrostatic properties, respectively. In turn, for the topography studies of LSMO ultra-thin films and 3D nanostructures described in Chapter 3 we have used systematically AFM, sensing the attractive Van der Waals forces between the tip and the sample in the Dynamic mode.

Sharp AFM tips typically have apex radii below the ~ 20 nm, and are fabricated on Si or Si_3N_4 . Their sharpness and the fact of approaching the tips at distances below the ~ 30 nm from the sample enables lateral and vertical resolutions of around ~ 0.1 - 0.2 nm and ~ 1 nm, respectively [221, 230]. Tips sit at the end of a soft spring called the cantilever, also known as the force detector. The sensitivity of the cantilever to the interactions is determined by

its geometry and its mechanical stiffness. The force constant k of the cantilever is therefore given by $k = Ew^3t/4l$, where E is Young's modulus, w is the lateral width (with typical values $\sim 10\text{-}30\text{ }\mu\text{m}$), t is the thickness ($\sim 3\text{-}5\text{ }\mu\text{m}$), and l is the length ($\sim 100\text{-}300\text{ }\mu\text{m}$). Cantilevers are also made of silicon or silicon nitride, by means of standard microfabrication techniques [331].

The forces between the tip and the sample are detected by measuring the bending and the torsion suffered by the cantilever due to the specific interactions at play. In the optical detection mode, a laser beam is focused on the rear side of the cantilever, at the end of which sits the tip, and its reflection is detected by a Position Sensitive Photo Diode (PSPD) (see Fig. A.1) The PSPD senses the shifts in position of the laser spot while the tip is scanning the sample. Upon comparing the signal measured with a user-specified set-point, an electronic feedback system sends the signal to the piezoelectric tubes under the sample to retract or expand in order to re-establish the value of the set-point. Such contractions/expansions are registered and form the topography images, which is hence a constant-deflection image. The piezoelectric tubes under the sample control not only the z movement, but also the xy scanning. Typical $x - y$ scan areas range from $0.5\text{ }\mu\text{m} \times 0.5\text{ }\mu\text{m}$ up to $20\text{ }\mu\text{m} \times 20\text{ }\mu\text{m}$.

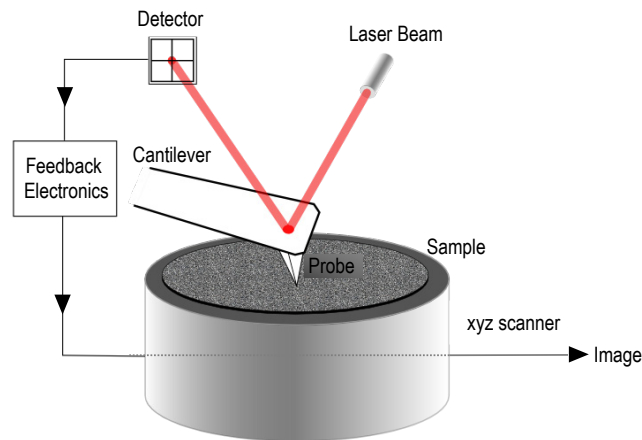


Fig. A.1: Schematic diagram of a AFM set up featuring the optical laser-reflection detection mode. Adapted from [332].

The AFM can operate in a variety of modes mainly depending on the environmental conditions and on the goal of the measurement [333]. In the *static* or *contact* mode, the tip is in mechanical contact with the sample surface and the forces are sensed through the bending and torsion of the cantilever mentioned above. The vertical deflection of the cantilever provides topography information while lateral deflection or torsion can be used to measure friction and wear properties of the sample. Electrical conduction measurements also require that tip and sample are in contact. Typical cantilever force constants for contact mode operation are very low, in the $0.01\text{-}1\text{ N/m}$ range. In the *dynamic* mode operation, which includes intermittent and non-contact modes, the cantilever is set to oscillate near its resonance frequency, at distances typically below the $\sim 30\text{ nm}$ from the sample surface. The forces between tip and sample are thus sensed by measuring the changes produced in the cantilever's oscillation amplitude, frequency, and phase, when the tip gets close to the sample [222]. Stiffer cantilevers are used, with force constants typically between $10\text{-}80\text{ N/m}$ and resonant frequencies in the $100\text{-}500\text{ kHz}$ range. Dynamic operation prevents tips

from wearing off so quickly and also damaging soft samples. It is used in ambient, liquid, and vacuum environment, and, besides providing topographical information, it can be used for the magnetic and electrostatic imaging of the sample with nanometric resolution (as explained in Chapters 4 and 5 of this thesis). Fig. A.2 shows the dependence of the tip-sample force with their separation, as well as the typical ranges where Contact and Non-Contact modes operate. Interleave refers to large distances usually used in lift-mode operation, where each line is scanned twice, one scan near the surface, the other scan away from it. At distances between ~ 1 nm to ~ 500 nm the interaction is attractive (<0) and below 1 nm it becomes repulsive due to the overlap of electronic orbitals upon decreasing the distance [334].

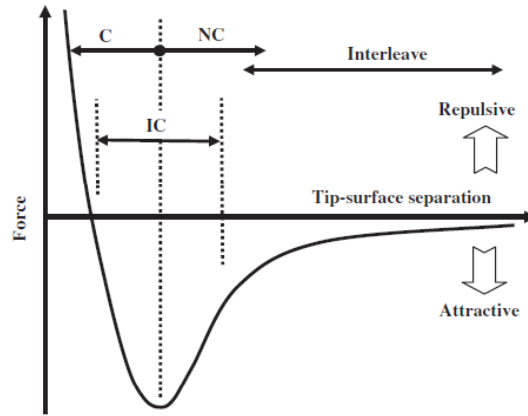


Fig. A.2: Schematic diagram of the force dependence with sample-tip separation. The range of distances at which different modes operate are indicated: Contact (C), Intermittent contact (IC), and Non-Contact (NC). Reproduced from [334].

Surface topography characterization of the nanoscale LSMO heteroepitaxys was performed in air, at room temperature, and, typically, in the intermittent contact mode. Three AFM equipments, located at ICMAB, were used for such purpose: an Agilent 5100, an Agilent 5500 LS (both from Molecular Imaging), and a Cervantes AFM (from Nanotec). Prior to imaging, samples were systematically cleaned with acetone and methanol in an ultrasonic bath. We used Si tips from Nanosensors, mounted onto rectangular Si cantilevers with force constants k around 40 N/m, and resonance frequencies in the 300-400 kHz range. The suppliers give tip radius values below ~ 10 nm [335]. Image processing was done using MountainsMap 5.1 (Digital Surf) and WSXM 5.0 [336] (Nanotec Electrónica) commercial softwares.

A.2 X-Ray Diffraction

X-ray diffraction (XRD) is based on the scattering of incident X-ray waves by the electronic density surrounding each atom in a crystal. X-rays are electromagnetic waves with wavelength λ in the 0.1-100 Å range. The atomic periodicity within crystals is also in the Å range. Diffraction phenomena occur when the spacing between the object (the crystal in this case) is in the order of the wavelength of the incident radiation, and, consequently,

X-ray diffraction is a powerful tool to characterize crystals. The scattered X-rays will destroy themselves except for the case in which the difference between the incident and the scattered wave vectors is a vector belonging to the reciprocal lattice. Or, more simply, according to Bragg's law, if the scattered rays are in-phase so that their difference in path is equal to an integer number n of wavelengths [see Fig. A.3 (a)]

$$n\lambda = 2d_{hkl} \sin \theta \quad (\text{A.1})$$

where λ is the wavelength of the incident X-ray, n is the reflection order (an integer number), θ is the angle of incidence between the X-ray and the sample plane, and d_{hkl} is the interplanar spacing between the (hkl) family of planes. When Bragg's law is fulfilled we have a constructive interference, i.e. the so-called diffraction peak or the Bragg reflection. The diffraction pattern is then composed by such Bragg reflections and their intensity and spatial distributions conform the fingerprint of the specific sample. XRD is thus routinely used for determining crystal structures, phase identification, crystalline quality, cell parameters, or the study of crystal texture and orientation of epitaxial thin films and nanostructures, among others.

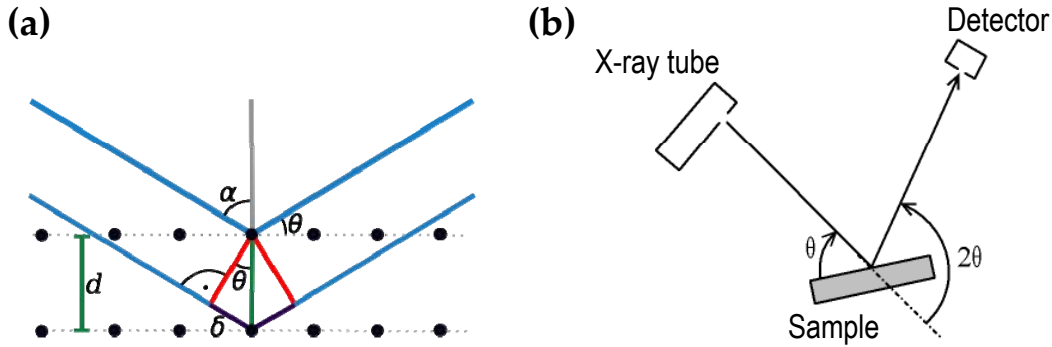


Fig. A.3: (a) Sketch of the constructive interference (Bragg's law) between two incident X-rays on a crystal surface. (b) Geometry of the $\theta - 2\theta$ configuration.

The rotation of the sample with respect to the incident angle and to the detector produces different XRD configurations from where different information can be obtained. In a $\theta - 2\theta$ scan [Bragg-Brentano geometry, Fig. A.3 (b)], the sample moves by the angle θ and the detector simultaneously moves by the angle 2θ while the X-ray tube remains stationary. Only the atomic planes parallel to the surface plane will diffract in this configuration, i.e. we obtain information of the out-of-plane orientation of the crystal. Polycrystalline samples consist of randomly oriented crystallites in all possible orientations so for every crystal plane that fulfills the Bragg condition at a certain θ value there will be a diffraction peak. Conversely, in single crystals, the family of planes parallel to the sample surface is the only one giving a reflection peak. Information on the out-of-plane texture of crystallites can be obtained by ω scans, also known as *rocking curves*. A ω scan is a θ scan at a fixed 2θ angle and provides information on the mosaic spread of the specific reflection being analyzed: the width of the peak obtained is proportional to the misorientation of the coherent domain being measured.

The $\theta - 2\theta$ and ω scans performed in this thesis were done using either a Siemens D5000 or a Rigaku Rotaflex RU-200BV diffractometer located at ICMAB, using Cu K_α radiation [$\lambda(K_{\alpha 1}^{Cu}) = 1.5406 \text{ \AA}$ and $\lambda(K_{\alpha 2}^{Cu}) = 1.5444 \text{ \AA}$]. Data acquisition was typically performed

with a 0.02° step size. The lattice parameters of the (001)-single crystal substrates used in this thesis (see Chapter 2) were obtained by the combination of $\theta - 2\theta$ and ω scans at two different (001) reflections (which enables getting rid of the instrumental uncertainty θ_0). We used $\theta - 2\theta$ scans to identify the $(001)_{\text{LSMO}}$ -oriented LSMO nanoislands on YSZ and MgO, and rocking curve measurements that gave information on the out-of-plane misorientation of the nanoisland ensemble. On the other hand, the proximity to the substrate 2θ values prevented from resolving the LSMO reflection of ultra-thin LSMO films (concentrations ≤ 0.03 M, thickness ≤ 4 nm) grown onto STO and LAO.

The other XRD measurement routinely performed in the characterization of the LSMO nanoislands were *pole figure* measurements (also called phi-scans). In a Pole Figure we select a particular hkl reflection which is put in Bragg condition. In order to do so, if the (hkl) planes are not parallel to the substrate, the sample has to be tilted a certain angle χ and rotated an angle ϕ . The rotation angles are displayed in Fig. A.4 (a). For instance, for epitaxial LSMO nanoislands growing $(001)_{\text{LSMO}}$ -oriented with respect to a (001)-oriented single crystal substrate, to detect the $(011)_{\text{LSMO}}$ reflection the sample must be tilted 45° and rotated some degrees in ϕ in order to catch one of the 90° separated four poles (the multiplicity of the (001) out-of-plane orientation is $m=4$). Hence, the 360° rotation of the sample around the (001) sample plane results in the $(011)_{\text{LSMO}}$ pole figure of Fig. A.4 (b). Moreover, by comparing the relative orientation in ϕ of the poles of the substrate and of the islands (or film) on top we can deduce the in-plane orientation of the epitaxy. In summary, the χ value indicates the out-of-plane orientation of the crystal, i.e. $(001)_{\text{LSMO}} \parallel (001)_{\text{YSZ}}$ while the position of the poles in ϕ points out that, in-plane, LSMO grows 45° rotated with respect to the YSZ substrate, i.e. $[110]_{\text{YSZ}} \parallel [010]_{\text{YSZ}}$.

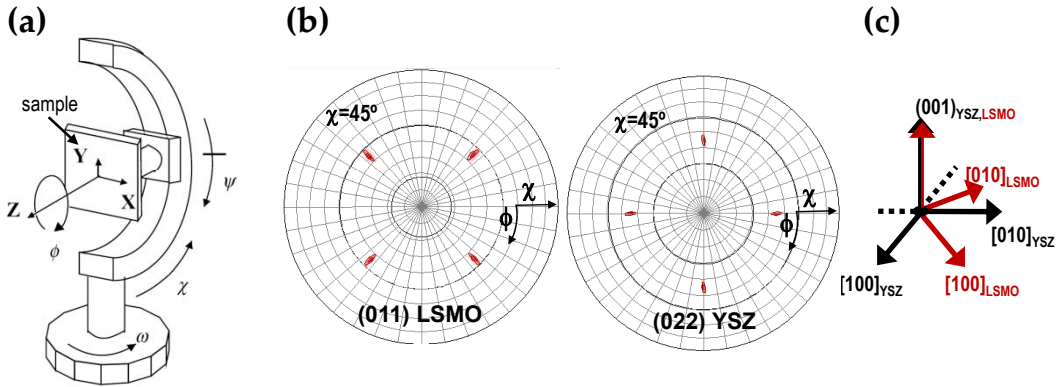


Fig. A.4: (a) Sketch of the goniometer showing the different rotation angles. X, Y, and Z are the sample reference system. Reproduced from [337]. (b) Pole figure measurement of a LSMO nanoisland ensemble on YSZ showing the $(001)_{\text{LSMO}}[110] \parallel (001)_{\text{YSZ}}[010]$ epitaxial orientation. (c) Sketch of the LSMO orientation relative to YSZ.

We performed pole figure measurements using a 2D X-Ray Diffraction (XRD²) system located at ICMAb, the GADDS D8 Advance System (Bruker), where GADDS stands for General Area Detector System. The sketched diagram of the GADDS main components is shown in Fig. A.5 (a). In addition to the goniometer sketched in Fig. A.4, the most salient feature in the GADDS system is the 2D detector, which permits simultaneously measuring large 2θ ($\sim 30^\circ$) and χ ($\sim 70^\circ$) ranges. In consequence, in a single fast measurement we obtain not only the information relative to the 2θ and χ values in which we center the

sample, but also detect reflections at different 2θ and χ values that give information on the out-of-plane texture of the sample [337].

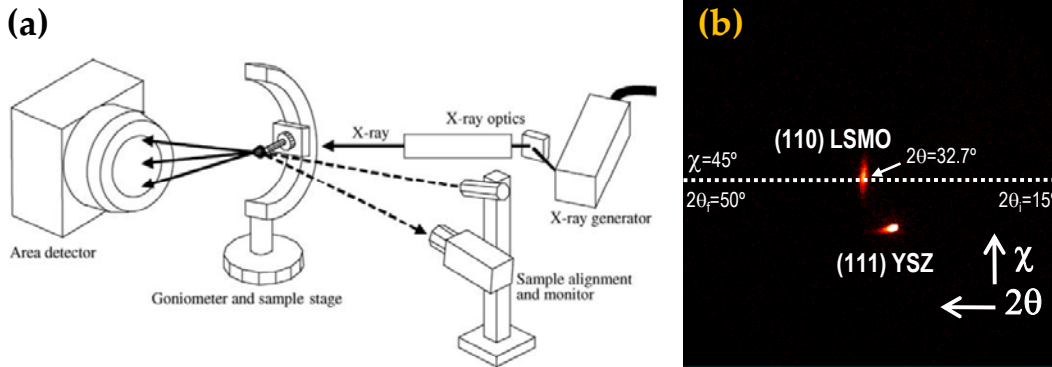


Fig. A.5: (a) Main components of a XRD² GADDS system. Reproduced from [337]. (b) 2θ - χ frame obtained from a GADDS measurement on a LSMO thin film (thickness ~ 25 nm) on a (001)-YSZ substrate.

An example of a 2D XRD diffraction pattern obtained with the GADDS is displayed in Fig. A.5 (b). The sample was a thin LSMO film (thickness ~ 25 nm) grown onto a (001)-YSZ substrate. The horizontal direction covers the 2θ values and the vertical direction represents χ values. The 2θ - χ frame shown in Fig. A.5 (b) was obtained by centering the sample at the (011)_{LSMO} reflection (falling at $2\theta=32.7^\circ$) and tilting it at a $\chi=45^\circ$. The bright reflection falling precisely at such χ and 2θ values indicates that the LSMO film grows with the (001)_{LSMO} out-of-plane orientation. To have the complete phi-scan we must rotate the sample about its normal axis (while tilted at 45°) and collect each of the frames. Integration in χ for the whole set of frames then produces a pole figure such as the one in Fig. A.4 (b). The low intensities coming from our LSMO nanoislands required long exposition times (each frame would take 120 s). In order to better resolve the out-of-plane misorientations in some of the nanoislands we also played with the ϕ step sizes, reducing it from the standard $\Delta\phi=2^\circ$ to $\Delta\phi=1^\circ$ and even $\Delta\phi=0.5^\circ$.

A.3 Transmission Electron Microscopy and Scanning Transmission Electron Microscopy

The following lines are based on a complete description of Transmission Electron Microscopy (TEM) given in the thesis by P. Abellán [160]. The reader is directed to this piece of work and to the references therein for further details on the technique.

Transmission Electron Microscopy (TEM) and Scanning Transmission Electron Microscopy (STEM) are powerful tools for characterizing the internal structure of materials with sub-nanometer resolution [338]. In TEM a parallel beam of accelerated electrons (acceleration voltages ~ 100 -300 kV) is directed towards a thin specimen, giving rise to scattering events and diffracted beams. The electrons traversing the specimen contain the information of the sample's atomic structure (known as the projected crystal potential, $f(x, y)$), and pass through an objective lens and a series of other lenses that focus and enlarge the information to finally build a magnified image of our sample. We can visualize the TEM

as a visible light microscope where the electron beam plays the role of light, and instead of glass lenses we have electromagnetic lenses which act upon the trajectories of the electrons. Fig. A.6 (a) shows a sketch of an ideal electron microscope. The analogy with the optical microscope is highlighted by illustrating the objective lens as a fictitious glass lens. The small wavelength of highly accelerated electrons permits very high lateral resolutions in the order of $\sim 1.5 \text{ \AA}$ – 2.5 \AA . Aberration-corrected microscopes can nowadays achieve resolution values of $\sim 0.5 \text{ \AA}$. STEM is based on the same principles as TEM, with the difference that the specimen is hit by a convergent electron beam which scans the sample (instead of a parallel static beam). This is achieved by placing the objective lens before the specimen, as sketched in Fig. A.6 (b).

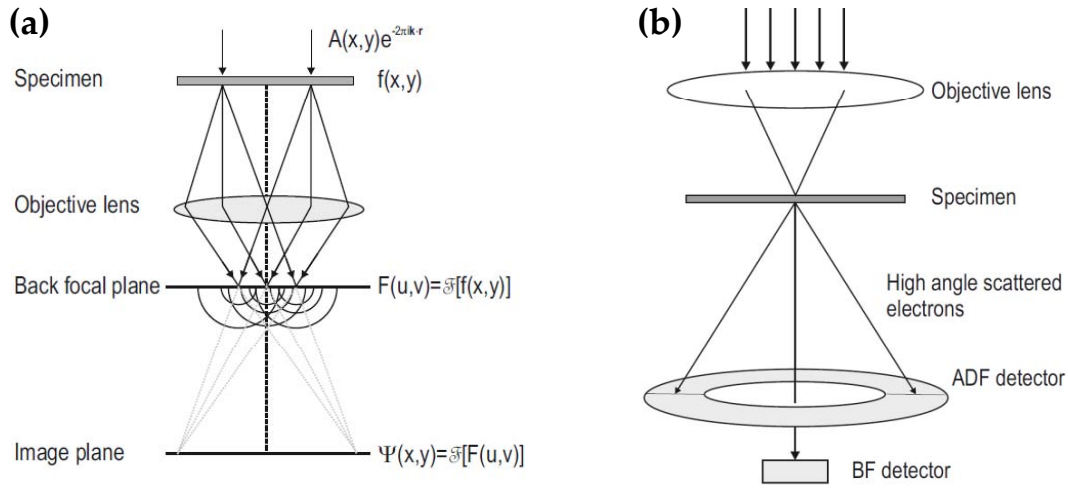


Fig. A.6: (a) Main components of an ideal TEM microscope, showing the mathematical evolution of the projected crystal potential $f(x,y)$. (b) Sketch of image formation within a STEM microscope. Illustrations reproduced from [160].

In addition to imaging the sample, TEM provides for structural and chemical information by means of Electron Diffraction (ED) and spectroscopic techniques such as Electron Energy Loss spectroscopy (EELS). Whether the ED pattern or the image of the sample is the information projected and thus visualized, is selected by adjusting the strength of one of the electromagnetic lenses (the intermediate lens). In both ED and imaging modes the information comes from coherently scattered elastic electrons, i.e. electrons that after interacting with the specimen keep a certain phase relationship and do not lose energy. Conversely, for High Annular Dark Field (HAADF) STEM imaging high angle inelastically scattered electrons are used. These are generally incoherent electrons, and it can be demonstrated that their intensity is proportional to Z^2 , where Z is the atomic number [339]. During STEM operation the direct (non-scattered) beam can also be selected. In that case STEM imaging is similar to TEM Bright Field imaging. The Z^2 dependency in HAADF-STEM mode implies that heavy atoms will be seen brighter than light atoms. A consequence of this dependence is that in HAADF-STEM the interpretation of the contrast is straightforward. This is an advantage with respect to High Resolution TEM (HRTEM) imaging, which despite yielding atomic resolution images, their interpretation is not direct: in HRTEM the contrast arises from differences in the phase of the beams scattered through the specimen, i.e. HRTEM images are interference images which strongly depend on the sample thickness and the microscope defocus. HRTEM image interpretation thus often requires a posteriori

simulations to unambiguously determine the origin of the observed contrasts.

TEM and STEM imaging is limited in practice by lens aberrations (astigmatism, chromatic and spherical aberrations) and, very importantly, by the quality of the sample, which mainly refers to its thickness. Specimens must be ‘electron-transparent’, which requires thicknesses below the 200 nm. For high resolution imaging the optimal thickness goes down to a few tens of nm. The samples imaged by TEM and STEM in this thesis were all cross-section samples prepared by the tripod mechanical preparation technique. The sample is cut into different slices, two slices are glued face to face, and the tripod polishing is applied to one of the two faces parallel to the substrate/film interface, until a thickness of ~ 20 μm is achieved. Further thinning down to electron transparency is obtained by Ar^+ ion bombardment on a Precision Ion Polishing System (PIPS), with low voltages in the 2-5 kV range (to minimize ion milling damage of the sample). The single crystal oxide substrates used in this thesis are very brittle and difficult to prepare. This process was principally carried out by Dr. P. Abellán in the context of her thesis, and also by F. Belarre and Dr. J. Gázquez.

A number of microscopes were used for the TEM and STEM images present in this thesis. LSMO thin films on STO and LAO substrates were imaged using two different aberration corrected STEMs: A VG Microscopes HB501UX and a Nion UltraSTEM at Oak Ridge National Laboratory (USA). Both of them were operated at 100 kV, equipped with NION aberration correctors (3rd order for the VG501 and 5th order for the NION UltraSTEM). Low magnification and ED patterns for LSMO nanoislands on YSZ were acquired with a Jeol JEM-2011 (200 kV) microscope at UAB (Barcelona) and a Philips CM30 (300 kV) microscope at Serveis Científic Tècnics of the UB (Barcelona). High resolution TEM images of LSMO nanoislands on YSZ were obtained using a Jeol 2010 FEG (200 kV) at Serveis Científic Tècnics of the UB (Barcelona). An aberration (C_s) corrected F20-SACTEM Tecnai microscope at CEMES (Toulouse) was used for high resolution imaging of MgO on LSMO nanoislands. Image acquisition and interpretation was carried out by Dr. P. Abellán, Dr. J. Gázquez, and Dr. M. Roldán.

A.4 Superconducting quantum interference device

Field and temperature dependent magnetization curves of LSMO ultra-thin films and self-assembled nanoislands were measured at ICMAB (B. Bozzo, Dr. C. Montón and J. Zabaleta) using a commercial SQUID DC-magnetometer (Quantum Design) equipped with a 7 T superconducting and a helium cryostat allowing temperature control between 1.8 K and 400 K. The isothermal magnetization curves showed a strong negative slope due to the diamagnetic contribution of the single crystal substrates. Data treatment involved getting rid of that contribution by linear fitting of the diamagnetic signal.

A SQUID consists of a superconducting loop with one or two non superconducting links inserted (the so-called Josephson junction). These devices give rise to an output voltage signal, which is a periodic function of the flux threading the superconducting loop. This geometry is known as DC-SQUID (constant bias current). The magnetometer includes a SQUID detection system and a precision temperature control unit in the bore of a high-field superconducting coil. The sample locates inside a set of pick-up coils, which in turn are placed inside the superconducting coil which provides a uniform dc-magnetic field at the sample location. The magnetized sample is then displaced inside the set of pick-up

coils inducing a current proportional to the variation of the magnetic flux. The signal is detected and amplified by means of the SQUID sensor (the superconducting loop with the weak link) in form of voltage. The magnetic moment of the sample is thus proportional to the voltage variations that the SQUID detects, which can resolve magnetic moments in the order of 10^{-6} emu. All the system is placed inside a helium cryostat which refrigerates the superconducting coil and allows precise temperature control.

A.5 Transport measurements

The electric transport measurements in the ultra-thin LSMO films on LAO and STO were performed by Dr. A. Palau using a Physical Properties Measurement System (PPMS) from Quantum Design located at the ICMAB. The system has a 9 T superconducting magnet and a helium cryostat which allows a precise temperature control between 1.8 K and 400 K. During the magnetotransport measurements, the magnetic field was applied out-of-plane of the LSMO film. Silver metal contacts were evaporated on the films and post-annealed, ensuring resistance values below $10\ \mu\Omega$. The resistivity of the LSMO films was measured in a four-point configuration with an applied current of 5 nA. Vacuum grease was used when mounting the sample to ensure good thermal coupling during the measurement.

Bibliography

- [1] S. D. Bader, *Colloquium: Opportunities in nanomagnetism*, *Rev. Mod. Phys.* **78**, 1 (2006).
- [2] G. Srajer, L. H. Lewis, S. D. Bader, A. J. Epstein, C. S. Fadley, E. E. Fullerton, A. Hoffmann, J. B. Kortright, K. M. Krishnan, S. A. Majetich, T. S. Rahman, C. A. Ross, M. B. Salamon, I. K. Schuller, T. C. Schulthess, and J. Z. Sun, *Advances in nanomagnetism via X-ray techniques*, *J. Magn. Magn. Mater.* **307**, 1 (2006).
- [3] J. V. Barth, G. Costantini, and K. Kern, *Engineering atomic and molecular nanostructures at surfaces*, *Nature* **437**, 671 (2005).
- [4] T. Ito and S. Okazaki, *Pushing the limits of lithography*, *Nature* **406**, 1027 (2000).
- [5] M. N. Yoder, *Microelectronics/nanoelectronics and the 21st century*, in *University/Government/Industry Microelectronics Symposium, 2001. Proceedings of the Fourteenth Biennial* (2001) pp. 2–7.
- [6] C. Moreno, P. Abellán, A. Hassini, A. Ruyter, A. P. del Pino, F. Sandiumenge, M. J. Casanove, J. Santiso, T. Puig, and X. Obradors, *Spontaneous outcropping of self-assembled insulating nanodots in solution-derived metallic ferromagnetic $\text{La}_{0.7}\text{Sr}_{0.3}\text{MnO}_3$ films*, *Adv. Funct. Mater.* **19**, 2139 (2009).
- [7] P. Abellán, F. Sandiumenge, M.-J. Casanove, M. Gibert, A. Palau, T. Puig, and X. Obradors, *Interaction between solution derived BaZrO_3 nanodot interfacial templates and $\text{YBa}_2\text{Cu}_3\text{O}_7$ films leading to enhanced critical currents*, *Acta Mater.* **59**, 2075 (2011).
- [8] A. Carretero-Genevri, J. Gázquez, J. C. Idrobo, J. Oró, J. Arbiol, M. Varela, E. Ferain, J. Rodríguez-Carvajal, T. Puig, N. Mestres, and X. Obradors, *Single crystalline $\text{La}_{0.7}\text{Sr}_{0.3}\text{MnO}_3$ molecular sieve nanowires with high temperature ferromagnetism*, *J. Am. Chem. Soc.* **133**, 4053 (2011).
- [9] M. Gibert, P. Abellán, L. Martínez, E. Román, A. Crespi, F. Sandiumenge, T. Puig, and X. Obradors, *Orientation and shape selection of self-assembled epitaxial $\text{Ce}_{1-x}\text{Gd}_x\text{O}_{2-y}$ nanostructures grown by chemical solution deposition*, *CrystEngComm* **13**, 6719 (2011).
- [10] T. Shinjo, T. Okuno, R. Hassdorf, K. Shigeto, and T. Ono, *Magnetic vortex core observation in circular dots of permalloy*, *Science* **289**, 930 (2000).
- [11] A. Ohtomo and H. Y. Hwang, *A high-mobility electron gas at the $\text{LaAlO}_3/\text{SrTiO}_3$ heterointerface*, *Nature* **427**, 423 (2004).
- [12] J. Gutiérrez, A. Llordés, J. Gázquez, M. Gibert, N. Romà, S. Ricart, A. Pomar, F. Sandiumenge, N. Mestres, T. Puig, and X. Obradors, *Strong isotropic flux pinning in solution-derived $\text{YBa}_2\text{Cu}_3\text{O}_{7-x}$ nanocomposite superconductor films*, *Nat. Mater.* **6**, 367 (2007).
- [13] M. Stengel, D. Vanderbilt, and N. A. Spaldin, *Enhancement of ferroelectricity at metal-oxide interfaces*, *Nat. Mater.* **8**, 392 (2009).
- [14] D. G. Schlom and J. Mannhart, *Oxide electronics: Interface takes charge over Si*, *Nat. Mater.* **10**, 168 (2011).
- [15] R. K. Vasudevan, Y. C. Chen, H. H. Tai, N. Balke, P. P. Wu, S. Bhattacharya, L. Q. Chen, Y. H. Chu, I. N. Lin, S. V. Kalinin, and V. Nagarajan, *Exploring topological defects in epitaxial BiFeO_3 thin films*, *ACS Nano* **5**, 879 (2011).
- [16] S. Jin, M. McCormack, T. H. Tiefel, and R. Ramesh, *Colossal magnetoresistance in La-Ca-Mn-O ferromagnetic thin films (invited)*, *J. Appl. Phys.* **76**, 6929 (1994).

- [17] Y. Tokura and Y. Tomioka, *Colossal magnetoresistive manganites*, *J. Magn. Magn. Mater.* **200**, 1 (1999).
- [18] J. H. Park, E. Vescovo, H. J. Kim, C. Kwon, R. Ramesh, and T. Venkatesan, *Direct evidence for a half-metallic ferromagnet*, *Nature* **392**, 794 (1998).
- [19] J. H. Park, E. Vescovo, H. J. Kim, C. Kwon, R. Ramesh, and T. Venkatesan, *Magnetic properties at surface boundary of a half-metallic ferromagnet $\text{La}_{0.7}\text{Sr}_{0.3}\text{MnO}_3$* , *Phys. Rev. Lett.* **81**, 1953 (1998).
- [20] G. A. Prinz, *Magnetoelectronics*, *Science* **282**, 1660 (1998).
- [21] S. D. Bader and S. S. P. Parkin, *Spintronics*, *Annual Review of Condensed Matter Physics* **1**, 71 (2010).
- [22] F. Yang, N. Kemik, M. D. Biegalski, H. M. Christen, E. Arenholz, and Y. Takamura, *Strain engineering to control the magnetic and magnetotransport properties of $\text{La}_{0.67}\text{Sr}_{0.33}\text{MnO}_3$ thin films*, *Appl. Phys. Lett.* **97**, 092503 (2010).
- [23] B. Kim, D. Kwon, J. H. Song, Y. Hikita, B. G. Kim, and H. Y. Hwang, *Finite size effect and phase diagram of ultra-thin $\text{La}_{0.7}\text{Sr}_{0.3}\text{MnO}_3$* , *Solid State Communications* **150**, 598 (2010).
- [24] B. Kim, D. Kwon, T. Yajima, C. Bell, Y. Hikita, B. G. Kim, and H. Y. Hwang, *Reentrant insulating state in ultrathin manganite films*, *Appl. Phys. Lett.* **99**, 092513 (2011).
- [25] J. Z. Sun, D. W. Abraham, R. A. Rao, and C. B. Eom, *Thickness-dependent magnetotransport in ultrathin manganite films*, *Appl. Phys. Lett.* **74**, 3017 (1999).
- [26] Y. H. Sun, Y. G. Zhao, H. F. Tian, C. M. Xiong, B. T. Xie, M. H. Zhu, S. Park, W. D. Wu, and J. Q. Li, *Electric and magnetic modulation of fully strained dead layers in $\text{La}_{0.67}\text{Sr}_{0.33}\text{MnO}_3$* , *Phys. Rev. B* **78**, (2008).
- [27] C. Kwon, M. C. Robson, K. C. Kim, J. Y. Gu, S. E. Lofland, S. M. Bhagat, Z. Trajanovic, M. Rajeswari, T. Venkatesan, A. R. Kratz, R. D. Gomez, and R. Ramesh, *Stress-induced effects in epitaxial $(\text{La}_{0.7}\text{Sr}_{0.3})\text{MnO}_3$ films*, *J. Magn. Magn. Mater.* **172**, 229 (1997).
- [28] R. Desfeux, S. Bailleul, A. Da Costa, W. Prellier, and A. M. Haghiri-Gosnet, *Substrate effect on the magnetic microstructure of $\text{La}_{0.7}\text{Sr}_{0.3}\text{MnO}_3$ thin films studied by magnetic force microscopy*, *Appl. Phys. Lett.* **78**, 3681 (2001).
- [29] J. Dho, Y. N. Kim, Y. S. Hwang, J. C. Kim, and N. H. Hur, *Strain-induced magnetic stripe domains in $\text{La}_{0.7}\text{Sr}_{0.3}\text{MnO}_3$ thin films*, *Appl. Phys. Lett.* **82**, 1434 (2003).
- [30] J. Dho and N. H. Hur, *Thickness dependence of perpendicular magnetic anisotropy in $\text{La}_{0.7}\text{Sr}_{0.3}\text{MnO}_3$ films on LaAlO_3* , *J. Magn. Magn. Mater.* **318**, 23 (2007).
- [31] Q. A. Pankhurst, J. Connolly, S. K. Jones, and J. Dobson, *Applications of magnetic nanoparticles in biomedicine*, *J. Phys. D: Appl. Phys.* **36**, R167 (2003).
- [32] W. J. Gallagher and S. S. P. Parkin, *Development of the magnetic tunnel junction MRAM at IBM: From first junctions to a 16-Mb MRAM demonstrator chip*, *IBM Journal of Research and Development* **50**, 5 (2006).
- [33] Y. Song and D. Zhu, *High Density Data Storage: Principle, Technology, and Materials* (World Scientific Publishing Company, 2009).
- [34] S. N. Piramanayagam and T. C. Chong, *Developments in Data Storage: Materials Perspective* (John Wiley & Sons, 2011).
- [35] D. Weller and A. Moser, *Thermal effect limits in ultrahigh-density magnetic recording*, *Magnetics, IEEE Transactions on* **35**, 4423 (1999).
- [36] A. Hubert and R. Schäfer, *Domain theory magnetic domains* (Springer Berlin Heidelberg, 1998) pp. 99–335.
- [37] A. Aharoni, *Upper bound to a single-domain behavior of a ferromagnetic cylinder*, *J. Appl. Phys.* **68**, 2892 (1990).
- [38] R. P. Cowburn, D. K. Koltsov, A. O. Adeyeye, M. E. Welland, and D. M. Tricker, *Single-domain circular nanomagnets*, *Phys. Rev. Lett.* **83**, 1042 (1999).
- [39] K. Y. Guslienko and K. L. Metlov, *Evolution and stability of a magnetic vortex in a small cylindrical ferromagnetic particle under applied field*, *Phys. Rev. B* **63**, 100403 (2001).

- [40] R. Wiesendanger, I. V. Shvets, D. Bürgler, G. Tarrach, H. J. Güntherodt, J. M. D. Coey, and S. Gräser, *Topographic and magnetic-sensitive scanning tunneling microscope study of magnetite*, *Science* **255**, 583 (1992).
- [41] M. Bode, *Spin-polarized scanning tunnelling microscopy*, *Reports on Progress in Physics* **66**, 523 (2003).
- [42] A. Schwarz and R. Wiesendanger, *Magnetic sensitive force microscopy*, *Nano Today* **3**, 28.
- [43] K. Yamada, S. Kasai, Y. Nakatani, K. Kobayashi, H. Kohno, A. Thiaville, and T. Ono, *Electrical switching of the vortex core in a magnetic disk*, *Nat. Mater.* **6**, 269 (2007).
- [44] A. Wachowiak, J. Wiebe, M. Bode, O. Pietzsch, M. Morgenstern, and R. Wiesendanger, *Direct observation of internal spin structure of magnetic vortex cores*, *Science* **298**, 577 (2002).
- [45] S. B. Choe, Y. Acremann, A. Scholl, A. Bauer, A. Doran, J. Stohr, and H. A. Padmore, *Vortex core-driven magnetization dynamics*, *Science* **304**, 420 (2004).
- [46] K. S. Buchanan, K. Y. Guslienko, A. Doran, A. Scholl, S. D. Bader, and V. Novosad, *Magnetic remanent states and magnetization reversal in patterned trilayer nanodots*, *Phys. Rev. B* **72**, 134415 (2005).
- [47] V. Novosad, M. Grimsditch, K. Y. Guslienko, P. Vavassori, Y. Otani, and S. D. Bader, *Spin excitations of magnetic vortices in ferromagnetic nanodots*, *Phys. Rev. B* **66**, 052407 (2002).
- [48] R. P. Cowburn, *Magnetic nanodots for device applications*, *J. Magn. Magn. Mater.* **242**, 505 (2002).
- [49] B. Pigeau, G. De Loubens, O. Klein, A. Riegler, F. Lochner, G. Schmidt, L. W. Molenkamp, V. S. Tiberkevich, and A. N. Slavin, *A frequency-controlled magnetic vortex memory*, *Appl. Phys. Lett.* **96** (2010).
- [50] V. S. Pribiag, I. N. Krivorotov, G. D. Fuchs, P. M. Braganca, O. Ozatay, J. C. Sankey, D. C. Ralph, and R. A. Buhrman, *Magnetic vortex oscillator driven by d.c. spin-polarized current*, *Nat. Phys.* **3**, 498 (2007).
- [51] A. Ruotolo, V. Cros, B. Georges, A. Dussaux, J. Grollier, C. Deranlot, R. Guillemet, K. Bouzehouane, S. Fusil, and A. Fert, *Phase-locking of magnetic vortices mediated by antivortices*, *Nat. Nanotechnol.* **4**, 528 (2009).
- [52] S. Kasai, K. Nakano, K. Kondou, N. Ohshima, K. Kobayashi, and T. Ono, *Three-terminal device based on the current-induced magnetic vortex dynamics with the magnetic tunnel junction*, *Applied Physics Express* **1**, (2008).
- [53] T. Nozaki, H. Kubota, S. Yuasa, M. Shiraishi, T. Shinjo, and Y. Suzuki, *RF amplification in a three-terminal magnetic tunnel junction with a magnetic vortex structure*, *Appl. Phys. Lett.* **95**, (2009).
- [54] J. I. Martín, J. Nogués, K. Liu, J. L. Vicent, and I. K. Schuller, *Ordered magnetic nanostructures: fabrication and properties*, *J. Magn. Magn. Mater.* **256**, 449 (2003).
- [55] B. T. Jonker, K. H. Walker, E. Kisker, G. A. Prinz, and C. Carbone, *Spin-polarized photoemission study of epitaxial Fe(001) films on Ag(001)*, *Phys. Rev. Lett.* **57**, 142 (1986).
- [56] N. C. Koon, B. T. Jonker, F. A. Volkening, J. J. Krebs, and G. A. Prinz, *Direct evidence for perpendicular spin orientations and enhanced hyperfine fields in ultrathin Fe(100) films on Ag(100)*, *Phys. Rev. Lett.* **59**, 2463 (1987).
- [57] C. Liu, E. R. Moog, and S. D. Bader, *Polar Kerr-effect observation of perpendicular surface anisotropy for ultrathin fcc Fe grown on Cu(100)*, *Phys. Rev. Lett.* **60**, 2422 (1988).
- [58] A. P. Popov, N. V. Skorodumova, and O. Eriksson, *Phenomenological model of the magnetic states of ferromagnetic film with competing surface and bulk anisotropies*, *Phys. Rev. B* **77**, 014415 (2008).
- [59] R. P. Cowburn, A. O. Adeyeye, and M. E. Welland, *Configurational anisotropy in nanomagnets*, *Phys. Rev. Lett.* **81**, 5414 (1998).
- [60] R. P. Cowburn and M. E. Welland, *Phase transitions in planar magnetic nanostructures*, *Appl. Phys. Lett.* **72**, 2041 (1998).
- [61] R. P. Cowburn and M. E. Welland, *Micromagnetics of the single-domain state of square ferromagnetic nanostructures*, *Phys. Rev. B* **58**, 9217 (1998).
- [62] Y. Suzuki, H. Y. Hwang, S. W. Cheong, T. Siegrist, R. B. van Dover, A. Asamitsu, and Y. Tokura, *Magnetic anisotropy of doped manganite thin films and crystals*, *J. Appl. Phys.* **83**, 7064 (1998).

-
- [63] M. Bibes, L. Balcells, S. Valencia, J. Fontcuberta, M. Wojcik, E. Jedryka, and S. Nadolski, *Nanoscale multiphase separation at $\text{La}_{2/3}\text{Ca}_{1/3}\text{MnO}_3/\text{SrTiO}_3$ interfaces*, *Phys. Rev. Lett.* **8706**, (2001).
 - [64] J. L. Maurice, F. Pailloux, A. Barthélémy, O. Durand, D. Imhoff, R. Lyonnet, A. Rocher, and J. P. Contour, *Strain relaxation in the epitaxy of $\text{La}_{2/3}\text{Sr}_{1/3}\text{MnO}_3$ grown by pulsed-laser deposition on $\text{SrTiO}_3(001)$* , *Philos. Mag.* **83**, 3201 (2003).
 - [65] C. Adamo, X. Ke, H. Q. Wang, H. L. Xin, T. Heeg, M. E. Hawley, W. Zander, J. Schubert, P. Schiffer, D. A. Muller, L. Maritato, and D. G. Schlom, *Effect of biaxial strain on the electrical and magnetic properties of (001) $\text{La}_{0.7}\text{Sr}_{0.3}\text{MnO}_3$ thin films*, *Appl. Phys. Lett.* **95**, (2009).
 - [66] Y. Takamura, R. V. Chopdekar, A. Scholl, A. Doran, J. A. Liddle, B. Harteneck, and Y. Suzuki, *Tuning magnetic domain structure in nanoscale $\text{La}_{0.7}\text{Sr}_{0.3}\text{MnO}_3$ islands*, *Nano Lett.* **6**, 1287 (2006).
 - [67] M. Mathews, R. Jansen, G. Rijnders, J. C. Lodder, and D. H. A. Blank, *Magnetic oxide nanowires with strain-controlled uniaxial magnetic anisotropy direction*, *Phys. Rev. B* **80**, (2009).
 - [68] A. M. Haghir-Gosnet and J. P. Renard, *CMR manganites: physics, thin films and devices*, *J. Phys. D: Appl. Phys.* **36**, R127 (2003).
 - [69] N. Suzuki, H. Tanaka, and T. Kawai, *Epitaxial transition metal oxide nanostructures fabricated by a combination of AFM lithography and molybdenum lift-off*, *Adv. Mater.* **20**, 909 (2008).
 - [70] E. Dagotto, *Complexity in strongly correlated electronic systems*, *Science* **309**, 257 (2005).
 - [71] E. Dagotto, T. Hotta, and A. Moreo, *Colossal magnetoresistant materials: the key role of phase separation*, *Physics Reports* **344**, 1 (2001).
 - [72] A. P. Ramirez, *Colossal magnetoresistance*, *Journal of Physics-Condensed Matter* **9**, 8171 (1997).
 - [73] C. N. R. Rao, A. Anthony, A. K. Cheetham, and R. Bernard, *Charge ordering in the rare earth manganates: the experimental situation*, *Journal of Physics: Condensed Matter* **12**, R83 (2000).
 - [74] M. B. Salamon and M. Jaime, *The physics of manganites: Structure and transport*, *Reviews of Modern Physics* **73**, 583 (2001).
 - [75] G. H. Jonker and J. H. Van Santen, *Ferromagnetic compounds of manganese with perovskite structure*, *Physica* **16**, 337 (1950).
 - [76] C. Zener, *Interaction between the d-shells in the transition metals. II. Ferromagnetic compounds of manganese with perovskite structure*, *Phys. Rev.* **82**, 403 (1951).
 - [77] P. W. Anderson and H. Hasegawa, *Considerations on double exchange*, *Phys. Rev.* **100**, 675 (1955).
 - [78] P. G. de Gennes, *Effects of double exchange in magnetic crystals*, *Phys. Rev.* **118**, 141 (1960).
 - [79] S. Jin, T. H. Tiefel, M. McCormack, R. A. Fastnacht, R. Ramesh, and L. H. Chen, *Thousandfold change in resistivity in magnetoresistive La-Ca-Mn-O films*, *Science* **264**, 413 (1994).
 - [80] M. N. Baibich, J. M. Broto, A. Fert, F. N. Van Dau, F. Petroff, P. Etienne, G. Creuzet, A. Friederich, and J. Chazelas, *Giant magnetoresistance of (001)Fe/(001)Cr magnetic superlattices*, *Phys. Rev. Lett.* **61**, 2472 (1988).
 - [81] H. Y. Hwang, S. W. Cheong, N. P. Ong, and B. Batlogg, *Spin-polarized intergrain tunneling in $\text{La}_{2/3}\text{Sr}_{1/3}\text{MnO}_3$* , *Phys. Rev. Lett.* **77**, 2041 (1996).
 - [82] A. Urushibara, Y. Moritomo, T. Arima, A. Asamitsu, G. Kido, and Y. Tokura, *Insulator-metal transition and giant magnetoresistance in $\text{La}_{1-x}\text{Sr}_x\text{MnO}_3$* , *Phys. Rev. B* **51**, 14103 (1995).
 - [83] R. A. de Groot, F. M. Mueller, P. G. v. Engen, and K. H. J. Buschow, *New class of materials: Half-metallic ferromagnets*, *Phys. Rev. Lett.* **50**, 2024 (1983).
 - [84] K. Schwarz, *CrO_2 predicted as a half-metallic ferromagnet*, *Journal of Physics F: Metal Physics* **16**, L211 (1986).
 - [85] R. J. Soulen, J. M. Byers, M. S. Osofsky, B. Nadgorny, T. Ambrose, S. F. Cheng, P. R. Broussard, C. T. Tanaka, J. Nowak, J. S. Moodera, A. Barry, and J. M. D. Coey, *Measuring the spin polarization of a metal with a superconducting point contact*, *Science* **282**, 85 (1998).

- [86] J. M. De Teresa, A. Barthélémy, A. Fert, J. P. Contour, F. Montaigne, and P. Seneor, *Role of metal-oxide interface in determining the spin polarization of magnetic tunnel junctions*, *Science* **286**, 507 (1999).
- [87] M. Bowen, M. Bibes, A. Barthélemy, J. P. Contour, A. Anane, Y. Lemaitre, and A. Fert, *Nearly total spin polarization in $\text{La}_{2/3}\text{Sr}_{1/3}\text{MnO}_3$ from tunneling experiments*, *Appl. Phys. Lett.* **82**, 233 (2003).
- [88] A. Solignac, R. Guerrero, G. Agnus, C. Fermon, M. Pannetier-Lecoeur, and P. Lecoeur, *Magnetic tunnels junctions for all-oxide spin valves devices*, *Journal of Physics: Conference Series* **303**, 012059 (2011).
- [89] M. C. Martin, G. Shirane, Y. Endoh, K. Hirota, Y. Moritomo, and Y. Tokura, *Magnetism and structural distortion in the $\text{La}_{0.7}\text{Sr}_{0.3}\text{MnO}_3$ metallic ferromagnet*, *Phys. Rev. B* **53**, 14285 (1996).
- [90] K. Steenbeck, T. Habisreuther, C. Dubourdieu, and J. P. Senateur, *Magnetic anisotropy of ferromagnetic $\text{La}_{0.7}\text{Sr}_{0.3}\text{MnO}_3$ epitaxial thin films: Dependence on temperature and film thickness*, *Appl. Phys. Lett.* **80**, 3361 (2002).
- [91] V. M. Goldschmidt, *The laws of crystal chemistry*, *Naturwissenschaften* **14**, 477 (1926).
- [92] J. M. Phillips, *Substrate selection for high-temperature superconducting thin films*, *J. Appl. Phys.* **79**, 1829 (1996).
- [93] L. W. Martin, Y. H. Chu, and R. Ramesh, *Advances in the growth and characterization of magnetic, ferroelectric, and multiferroic oxide thin films*, *Materials Science and Engineering: R: Reports* **68**, 89 (2010).
- [94] H. U. Habermeier, *Thin films of perovskite-type complex oxides*, *Materials Today* **10**, 34 (2007).
- [95] R. Ramesh and N. A. Spaldin, *Multiferroics: progress and prospects in thin films*, *Nat. Mater.* **6**, 21 (2007).
- [96] G. H. Kwei, A. C. Lawson, S. J. L. Billinge, and S. W. Cheong, *Structures of the ferroelectric phases of Barium-Titanate*, *J. Phys. Chem.* **97**, 2368 (1993).
- [97] R. H. Buttner and E. N. Maslen, *Electron difference density and structural parameters in CaTiO_3* , *Acta Crystallogr., Sect. B: Struct. Sci.* **48**, 644 (1992).
- [98] C. J. Howard, B. J. Kennedy, and B. C. Chakoumakos, *Neutron powder diffraction study of rhombohedral rare-earth aluminates and the rhombohedral to cubic phase transition*, *J. Phys.: Condens. Matter* **12**, 349 (2000).
- [99] F. W. Lytle, *X-Ray diffractometry of low-temperature phase transformations in Strontium Titanate*, *J. Appl. Phys.* **35**, 2212 (1964).
- [100] C. J. Howard and H. T. Stokes, *Structures and phase transitions in perovskites - a group-theoretical approach*, *Acta Crystallogr., Sect. A: Found. Crystallogr.* **61**, 93 (2005).
- [101] R. H. Mitchell, A. R. Chakhmouradian, and P. M. Woodward, *Crystal chemistry of perovskite-type compounds in the taunonite-loparite series, $(\text{Sr}_{1-2x}\text{Na}_x\text{La}_x)\text{TiO}_3$* , *Phys. Chem. Miner.* **27**, 583 (2000).
- [102] S. Geller and V. B. Bala, *Crystallographic studies of perovskite-like compounds. II. Rare earth alluminates*, *Acta Crystallogr.* **9**, 1019 (1956).
- [103] J. F. Scott, *Raman study of trigonal-cubic phase transitions in rare-earth aluminates*, *Phys. Rev.* **183**, 823 (1969).
- [104] S. Bueble, K. Knorr, E. Brecht, and W. W. Schmahl, *Influence of the ferroelastic twin domain structure on the (100) surface morphology of LaAlO_3 HTSC substrates*, *Surf. Sci.* **400**, 345 (1998).
- [105] G. W. Berkstresser, A. J. Valentino, and C. D. Brandle, *Growth of single crystals of lanthanum aluminate*, *J. Cryst. Growth* **109**, 457 (1991).
- [106] C. H. Kim, J. W. Jang, S. Y. Cho, I. T. Kim, and K. S. Hong, *Ferroelastic twins in LaAlO_3 polycrystals*, *Physica B: Condensed Matter* **262**, 438 (1999).
- [107] W. Langel and M. Parrinello, *Hydrolysis at stepped MgO surfaces*, *Phys. Rev. Lett.* **73**, 504 (1994).
- [108] A. Wander, I. J. Bush, and N. M. Harrison, *Stability of rocksalt polar surfaces: An ab initio study of $\text{MgO}(111)$ and $\text{NiO}(111)$* , *Phys. Rev. B* **68**, (2003).
- [109] R. A. Evarestov and A. V. Bandura, *HF and DFT calculations of MgO surface energy and electrostatic potential using two- and three-periodic models*, *International Journal of Quantum Chemistry* **100**, 452 (2004).

- [110] Y. Hao, M. Mihaylov, E. Ivanova, K. Hadjiivanov, H. Knozinger, and B. C. Gates, CO oxidation catalyzed by gold supported on MgO: Spectroscopic identification of carbonate-like species bonded to gold during catalyst deactivation, *J. Catal.* **261**, 137 (2009).
- [111] J. Du, S. Gnanarajan, and A. Bendavid, Influence of MgO surface conditions on the in-plane crystal orientation and critical current density of epitaxial YBCO films, *Physica C-Superconductivity* **400**, 143 (2004).
- [112] M. V. Jacob, J. Mazierska, N. Savvides, S. Ohshima, and S. Oikawa, Comparison of microwave properties of YBCO films on MgO and LaAlO₃ substrates, *Physica C: Superconductivity* **372-376**, 474 (2002).
- [113] V. G. Tsirelson, A. S. Avilov, Y. A. Abramov, E. L. Belokoneva, R. Kitaneh, and D. Feil, X-Ray and electron diffraction study of MgO, *Acta Crystallogr., Sect. B: Struct. Sci.* **54**, 8 (1998).
- [114] M. Yoshimura, Phase-stability of zirconia, *Am. Ceram. Soc. Bull.* **67**, 1950 (1988).
- [115] C. Pascual and P. Duran, Subsolvus phase-equilibria and ordering in the system ZrO₂-Y₂O₃, *J. Am. Ceram. Soc.* **66**, 23 (1983).
- [116] A. Weber and E. Ivers-Tiffée, Materials and concepts for solid oxide fuel cells (SOFCs) in stationary and mobile applications, *J. Power Sources* **127**, 273 (2004).
- [117] X. Xia, R. Oldman, and R. Catlow, Computational modeling study of bulk and surface of yttria-stabilized cubic zirconia, *Chemistry of Materials* **21**, 3576 (2009).
- [118] M. Yashima, S. Sasaki, M. Kakihana, Y. Yamaguchi, H. Arashi, and M. Yoshimura, Oxygen-induced structural change of the tetragonal phase around the tetragonal-cubic phase-boundary in ZrO₂-YO_{1.5} solid-solutions, *Acta Crystallogr., Sect. B: Struct. Sci.* **50**, 663 (1994).
- [119] K. S. Lee, S. Choi, and S. K. Kim, Radiation of spin waves from magnetic vortex cores by their dynamic motion and annihilation processes, *Appl. Phys. Lett.* **87** (2005).
- [120] C. Noguera, *Physics and chemistry at oxide surfaces* (Cambridge University Press, 1996).
- [121] M. Kawasaki, K. Takahashi, T. Maeda, R. Tsuchiya, M. Shinohara, O. Ishiyama, T. Yonezawa, M. Yoshimoto, and H. Koinuma, Atomic control of the SrTiO₃ crystal-surface, *Science* **266**, 1540 (1994).
- [122] G. Koster, B. L. Kropman, G. J. H. M. Rijnders, D. H. A. Blank, and H. Rogalla, Quasi-ideal Strontium Titanate crystal surfaces through formation of Strontium Hydroxide, *Appl. Phys. Lett.* **73**, 2920 (1998).
- [123] R. Bachelet, F. Sanchez, J. Santiso, C. Munuera, C. Ocal, and J. Fontcuberta, Self-assembly of SrTiO₃ (001) chemical-terminations: A route for oxide-nanostructure fabrication by selective growth, *Chemistry of Materials* **21**, 2494 (2009).
- [124] J. M. Huijbregtse, J. H. Rector, and B. Dam, Effect of the two (100) SrTiO₃ substrate terminations on the nucleation and growth of YBa₂Cu₃O_{7-δ} thin films, *Physica C* **351**, 183 (2001).
- [125] J. Yao, P. B. Merrill, S. S. Perry, D. Marton, and J. W. Rabalais, Thermal stimulation of the surface termination of LaAlO₃ (100), *J. Chem. Phys.* **108**, 1645 (1998).
- [126] H. Kawanowa, H. Ozawa, M. Ohtsuki, Y. Gotoh, and R. Souda, Structure analysis of LaAlO₃ (001) surfaces by low energy neutral scattering spectroscopy, *Surf. Sci.* **506**, 87 (2002).
- [127] D. A. Schmidt, T. Ohta, Q. Yu, and M. A. Olmstead, Influence of perovskite termination on oxide heteroepitaxy, *J. Appl. Phys.* **99**, (2006).
- [128] C. Duriez, C. Chapon, C. R. Henry, and J. M. Rickard, Structural characterization of MgO (100) surfaces, *Surf. Sci.* **230**, 123 (1990).
- [129] I. D. Gay and N. M. Harrison, A density functional study of water and methanol chemisorption on MgO(110), *Surf. Sci.* **591**, 13 (2005).
- [130] K. F. Zheng, Y. H. Yu, Q. L. Guo, S. Liu, E. G. Wang, F. Xu, and P. J. Moller, Coverage-dependent dissociation of H₂O on Pd/MgO(100)/Mo(100), *J. Phys.: Condens. Matter* **17**, 3073 (2005).
- [131] C. D. Daub, G. N. Patey, D. B. Jack, and A. K. Sallabi, Monte Carlo simulations of the adsorption of CO₂ on the MgO(100) surface, *J. Chem. Phys.* **124**, 9 (2006).

- [132] S. C. Lee, H. J. Chae, S. J. Lee, B. Y. Choi, C. K. Yi, J. B. Lee, C. K. Ryu, and J. C. Kim, *Development of regenerable MgO-based sorbent promoted with K_2CO_3 for CO_2 capture at low temperatures*, *Environmental Science & Technology* **42**, 2736 (2008).
- [133] A. B. Joshi and M. G. Norton, *The influence of annealing on the surface morphology of single crystal MgO*, *Appl. Surf. Sci.* **115**, 307 (1997).
- [134] A. F. Degardin, F. Houze, and A. J. Kreisler, *MgO substrate surface optimization for YBaCuO thin film growth*, *IEEE Transactions on Applied Superconductivity* **13**, 2721 (2003).
- [135] T. Thome, L. P. Van, and J. Cousty, *Evolution of yttria-stabilized zirconia (100) surface morphology with temperature*, *Journal of the European Ceramic Society* **24**, 841 (2004).
- [136] R. G. Green, L. Barre, and J. B. Giorgi, *Nano-structures in YSZ (100) surfaces: Implications for metal deposition experiments*, *Surf. Sci.* **601**, 792 (2007).
- [137] U. Hasenkox, C. Mitze, and R. Waser, *Metal propionate synthesis of magnetoresistive $La_{1-x}(Ca,Sr)_xMnO_3$ thin films*, *J. Am. Ceram. Soc.* **80**, 2709 (1997).
- [138] R. W. Schwartz, T. Schneller, and R. Waser, *Chemical solution deposition of electronic oxide films*, *C. R. Chim.* **7**, 433 (2004).
- [139] A. Hassini, A. Pomar, J. Gutierrez, M. Coll, N. Roma, C. Moreno, A. Ruyter, T. Puig, and X. Obradors, *Atomically flat MOD $La_{0.7}Sr_{0.3}MnO_3$ buffer layers for high critical current $YBa_2Cu_3O_7$ TFA films*, *Supercond. Sci. Technol.* **20**, S230 (2007).
- [140] C. Moreno, *New features in solution derived $La_{0.7}Sr_{0.3}MnO_3$ thin films : spontaneous outcropping and nanoscale reversible resistive switching*, *Ph.D. thesis*, Universitat Autònoma de Barcelona (2010).
- [141] L. B. Freund and S. Suresh, *Thin Film materials: stress, defect formation and surface evolution* (Cambridge University Press, Cambridge, 2003).
- [142] M. Ohring, *Materials Science of thin films: deposition and structure* (Academic Press, 1992).
- [143] E. Bauer, *Z. Kristallogr.* **110**, 372 (1958).
- [144] F. C. Frank and J. H. Van der Merwe, *Proc. Roy. Soc. London A* **198**, 205 (1949).
- [145] V. Volmer and A. Weber, *Z. Phys. Chem* **119**, 277 (1926).
- [146] I. N. Stranski and L. Krastanov, *Sitzungsberichte der Akademie der Wissenschaften Wien* **146** (1938).
- [147] V. A. Shchukin and D. Bimberg, *Spontaneous ordering of nanostructures on crystal surfaces*, *Reviews of Modern Physics* **71**, 1125 (1999).
- [148] B. Voigtländer, *Fundamental processes in Si/Si and Ge/Si epitaxy studied by scanning tunneling microscopy during growth*, *Surf. Sci. Rep.* **43**, 127 (2001).
- [149] J. Tersoff and F. K. LeGoues, *Competing relaxation mechanisms in strained layers*, *Phys. Rev. Lett.* **72**, 3570 (1994).
- [150] C. Teichert, *Self-organization of nanostructures in semiconductor heteroepitaxy*, *Physics Reports* **365**, 335 (2002).
- [151] H. T. Johnson and L. B. Freund, *Mechanics of coherent and dislocated island morphologies in strained epitaxial material systems*, *J. Appl. Phys.* **81**, 6081 (1997).
- [152] F. Liu, A. H. Li, and M. G. Lagally, *Self-assembly of two-dimensional islands via strain-mediated coarsening*, *Phys. Rev. Lett.* **87**, 126103 (2001).
- [153] J. A. Floro, G. A. Lucadamo, E. Chason, L. B. Freund, M. Sinclair, R. D. Twisten, and R. Q. Hwang, *SiGe island shape transitions induced by elastic repulsion*, *Phys. Rev. Lett.* **80**, 4717 (1998).
- [154] J. Tersoff and R. M. Tromp, *Shape transition in growth of strained islands: Spontaneous formation of quantum wires*, *Phys. Rev. Lett.* **70**, 2782 (1993).
- [155] J. C. Nie, H. Yamasaki, and Y. Mawatari, *Self-assembled growth of CeO_2 nanostructures on sapphire*, *Phys. Rev. B* **70**, 195421 (2004).

- [156] O. L. Alerhand, D. Vanderbilt, R. D. Meade, and J. D. Joannopoulos, *Spontaneous formation of stress domains on crystal surfaces*, *Phys. Rev. Lett.* **61**, 1973 (1988).
- [157] M. Gibert, *Self-assembled strain-induced oxide nanostructures grown by chemical solutions*, *Ph.D. thesis*, Universitat Autònoma de Barcelona (2009).
- [158] M. J. Akhtar, C. R. A. Catlow, B. Slater, A. M. Walker, and S. M. Woodley, *Bulk and surface simulation studies of $\text{La}_{1-x}\text{Ca}_x\text{MnO}_3$* , *Chemistry of Materials* **18**, 1552 (2006).
- [159] H. Boschker, M. Huijben, A. Vailionis, J. Verbeeck, S. v. Aert, M. Luysberg, S. Bals, G. v. Tendeloo, E. P. Houwman, G. Koster, D. H. A. Blank, and G. Rijnders, *Optimized fabrication of high-quality $\text{La}_{0.67}\text{Sr}_{0.33}\text{MnO}_3$ thin films considering all essential characteristics*, *J. Phys. D: Appl. Phys.* **44**, 205001 (2011).
- [160] P. Abellan, *Interfacial structure and microstructural evolution of solution derived dissimilar oxide nanostructures. Implications on their functional properties*, *Ph.D. thesis*, Universitat Autònoma de Barcelona (2011).
- [161] H. Zheng, Q. Zhan, F. Zavaliche, M. Sherburne, F. Straub, M. P. Cruz, L.-Q. Chen, U. Dahmen, and R. Ramesh, *Controlling self-assembled perovskite-spinel nanostructures*, *Nano Letters* **6**, 1401 (2006).
- [162] F. Tsui, M. C. Smoak, T. K. Nath, and C. B. Eom, *Strain-dependent magnetic phase diagram of epitaxial $\text{La}_{0.67}\text{Sr}_{0.33}\text{MnO}_3$ thin films*, *Appl. Phys. Lett.* **76**, 2421 (2000).
- [163] M. Angeloni, G. Balestrino, N. G. Boggio, P. G. Medaglia, P. Orgiani, and A. Tebano, *Suppression of the metal-insulator transition temperature in thin $\text{La}_{0.7}\text{Sr}_{0.3}\text{MnO}_3$ films*, *J. Appl. Phys.* **96**, 6387 (2004).
- [164] Y. Takamura, R. V. Chopdekar, E. Arenholz, and Y. Suzuki, *Control of the magnetic and magnetotransport properties of $\text{La}_{0.67}\text{Sr}_{0.33}\text{MnO}_3$ thin films through epitaxial strain*, *Appl. Phys. Lett.* **92** (2008).
- [165] M. Huijben, L. W. Martin, Y. H. Chu, M. B. Holcomb, P. Yu, G. Rijnders, D. H. A. Blank, and R. Ramesh, *Critical thickness and orbital ordering in ultrathin $\text{La}_{0.7}\text{Sr}_{0.3}\text{MnO}_3$ films*, *Phys. Rev. B* **78**, 094413 (2008).
- [166] A. J. Millis, T. Darling, and A. Migliori, *Quantifying strain dependence in “colossal” magnetoresistance manganites*, *J. Appl. Phys.* **83**, 1588 (1998).
- [167] L. F. Kourkoutis, J. H. Song, H. Y. Hwang, and D. A. Muller, *Microscopic origins for stabilizing room-temperature ferromagnetism in ultrathin manganite layers*, *PNAS* **107**, 11682 (2010).
- [168] P. W. Anderson, *Absence of diffusion in certain random lattices*, *Phys. Rev.* **109**, 1492 (1958).
- [169] P. Abellán, C. Moreno, F. Sandiumenge, X. Obradors, and M. Casanove, *Misfit relaxation of $\text{La}_{0.7}\text{Sr}_{0.3}\text{MnO}_3$ thin films by a nanodot segregation mechanism*, *Appl. Phys. Lett.* **98**, 041903 (2011).
- [170] C. Moreno, P. Abellán, F. Sandiumenge, M. J. Casanove, and X. Obradors, *Nanocomposite lanthanum strontium manganite thin films formed by using a chemical solution deposition*, *App. Phys. Lett.* **100** (In press).
- [171] M. Gibert, T. Puig, X. Obradors, A. Benedetti, F. Sandiumenge, and R. Hühne, *Self-organization of heteroepitaxial CeO_2 nanodots grown from chemical solutions*, *Adv. Mater.* **19**, 3937 (2007).
- [172] J. Zabaleta, *Autoensamblaje dirigido de nanoestructuras de $\text{Ce}_{0.9}\text{Gd}_{0.1}\text{O}_{2-y}$ crecidas por vía química sobre sustratos nanoindentados*, Tech. Rep. (Universitat Autònoma de Barcelona, 2008).
- [173] J. Zabaleta, N. Mestres, P. Abellan, M. Gibert, F. Sandiumenge, T. Puig, and X. Obradors, *Orientational ordering of solution derived epitaxial Gd-doped ceria nanowires induced by nanoscratching*, *Nanotechnology* **21**, (2010).
- [174] W. Ostwald, *Lehrbruck der Allgemeinen Chemie*, Lehrbruck der Allgemeinen Chemie, Vol. 2 (Leipzig, 1896).
- [175] J. Penuelas, P. Andreatza, C. Andreatza-Vignolle, H. C. N. Tolentino, M. De Santis, and C. Mottet, *Controlling structure and morphology of CoPt nanoparticles through dynamical or static coalescence effects*, *Phys. Rev. Lett.* **100**, 115502 (2008).
- [176] C. J. Lu, S. Senz, and D. Hesse, *The influence of yttria-stabilized zirconia surface pits on the initial stage of reactive $\text{La}_2\text{Zr}_2\text{O}_7$ formation from La_2O_3 vapours and yttria-stabilized zirconia (001) substrates*, *Philos. Mag. A* **81**, 2705 (2001).

- [177] F. F. Lange, H. Shubert, N. Claussen, and M. Ruhle, *Effects of attrition milling and post-sintering heat treatment on fabrication, microstructure and properties of transformation toughened ZrO_2* , *J. Mater. Sci.* **21**, 768 (1986).
- [178] M. Gaudon, C. Laberty-Robert, F. Ansart, P. Stevens, and A. Rousset, *New chemical process for the preparation of fine powders and thin films of LSM_x -YSZ composite oxides*, *Solid State Sci.* **5**, 1377 (2003).
- [179] A. N. Grundy, B. Hallstedt, and L. J. Gauckler, *Assessment of the La-Sr-Mn-O system*, *CALPHAD: Comput. Coupling Phase Diagrams Thermochem.* **28**, 191 (2004).
- [180] M. Backhaus-Ricoult, K. Adib, T. St.Clair, B. Luerssen, L. Gregoratti, and A. Barinov, *In-situ study of operating SOFC LSM/YSZ cathodes under polarization by photoelectron microscopy*, *Solid State Ion.* **179**, 891 (2008).
- [181] H. J. Deiseroth and H. Mueller-Buschbaum, *Ein beitrag zur pyrochlorstruktur an $\text{La}_2\text{Zr}_2\text{O}_7$* , *Z. Anorg. Allg. Chem.* **375**, 152 (1970).
- [182] Y. Tabira, R. L. Withers, T. Yamada, and N. Ishizawa, *Annular dynamical disorder of the rare earth ions in a $\text{La}_2\text{Zr}_2\text{O}_7$ pyrochlore via single crystal synchrotron X-ray diffraction*, *Zeitschrift fur Kristallographie* **216**, 92 (2001).
- [183] K. R. Whittle, L. M. D. Cranswick, S. A. T. Redfern, I. P. Swainson, and G. R. Lumpkin, *Lanthanum pyrochlores and the effect of yttrium addition in the systems $\text{La}_{2-x}\text{Y}_x\text{Zr}_2\text{O}_7$ and $\text{La}_{2-x}\text{Y}_x\text{Hf}_2\text{O}_7$* , *J. Solid State Chem.* **182**, 442 (2009).
- [184] C. Clausen, C. Bagger, J. B. Bildesorensen, and A. Horsewell, *Microstructural and microchemical characterization of the interface between $\text{La}_{0.85}\text{Sr}_{0.15}\text{MnO}_3$ and Y_2O_3 -stabilized ZrO_2* , *Solid State Ion.* **70**, 59 (1994).
- [185] M. Backhaus-Ricoult, M. Badding, J. Brown, M. Carson, E. Sanford, and Y. Thibault, *Interface reactivity between yttria stabilized zirconia and strontium lanthanum manganites*, in *Developments in Solid Oxide Fuel Cells and Lithium Ion Batteries: Proceedings of the 106th Annual Meeting of the American Ceramic Society*, Ceramic Transactions Series, edited by A. Manthiram, P. N. Kumta, S. K. Sundaram, and S. W. Chan (Wiley-American Ceramic Society, 2004).
- [186] A. Chen, G. Bourne, K. Siebein, R. DeHoff, E. Wachsman, and K. Jones, *Characterization of lanthanum zirconate formation at the A-site-deficient strontium-doped lanthanum manganite cathode/yttrium-stabilized zirconia electrolyte interface of solid oxide fuel cells*, *J. Am. Ceram. Soc.* **91**, 2670 (2008).
- [187] Y. L. Liu, A. Hagen, R. Barfod, M. Chen, H. J. Wang, F. W. Poulsen, and P. V. Hendriksen, *Microstructural studies on degradation of interface between LSM-YSZ cathode and YSZ electrolyte in SOFCs*, *Solid State Ion.* **180**, 1298 (2009).
- [188] C. W. Sun, R. Hui, and J. Roller, *Cathode materials for solid oxide fuel cells: a review*, *J. Solid State Electrochem.* **14**, 1125.
- [189] S. Bernal, F. J. Botana, J. J. Calvino, C. López-Cartes, J. A. Pérez-Omil, and J. M. Rodríguez-Izquierdo, *The interpretation of HREM images of supported metal catalysts using image simulation: profile view images*, *Ultramicroscopy* **72**, 135 (1998).
- [190] J. Pérez-Omil, Ph.D. thesis, University of Cadiz (2004).
- [191] J. A. Venables, *Atomic processes in crystal growth*, *Surf. Sci.* **299-300**, 798 (1994).
- [192] B. Fischer, H. Brune, J. V. Barth, A. Fricke, and K. Kern, *Nucleation kinetics on inhomogeneous substrates: Al/Au(111)*, *Phys. Rev. Lett.* **82**, 1732 (1999).
- [193] C. J. Lu, S. Senz, and D. Hesse, *The impact of YSZ surface steps on structure and morphology of $\text{La}_2\text{Zr}_2\text{O}_7$ islands growing on YSZ(1 0 0) surfaces by vapour-solid reaction*, *Surf. Sci.* **515**, 507 (2002).
- [194] C. J. Lu, S. Senz, and D. Hesse, *Formation and structure of misfit dislocations at the $\text{La}_2\text{Zr}_2\text{O}_7$ - Y_2O_3 -stabilized ZrO_2 (001) reaction front during vapour-solid reaction*, *Philos. Mag. Lett.* **82**, 167 (2002).
- [195] S. Chikazumi, *Physics of Magnetism* (John Wiley & Sons, 1964).
- [196] A. Haghir-Gosnet, *Microstructure and magnetic properties of strained $\text{La}_{0.7}\text{Sr}_{0.3}\text{MnO}_3$ thin films*, *J. Appl. Phys.* **88**, 4257 (2000).

- [197] J. Curiale, M. Granada, H. E. Troiani, R. D. Sanchez, A. G. Leyva, P. Levy, and K. Samwer, *Magnetic dead layer in ferromagnetic manganite nanoparticles*, *Appl. Phys. Lett.* **95**, (2009).
- [198] J. Smit and H. G. Beljers, *Philips Res. Rep.* **10**, 113 (1955).
- [199] K. Steenbeck and R. Hiergeist, *Magnetic anisotropy of ferromagnetic $\text{La}_{0.7}(\text{Sr}, \text{Ca})_{0.3}\text{MnO}_3$ epitaxial films*, *Appl. Phys. Lett.* **75**, 1778 (1999).
- [200] P. Abellán, J. Zabaleta, J. Santiso, M. J. Casanove, N. Dix, J. Aguiar, N. D. Browning, N. Mestres, T. Puig, X. Obradors, and F. Sandiumenge, *Interface structure governed by plastic and structural dissimilarity in perovskite $\text{La}_{0.7}\text{Sr}_{0.3}\text{MnO}_3$ nanodots on rock-salt MgO substrates*. (Submitted).
- [201] B. Yang, F. Liu, and M. G. Lagally, *Local strain-mediated chemical potential control of quantum dot self-organization in heteroepitaxy*, *Phys. Rev. Lett.* **92**, (2004).
- [202] Y. Du, S. Atha, R. Hull, J. F. Groves, I. Lyubnitsky, and D. R. Baer, *Focused-ion-beam directed self-assembly of Cu_2O islands on SrTiO_3 (100)*, *Appl. Phys. Lett.* **84**, 5213 (2004).
- [203] A. Strachan, T. Çağın, and W. A. Goddard III, *Phase diagram of MgO from density-functional theory and molecular-dynamics simulations*, *Phys. Rev. B* **60**, 15084 (1999).
- [204] in *Magnesium oxide (MgO) impurities and defects*. Landolt-Börnstein - Group III Condensed Matter Numerical Data and Functional Relationships in Science and Technology, Vol. 41B, edited by O. Madelung, U. Rössler, and M. Schulz (SpringerMaterials).
- [205] A. M. Glass, *Reactions between vacancies and impurities in magnesium oxide. I. Cr^{3+} ion impurities*, *J. Chem. Phys.* **46**, 2080 (1967).
- [206] <http://www.2spi.com/catalog/submat/magnesium-oxide.shtml> (2011).
- [207] Y. S. Kuz'minov, E. E. Lomonova, and V. V. Osiko, *Cubic Zirconia and Skull Melting*, 2nd ed. (Cambridge Int Science Publishing, 2008).
- [208] M. Khalid, A. Setzer, M. Ziese, P. Esquinazi, D. Spemann, A. Pöppel, and E. Goering, *Ubiquity of ferromagnetic signals in common diamagnetic oxide crystals*, *Phys. Rev. B* **81**, 214414 (2010).
- [209] M. J. Hytch, E. Snoeck, and R. Kilaas, *Quantitative measurement of displacement and strain fields from HREM micrographs*, *Ultramicroscopy* **74**, 131 (1998).
- [210] R. M. Bozorth and H. J. Williams, *Rev. Mod. Phys.* **17**, 72 (1945).
- [211] S. Xie, J. Cheng, B. W. Wessels, and V. P. Dravid, *Interfacial structure and chemistry of epitaxial CoFe_2O_4 thin films on SrTiO_3 and MgO substrates*, *Appl. Phys. Lett.* **93**, 181901 (2008).
- [212] T. W. Darling, A. Migliori, E. G. Moshopoulou, S. A. Trugman, J. J. Neumeier, J. L. Sarrao, A. R. Bishop, and J. D. Thompson, *Measurement of the elastic tensor of a single crystal of $\text{La}_{0.83}\text{Sr}_{0.17}\text{MnO}_3$ and its response to magnetic fields*, *Phys. Rev. B* **57**, 5093 (1998).
- [213] R. V. Demin, L. I. Koroleva, and A. M. Balbashov, *Anomalies of magnetostriction and thermal expansion in $\text{La}_{0.7}\text{Sr}_{0.3}\text{MnO}_3$ perovskite*, *J. Magn. Magn. Mater.* **177-181**, 871 (1998).
- [214] K. Nakamura, X. Liu, T. Hatano, Z. Jiao, K. Shang, and A. Ishii, *Mn and Mg interdiffusion and magnetotransport properties of $\text{La}_{0.7}\text{Sr}_{0.3}\text{MnO}_3$ films on MgO (100) substrate*, *Jpn. J. Appl. Phys.* **39**, 1721 (2000).
- [215] J. E. Huheey, E. A. Keiter, and R. L. Keiter, *Inorganic Chemistry: Principles of Structure and Reactivity*, 4th ed. (Prentice Hall, 1997).
- [216] M. Winter, <http://www.webelements.com> (2011).
- [217] C.-C. T. Yang, W.-C. J. Wei, and A. Roosen, *Reaction kinetics and mechanisms between $\text{La}_{0.65}\text{Sr}_{0.3}\text{MnO}_3$ and 8 mol% Yttria-Stabilized Zirconia*, *J. Am. Ceram. Soc.* **87**, 1110 (2004).
- [218] M. Palcut, K. Wiik, and T. Grande, *Cation self-diffusion and nonstoichiometry of lanthanum manganite studied by diffusion couple measurements*, *J. Phys. Chem. C* **111**, 813 (2006).
- [219] Y. Martin and H. K. Wickramasinghe, *Magnetic imaging by force microscopy with 1000-Å resolution*, *Appl. Phys. Lett.* **50**, 1455 (1987).

- [220] J. J. Saenz, N. Garcia, P. Grutter, E. Meyer, H. Heinzelmann, R. Wiesendanger, L. Rosenthaler, H. R. Hidber, and H. J. Guntherodt, *Observation of magnetic forces by the atomic force microscope*, *J. Appl. Phys.* **62**, 4293 (1987).
- [221] B. L. Ramakrishna and E. W. Ong, *Surface evaluation by atomic force microscopy*, Encyclopedia of Materials: Science and Technology, Elsevier Science Ltd. , 9030 (2001).
- [222] R. García and R. Pérez, *Dynamic atomic force microscopy methods*, *Surf. Sci. Rep.* **47**, 197 (2002).
- [223] A. Asenjo, J. M. Garcia, and M. Vazquez, *Magnetic force microscopy: an advanced technique for the observation of magnetic domain and walls*, in *Research Developments in Magnetism*, Vol. 2, edited by S. Pandalai (Transworld Res. Network, 2001) pp. 25–34.
- [224] U. Hartmann, *Magnetic force microscopy - some remarks from the micromagnetic point of view*, *J. Appl. Phys.* **64**, 1561 (1988).
- [225] J. J. Saenz, N. Garcia, and J. C. Slonczewski, *Theory of magnetic imaging by force microscopy*, *Appl. Phys. Lett.* **53**, 1449 (1988).
- [226] H. J. Mamin, D. Rugar, J. E. Stern, B. D. Terris, and S. E. Lambert, *Force microscopy of magnetization patterns in longitudinal recording media*, *Appl. Phys. Lett.* **53**, 1563 (1988).
- [227] U. Hartmann, *The point dipole approximation in magnetic force microscopy*, *Phys. Lett. A* **137**, 475 (1989).
- [228] J. M. Garcia, A. Thiaville, J. Miltat, K. J. Kirk, J. N. Chapman, and F. Alouges, *Quantitative interpretation of magnetic force microscopy images from soft patterned elements*, *Appl. Phys. Lett.* **79**, 656 (2001).
- [229] R. Engel-Herbert, D. M. Schaadt, and T. Hesjedal, *Analytical and numerical calculations of the magnetic force microscopy response: A comparison*, *J. Appl. Phys.* **99**, 113905 (2006).
- [230] W. G. Morris, *Atomic force microscopy*, Encyclopedia of Materials: Science and Technology, Elsevier Science , 365 (2001).
- [231] M. Jaafar, *Procesos de imanación en la nanoescala mediante microscopía de fuerzas magnéticas*, Ph.D. thesis, Universidad Autónoma de Madrid (2009).
- [232] M. Jaafar, J. Gomez-Herrero, A. Gil, P. Ares, M. Vazquez, and A. Asenjo, *Variable-field magnetic force microscopy*, *Ultramicroscopy* **109**, 693 (2009).
- [233] <http://www.nanosensors.com/>, .
- [234] R. M. Bozorth and J. G. Walker, *Effect of ordering on the magnetic anisotropy of iron nickel alloys*, *Phys. Rev.* **83**, 871 (1951).
- [235] M. M. Yang, S. E. Lambert, J. K. Howard, and C. Hwang, *Laminated CoPtCr/Cr films for low noise longitudinal recording*, *IEEE Trans. Magn.* **27**, 5052 (1991).
- [236] C. D. Fuerst and E. G. Brewer, *High-remanence rapidly solidified Nd-Fe-B: Die-upset magnets*, *J. Appl. Phys.* **73**, 5751 (1993).
- [237] J. W. F. Brown, *The fundamental theorem of fine-ferromagnetic-particle theory*, *J. Appl. Phys.* **39**, 993 (1968).
- [238] K. L. Metlov and K. Y. Guslienko, *Stability of magnetic vortex in soft magnetic nano-sized circular cylinder*, *J. Magn. Magn. Mater.* **242**, 1015 (2002).
- [239] E. Y. Tsymlal, *Theory of magnetostatic coupling in thin-film rectangular magnetic elements*, *Appl. Phys. Lett.* **77**, 2740 (2000).
- [240] J. Mejia-Lopez, D. Altbir, A. H. Romero, X. Batlle, I. V. Roshchin, C. P. Li, and I. K. Schuller, *Vortex state and effect of anisotropy in sub-100-nm magnetic nanodots*, *J. Appl. Phys.* **100**, (2006).
- [241] <http://math.nist.gov/oommf/>, .
- [242] R. Akiyama, H. Tanaka, T. Matsumoto, and T. Kawai, *Spin-polarized scanning tunneling microscopy on half-metallic manganite thin film with half-metallic manganite tip*, *Appl. Phys. Lett.* **79**, 4378 (2001).

- [243] S. Y. Chou, *Patterned magnetic nanostructures and quantized magnetic disks*, *Proceedings of the Ieee* **85**, 652 (1997).
- [244] L. S. Kong, L. Zhuang, and S. Y. Chou, *Writing and reading 7.5 Gbits/in² longitudinal quantized magnetic disk using magnetic force microscope tips*, *IEEE Trans. Magn.* **33**, 3019 (1997).
- [245] M. Todorovic, S. Schultz, J. Wong, and A. Scherer, *Writing and reading of single magnetic domain per bit perpendicular patterned media*, *Appl. Phys. Lett.* **74**, 2516 (1999).
- [246] B. Van Waeyenberge, A. Puzic, H. Stoll, K. W. Chou, T. Tylliszczak, R. Hertel, M. Fahnle, H. Bruckl, K. Rott, G. Reiss, I. Neudecker, D. Weiss, C. H. Back, and G. Schutz, *Magnetic vortex core reversal by excitation with short bursts of an alternating field*, *Nature* **444**, 461 (2006).
- [247] R. Hertel, S. Gliga, auml, M. hnle, and C. M. Schneider, *Ultrafast nanomagnetic toggle switching of vortex cores*, *Phys. Rev. Lett.* **98**, 117201 (2007).
- [248] M. Jaafar, R. Yanes, D. P. de Lara, O. Chubykalo-Fesenko, A. Asenjo, E. M. Gonzalez, J. V. Anguita, M. Vazquez, and J. L. Vicent, *Control of the chirality and polarity of magnetic vortices in triangular nanodots*, *Phys. Rev. B* **81**, (2010).
- [249] J. Raabe, R. Pulwey, R. Sattler, T. Schweinbock, J. Zweck, and D. Weiss, *Magnetization pattern of ferromagnetic nanodisks*, *J. Appl. Phys.* **88**, 4437 (2000).
- [250] J. M. Garcia-Martin, A. Thiaville, J. Miltat, T. Okuno, L. Vila, and L. Piroux, *Imaging magnetic vortices by magnetic force microscopy: experiments and modelling*, *J. Phys. D: Appl. Phys.* **37**, 965 (2004).
- [251] L. D. Buda, I. L. Prejbeanu, U. Ebels, and K. Ounadjela, *Micromagnetic simulations of magnetisation in circular cobalt dots*, *Comp. Mater. Sci.* **24**, 181 (2002).
- [252] A. Schwarz, M. Liebmann, U. Kaiser, R. Wiesendanger, T. W. Noh, and D. W. Kim, *Visualization of the Barkhausen effect by magnetic force microscopy*, *Phys. Rev. Lett.* **92**, (2004).
- [253] J. Mejia-Lopez, D. Altbir, P. Landeros, J. Escrig, A. H. Romero, I. V. Roshchin, C. P. Li, M. R. Fitzsimmons, X. Battle, and I. K. Schuller, *Development of vortex state in circular magnetic nanodots: Theory and experiment*, *Phys. Rev. B* **81**, (2010).
- [254] R. Hertel and C. M. Schneider, *Exchange explosions: Magnetization dynamics during vortex-antivortex annihilation*, *Phys. Rev. Lett.* **97**, (2006).
- [255] M. Konoto, T. Kohashi, K. Koikie, T. Arima, Y. Kaneko, Y. Tomioka, and Y. Tokura, *Magnetic domain structure of a $\text{La}_{0.7}\text{Sr}_{0.3}\text{MnO}_3$ (001) surface observed by a spin-polarized scanning electron microscope*, *Appl. Phys. Lett.* **84**, 2361 (2004).
- [256] T. Pokhil, D. A. Song, and J. Nowak, *Spin vortex states and hysteretic properties of submicron size NiFe elements*, *J. Appl. Phys.* **87**, 6319 (2000).
- [257] L. D. Buda, I. L. Prejbeanu, I. L. Demand, M. Demand, U. Ebels, and K. Ounadjela, *Vortex states stability in circular $\text{Co}(0001)$ dots*, *IEEE Trans. Magn.* **37**, 2061 (2001).
- [258] N. Martin, N. C. Bigall, I. Monch, T. Gemming, A. Eychmuller, R. Mattheis, R. Schafer, L. Schultz, and J. McCord, *Enhanced nucleation of vortices in soft magnetic materials prepared by silica nanosphere lithography*, *Adv. Funct. Mater.* **21**, 891 (2011).
- [259] T. Okuno, K. Shigeto, T. Ono, K. Mibu, and T. Shinjo, *MFM study of magnetic vortex cores in circular permalloy dots: behavior in external field*, *J. Magn. Magn. Mater.* **240**, 1 (2002).
- [260] K. Y. Guslienko, V. Novosad, Y. Otani, H. Shima, and K. Fukamichi, *Magnetization reversal due to vortex nucleation, displacement, and annihilation in submicron ferromagnetic dot arrays*, *Phys. Rev. B* **65**, 024414 (2001).
- [261] L. Kelvin, *Contact electricity of metals*, *Philos. Mag.* **46**, 82 (1898).
- [262] G. H. Enevoldsen, T. Glatzel, M. C. Christensen, J. V. Lauritsen, and F. Besenbacher, *Atomic scale Kelvin Probe Force Microscopy studies of the surface potential variations on the $\text{TiO}_2(110)$ surface*, *Phys. Rev. Lett.* **100**, 236104 (2008).

- [263] S. Sadewasser, P. Jelinek, C.-K. Fang, O. Custance, Y. Yamada, Y. Sugimoto, M. Abe, and S. Morita, *New insights on atomic-resolution frequency-modulation Kelvin-Probe Force-Microscopy imaging of semiconductors*, *Phys. Rev. Lett.* **103**, 266103 (2009).
- [264] W. Wan, J. Feng, H. A. Padmore, and D. S. Robin, *Simulation of a mirror corrector for PEEM3*, *Nucl. Instrum. Methods Phys. Res., Sect. A* **519**, 222 (2004).
- [265] M. Schneider, Claus and G. Schönhense, *Investigating surface magnetism by means of photoexcitation electron emission microscopy*, *Reports on Progress in Physics* **65**, 1785 (2002).
- [266] J. Feng and A. Scholl, *Photoemission electron microscopy (PEEM)*, in *Science of Microscopy*, edited by P. W. Hawkes and J. C. H. Spence (Springer New York, 2007) pp. 657–695.
- [267] B. T. Thole, G. van der Laan, J. C. Fuggle, G. A. Sawatzky, R. C. Karnatak, and J. M. Esteve, *3d X-ray-absorption lines and the $3d^9 4f^{n+1}$ multiplets of the lanthanides*, *Phys. Rev. B* **32**, 5107 (1985).
- [268] Y. Ufuktepe, G. Akgül, and J. Lüning, *X-ray photoabsorption and total electron yield of Fe thin films at the $L_{2,3}$ edge*, *J. Alloys Compd.* **401**, 193 (2005).
- [269] R. Nakajima, J. Stöhr, and Y. U. Idzerda, *Electron-yield saturation effects in L-edge x-ray magnetic circular dichroism spectra of Fe, Co, and Ni*, *Phys. Rev. B* **59**, 6421 (1999).
- [270] M. C. Richter, P. De Padova, C. Quaresima, P. Perfetti, R. Brochier, V. Ilakovac, O. Heckmann, L. Lechevallier, M. Zerrouki, C. Teodorescu, C. S. Fadley, N. Hamdan, and K. Hricovini, *Resonant photoemission and XMCD on Mn-based systems*, *J. Alloys Compd.* **362**, 41 (2004).
- [271] B. T. Thole, P. Carra, F. Sette, and G. van der Laan, *X-ray circular dichroism as a probe of orbital magnetization*, *Phys. Rev. Lett.* **68**, 1943 (1992).
- [272] C. T. Chen, Y. U. Idzerda, H. J. Lin, N. V. Smith, G. Meigs, E. Chaban, G. H. Ho, E. Pellegrin, and F. Sette, *Experimental confirmation of the X-ray magnetic circular dichroism sum rules for iron and cobalt*, *Phys. Rev. Lett.* **75**, 152 (1995).
- [273] A. Scholl, J. Stöhr, J. Lüning, J. W. Seo, J. Fompeyrine, H. Siegwart, J. P. Locquet, F. Nolting, S. Anders, E. E. Fullerton, M. R. Scheinfein, and H. A. Padmore, *Observation of antiferromagnetic domains in epitaxial thin films*, *Science* **287**, 1014 (2000).
- [274] B. Henke, E. Gullikson, and J. Davis, *X-ray interactions: photoabsorption, scattering, transmission, and reflection at $E=50\text{--}30000\text{ eV}$, $Z=1\text{--}92$* , *Atomic Data and Nuclear Data Tables* **54**, 181 (1993).
- [275] C. J. Powell and A. Jablonski, *Surface sensitivity of X-ray photoelectron spectroscopy*, *Nucl. Instrum. Methods Phys. Res., Sect. A* **601**, 54 (2009).
- [276] C. J. Powell and A. Jablonski, *NIST Electron Effective-Attenuation-Length Database Version 1.3* (National Institute of Standards and Technology, Gaithersburg, MD, 2011).
- [277] S. Stadler, Y. U. Idzerda, Z. Chen, S. B. Ogale, and T. Venkatesan, *The magnetism of a buried $\text{La}_{0.7}\text{Sr}_{0.3}\text{MnO}_3$ interface*, *Appl. Phys. Lett.* **75**, 3384 (1999).
- [278] M. P. de Jong, I. Bergenti, V. A. Dediu, M. Fahlman, M. Marsi, and C. Taliani, *Evidence for Mn^{2+} ions at surfaces of $\text{La}_{0.7}\text{Sr}_{0.3}\text{MnO}_3$ thin films*, *Phys. Rev. B* **71**, 014434 (2005).
- [279] S. Valencia, A. Gaupp, W. Gudat, L. Abad, L. Balcells, A. Cavallaro, B. Martínez, and F. J. Palomares, *Mn valence instability in $\text{La}_{2/3}\text{Ca}_{1/3}\text{MnO}_3$ thin films*, *Phys. Rev. B* **73**, 104402 (2006).
- [280] M. P. de Jong, I. Bergenti, W. Osikowicz, R. Friedlein, V. A. Dediu, C. Taliani, and W. R. Salaneck, *Valence electronic states related to Mn^{2+} at $\text{La}_{0.7}\text{Sr}_{0.3}\text{MnO}_3$ surfaces characterized by resonant photoemission*, *Phys. Rev. B* **73**, 052403 (2006).
- [281] S. Valencia, A. Gaupp, W. Gudat, L. Abad, L. Balcells, and B. Martínez, *Impact of microstructure on the Mn valence of $\text{La}_{2/3}\text{Ca}_{1/3}\text{MnO}_3$ thin films*, *Phys. Rev. B* **75**, 184431 (2007).
- [282] C. Mitra, Z. Hu, P. Raychaudhuri, S. Wirth, S. I. Csiszar, H. H. Hsieh, H. J. Lin, C. T. Chen, and L. H. Tjeng, *Direct observation of electron doping in $\text{La}_{0.7}\text{Ce}_{0.3}\text{MnO}_3$ using X-ray absorption spectroscopy*, *Phys. Rev. B* **67**, 092404 (2003).

-
- [283] F. M. F. de Groot, J. C. Fuggle, B. T. Thole, and G. A. Sawatzky, *2p x-ray absorption of 3d transition-metal compounds: An atomic multiplet description including the crystal field*, *Phys. Rev. B* **42**, 5459 (1990).
 - [284] S. Heun, Y. Watanabe, B. Ressel, D. Bottomley, T. Schmidt, and K. C. Prince, *Core-level photoelectron spectroscopy from individual heteroepitaxial nanocrystals on GaAs(001)*, *Phys. Rev. B* **63**, 125335 (2001).
 - [285] F. Ratto, A. Locatelli, S. Fontana, S. Kharrazi, S. Ashtaputre, S. K. Kulkarni, S. Heun, and F. Rosei, *Chemical mapping of individual semiconductor nanostructures*, *Small* **2**, 401 (2006).
 - [286] W. Yang, M. Zeman, and R. J. Nemanich, *Coarsening dynamics of nanoscale Ti-silicide islands on Si surfaces*, *J. Korean Phys. Soc.* **50**, 575 (2007).
 - [287] A. Moewes, S. Stadler, R. P. Winarski, D. L. Ederer, M. M. Grush, and T. A. Callcott, *Core-hole induced charge transfer and Coster-Kronig enhanced fluorescence at the 3d threshold of lanthanum studied by resonant inelastic scattering*, *Phys. Rev. B* **58**, R15951 (1998).
 - [288] www.efunda.com/materials/elements/TC_Table.cfm?Element_ID=pt (2011).
 - [289] J. L. Cohn, J. J. Neumeier, C. P. Popoviciu, K. J. McClellan, and T. Leventouri, *Local lattice distortions and thermal transport in perovskite manganites*, *Phys. Rev. B* **56**, R8495 (1997).
 - [290] D. D. Hass, *Directed Vapor Deposition of Thermal Barrier Coatings*, Ph.D. thesis, University of Virginia (2000).
 - [291] M. Nonnenmacher, M. P. O. Boyle, and H. K. Wickramasinghe, *Kelvin Probe Force Microscopy*, *Appl. Phys. Lett.* **58**, 2921 (1991).
 - [292] C. Sommerhalter, *High-sensitivity quantitative kelvin probe microscopy by noncontact ultra-high-vacuum atomic force microscopy*, *Appl. Phys. Lett.* **75**, 286 (1999).
 - [293] T. Glatzel, M. C. Lux-Steiner, E. Strassbourg, A. Boag, and Y. Rosenwaks, *Principles of Kelvin Probe Force Microscopy*, in *Scanning Probe Microscopy: Electrical and Electromechanical Phenomena at the Nanoscale*, Vol. 2, edited by S. V. Kalinin and A. Gruverman (Springer, New York, 2007) pp. 113–131.
 - [294] O. Douhéret, S. Anand, T. Glatzel, K. Maknys, and S. Sadewasser, *Characterization of quantum wells by cross-sectional Kelvin probe force microscopy*, *Appl. Phys. Lett.* **85**, 5245 (2004).
 - [295] A. Schwarzman, *Nanoscale potential distribution across multi-quantum well structures: Kelvin probe force microscopy and secondary electron imaging*, *J. Appl. Phys.* **98**, 084310 (2005).
 - [296] S. Shusterman, A. Raizman, A. Sher, Y. Paltiel, A. Schwarzman, E. Lepkifker, and Y. Rosenwaks, *Nanoscale mapping of strain and composition in quantum dots using Kelvin probe force microscopy*, *Nano Letters* **7**, 2089 (2007).
 - [297] G. N. Luo, K. Yamaguchi, T. Terai, and M. Yamawaki, *Charging effect on work function measurements of lithium ceramics under irradiation*, *J. Alloys Compd.* **349**, 211 (2003).
 - [298] C. Barth and C. R. Henry, *Gold nanoclusters on alkali halide surfaces: Charging and tunneling*, *Appl. Phys. Lett.* **89**, 252119 (2006).
 - [299] C. Barth and C. R. Henry, *Kelvin probe force microscopy on surfaces of UHV cleaved ionic crystals*, *Nanotechnology* **17**, S155 (2006).
 - [300] C. Barth and C. R. Henry, *Surface double layer on (001) surfaces of alkali halide crystals: A scanning force microscopy study*, *Phys. Rev. Lett.* **98**, 136804 (2007).
 - [301] S. Gómez-Moñivas, L. Froufe-Pérez, A. Caamaño, and J. Sáenz, *Electrostatic forces between sharp tips and metallic and dielectric samples*, *Appl. Phys. Lett.* **79**, 4048 (2001).
 - [302] J. Zuñiga-Pérez, E. Palacios-Lidón, V. Muñoz-Sanjosé, and J. Colchero, *Nanoscale determination of surface orientation and electrostatic properties of ZnO thin films*, *Appl. Phys. A* **88**, 77 (2007).
 - [303] M. Fujihira, *Kelvin Probe Force Microscopy of molecular surfaces*, *Annual Review of Materials Science* **29**, 353 (1999).
 - [304] W. A. Zisman, *A new method of measuring contact potential differences in metals*, *Rev. Sci. Instrum.* **3**, 367 (1932).

- [305] D. W. Abraham, C. Williams, J. Slinkman, and H. K. Wickramasinghe, *Lateral dopant profiling in semiconductors by force microscopy using capacitive detection*, *J. Vac. Sci. Technol. B* **9**, 703 (1991).
- [306] S. V. Kalinin and A. Gruverman, *Scanning Probe Microscopy* (Springer, New York, 2007).
- [307] A. Sasahara, C. L. Pang, and H. Onishi, *Probe microscope observation of platinum atoms deposited on the TiO₂(110)-(1×1) surface*, *J. Phys. Chem. B* **110**, 13453 (2006).
- [308] L. Nony, A. S. Foster, F. Bocquet, and C. Loppacher, *Understanding the atomic-scale contrast in Kelvin Probe Force Microscopy*, *Phys. Rev. Lett.* **103**, 036802 (2009).
- [309] S. Lee, A. Shinde, and R. Ragan, *Morphological work function dependence of rare-earth disilicide metal nanostructures*, *Nanotechnology* **20**, 035701 (2009).
- [310] T. Glatzel, S. Sadewasser, and M. C. Lux-Steiner, *Amplitude or frequency modulation-detection in Kelvin Probe Force Microscopy*, *Appl. Surf. Sci.* **210**, 84 (2003).
- [311] A. Kikukawa, S. Hosaka, and R. Imura, *Vacuum compatible high-sensitive Kelvin Probe Force Microscopy*, *Rev. Sci. Instrum.* **67**, 1463 (1996).
- [312] Y. Rosenwaks, R. Shikler, T. Glatzel, and S. Sadewasser, *Kelvin Probe Force Microscopy of semiconductor surface defects*, *Phys. Rev. B* **70**, 085320 (2004).
- [313] T. R. Albrecht, P. Grütter, D. Horne, and D. Rugar, *Frequency modulation detection using high-Q cantilevers for enhanced force microscope sensitivity*, *J. Appl. Phys.* **69**, 668 (1991).
- [314] <http://www.budgetsensors.com>.
- [315] T. Ngai, W. J. Qi, R. Sharma, J. Fretwell, X. Chen, J. C. Lee, and S. Banerjee, *Electrical properties of ZrO₂ gate dielectric on SiGe*, *Appl. Phys. Lett.* **76**, 502 (2000).
- [316] G. A. Samara, *Low temperature dielectric properties of candidate substrates for high-temperature superconductors: LaAlO₃ and ZrO₂: 9.5 mol% Y₂O₃*, *J. Appl. Phys.* **68**, 4214 (1990).
- [317] M. Weinert and R. E. Watson, *Contributions to the work function of crystals*, *Phys. Rev. B* **29**, 3001 (1984).
- [318] S. Duhm, G. Heimel, I. Salzmann, H. Glowatzki, R. L. Johnson, A. Vollmer, J. P. Rabe, and N. Koch, *Orientation-dependent ionization energies and interface dipoles in ordered molecular assemblies*, *Nat. Mater.* **7**, 326 (2008).
- [319] K. Okamoto, Y. Sugawara, and S. Morita, *The elimination of the artifact in the electrostatic force measurement using a novel noncontact atomic force microscope/electrostatic force microscope*, *Appl. Surf. Sci.* **188**, 381 (2002).
- [320] M. Lee, W. Lee, and F. B. Prinz, *Geometric artefact suppressed surface potential measurements*, *Nanotechnology* **17**, 3728 (2006).
- [321] N. W. Ashcroft and N. D. Mermin, *Solid State Physics* (Brooks/Cole Thomson Learning, 1976).
- [322] D. Cahen and A. Kahn, *Electron energetics at surfaces and interfaces: Concepts and experiments*, *Adv. Mater.* **15**, 271 (2003).
- [323] H. Ishii, K. Sugiyama, E. Ito, and K. Seki, *Energy level alignment and interfacial electronic structures at organic/metal and organic/organic interfaces*, *Adv. Mater.* **11**, 605 (1999).
- [324] N. D. Lang and W. Kohn, *Theory of metal surfaces: Work function*, *Phys. Rev. B* **3**, 1215 (1971).
- [325] C. Fall, *Ab-initio study of the work functions of elemental metal crystals*, Ph.D. thesis, EPFL (1999).
- [326] K. Wandelt, *The local work function: Concept and implications*, *Appl. Surf. Sci.* **111**, 1 (1997).
- [327] R. Smoluchowski, *Anisotropy of the electronic work function of metals*, *Phys. Rev.* **60**, 661 (1941).
- [328] H. B. Michaelson, *The work function of the elements and its periodicity*, *J. Appl. Phys.* **48**, 4729 (1977).
- [329] G. Binnig, C. F. Quate, and C. Gerber, *Atomic force microscope*, *Phys. Rev. Lett.* **56**, 930 (1986).

- [330] G. Binnig, H. Rohrer, C. Gerber, and E. Weibel, *Surface studies by scanning tunneling microscopy*, *Phys. Rev. Lett.* **49**, 57 (1982).
- [331] H. Fuchs, H. Hölscher, and A. Schirmeisen, *Scanning probe microscopy*, Encyclopedia of Materials: Science and Technology, Elsevier Ltd. , 12 (2005).
- [332] <http://knol.google.com/k/atomic-force-microscopy-afm> (2011).
- [333] E. Meyer, H. J. Hug, and R. Bennewitz, *Scanning Probe Microscopy The Lab on a Tip*, Advanced Texts in Physics (Springer, 2004).
- [334] S. V. Kalinin, R. Shao, and D. A. Bonnell, *Local phenomena in oxides by advanced scanning probe microscopy*, *J. Am. Ceram. Soc.* **88**, 1077 (2005).
- [335] www.nanosensors.com (2011).
- [336] I. Horcas, R. Fernandez, J. M. Gomez-Rodriguez, J. Colchero, J. Gomez-Herrero, and A. M. Baro, *WSXM: A software for scanning probe microscopy and a tool for nanotechnology*, *Rev. Sci. Instrum.* **78**, (2007).
- [337] B. B. He, *Two-Dimensional X-ray diffraction* (Wiley, 2009).
- [338] D. B. Williams and C. B. Carter, *Transmission Electron Microscopy. A textbook for materials science* (Springer, New York, 1996,2009).
- [339] P. D. Nellist and S. J. Pennycook, *Incoherent imaging using dynamically scattered coherent electrons*, *Ultramicroscopy* **78**, 111 (1999).

